Politecnico di Torino

b
UNIVERSITÄT BERN

Politecnico di Torino

Master's Degree in Mathematical Engineering

A.a. 2024/2025

Graduation Session November

Quantification of the impact of variable mass transfer coefficients on oxygen transport in the brain

Supervisors:

Prof. Chiara Giverso
Dr. Franca Schmid
Gaia Stievano

Candidate:

Giorgia Barra

Abstract

Oxygen is essential for brain function, as neurons have very high metabolic demands and even small changes in oxygen availability can affect their activity. The brain relies on a dense microcirculation network to deliver oxygen efficiently to all regions. Despite years of research, the understanding of oxygen transport in the brain remains limited. Computational modeling has become an important tool to explore these mechanisms and provide insights that experiments alone cannot deliver.

A key element in oxygen transport is the exchange of oxygen between red blood cells (RBCs) and plasma, quantified by the mass transfer coefficient (MTC). The MTC determines the rate at which oxygen moves from RBCs to plasma, thereby influencing tissue oxygenation. While often assumed constant, studies by Lücker [1] and Vadapalli et al. [2] showed that it varies with hematocrit and oxygen saturation. Accounting for this variability in models enhances their accuracy and better reflects the biological reality of oxygen transport. The aim of this project is to investigate the impact of MTCs on oxygen transport in the brain. Initial findings on the connections between MTC, hematocrit, and oxygen saturation were derived from published studies and subsequently incorporated into a pre-existing computational framework for cerebral oxygen transport.

The numerical study followed a stepwise approach. Simplified test cases were first used to isolate the effect of variable MTCs, facilitating the evaluation of their direct impact on intravascular oxygen exchange. Subsequently, the model was applied to a realistic microvascular network containing approximately 950 vessels embedded in a cubic tissue domain of 400 μm side length, representing a small region of the somatosensory cortex of a mouse. This allowed assessment of how MTC variability shapes both vascular oxygen distribution and tissue oxygenation under more complex and physiologically realistic conditions.

Results indicate that accounting for MTC variability improves the fidelity of oxygen transport predictions, particularly in regions with low hematocrit. Introducing variable MTCs increased the spatial heterogeneity of tissue oxygenation, leading to local differences of up to 20–25 mmHg and average variations of about 2–3 mmHg relative to the constant formulation. The Lücker and Vadapalli models produced

consistent and physiologically grounded predictions, with Lücker providing the best trade-off between accuracy and computational cost.

In conclusion, this project extends existing models by introducing a variable formulation of the MTC. The work highlights the importance of considering microvascular heterogeneity and shows its impact on predictions of oxygen dynamics. These findings improve the ability to model cerebral physiology and may also support the study of pathological conditions where oxygen supply is impaired.

Acknowledgements

First of all, I would like to thank my supervisor, Professor Giverso, for the trust she placed in me and in this project, and for the constant support and availability she has shown throughout the entire thesis work.

I would also like to thank Dr. Franca Schmid and PhD candidate Gaia Stievano for giving me the opportunity to carry out this research project and to explore an aspect of mathematics that has always fascinated me. Thank you for your guidance, your patience, and the valuable insights you have shared with me.

My sincere thanks go to the CVE and UGE groups at ARTORG for welcoming me from the very first day and for making me feel part of the team.

I also wish to thank the people with whom I shared my Erasmus experience in the Netherlands. Your cheerfulness brightened even the rainiest days and made this period a memorable one.

Finally, I would like to thank my family, Federico, and my friends for their constant support, closeness, and encouragement throughout this journey. Your presence has been truly essential.

Ringraziamenti

Vorrei ringraziare innanzitutto la mia relatrice, la professoressa Giverso, per la fiducia che ha riposto in me e in questo progetto, e per la disponibilità e il supporto che mi ha sempre dimostrato durante tutto il percorso di tesi.

Ringrazio inoltre la dottoressa Franca Schmid e la dottoranda Gaia Stievano per avermi offerto l'opportunità di svolgere questo lavoro di ricerca e di applicare un aspetto della matematica che mi ha sempre affascinato. Grazie per la vostra guida, la pazienza e i preziosi insegnamenti.

Un sentito grazie ai gruppi CVE e UGE dell'ARTORG per avermi accolto fin dal primo giorno e per avermi fatto sentire parte del team.

Desidero ringraziare anche le persone con cui ho condiviso l'esperienza Erasmus nei Paesi Bassi. La vostra allegria ha reso più leggere le giornate e ha contribuito a rendere questo periodo un ricordo prezioso.

Un ultimo ringraziamento va alla mia famiglia, a Federico e ai miei amici, per il sostegno costante, la vicinanza e l'incoraggiamento che non sono mai venuti meno durante questo percorso. Il vostro appoggio è stato fondamentale.

Table of Contents

List of Tables

List of Figures

Nomenclature

This section lists the main symbols and abbreviations used throughout the thesis.

Notation

A	Cross sectional area
C	Oxygen concentration
C_0	Oxygen binding capacity
D_T	Diffusion coefficient of the tissue
D	Vessel diameter
H_d	Discharged hematocrit
H_t	Tube hematocrit
K	Dissociation rate constant
k_{cell}	Mass transfer coefficient
k_{L}	Mass transfer coefficient function by Lücker
k_{V}	Mass transfer coefficient function by Vadapalli
k_{C}	Constant mass transfer coefficient value
L	Length
M_0	Oxygen consumption rate
n	Hill exponent
p	Hydraulic pressure
P	Oxygen partial pressure
$P_{\text{RBC,50}}$	Oxygen partial pressure at half hemoglobin saturation
$P_{\text{T,50}}$	Oxygen partial pressure at half consumption

q	flow
R	Hydraulic resistance
S	Saturation
v	Velocity vector
u	Average vector
α	Oxygen solubility
γ	Surface to volume coefficient
μ	Viscosity
ρ	Density
σ	Oxygen permeability

Abbreviations

MVN	Microvascular network
MTC	Mass transfer coefficient
PO_2	Oxygen partial pressure
RBC	Red blood cell
SV	Single vessel

Subscripts

$(\cdot)_{\mathrm{RBC}}$	Refers to the red blood cell phase
$(\cdot)_{\mathrm{pl}}$	Refers to the plasma phase
$(\cdot)_{\mathrm{T}}$	Refers to the tissue domain
$(\cdot)_b$	Refers to the blood
$(\cdot)_v$	Refers to the vessel
$(\cdot)_{\mathrm{in}}$, $(\cdot)_{\mathrm{out}}$	Inlet and outlet quantities

Chapter 1

Introduction

To better understand the topic of this work, this first chapter provides a general introduction to the importance of oxygen for the body and its modeling in current literature.

Among the many organs that rely on oxygen, the brain stands out as one of the most demanding. Indeed, the brain consumes a significant amount of oxygen, using approximately 20% of the total oxygen supply of the body, despite representing only about 2% of body weight [3]. This high demand arises from the critical role of oxygen in generating energy via glucose oxidation. This energy is essential for supporting brain functions such as neuronal activity, maintenance of ionic gradients across cell membranes, and transmission of electrical impulses [4]. Despite its high oxygen demand, the brain has minimal storage capacity, making it extremely susceptible to disruptions in oxygen delivery. Such disruptions may occur due to various pathological conditions, including vascular occlusions and impaired blood flow regulation. In the case of stroke, irreversible injury to brain cells can occur within minutes due to oxygen deprivation. Variations in oxygen concentration are a major factor in numerous diseases and conditions, such as hypertension, diabetes, heart failure, respiratory failure, and traumatic injuries [1].

To better understand the nature of these diseases, it is crucial to complement theoretical knowledge with *in-vivo* measurements of oxygen concentration. Yet, obtaining reliable data in living systems is challenging due to several factors, such as the intrinsic limitations of current imaging methods, the difficulty of isolating specific microvascular changes from systemic responses, and the inherent biological variability of living tissue. These challenges, together with the high cost and complexity of experiments, make computational modeling an important complementary tool for investigating oxygen dynamics under controlled conditions.

To understand both the experimental observations and the modeling approaches, the next section provides a comprehensive overview of oxygen delivery to the brain, covering the main biological mechanisms as well as the associated modeling concepts.

1.1 Oxygen delivery to the brain

Oxygen delivery to the brain is a complex physiological process involving multiple biological structures and mechanisms. This section outlines the key components that govern oxygen transport at both the macroscopic and microscopic scales. It begins with an overview of the brain's vascular architecture and the role of blood in carrying oxygen. Then, it focuses on the mechanisms of oxygen transport across the vasculature and the brain parenchyma.

1.1.1 Brain vasculature

Efficient oxygen delivery to the brain relies on its complex vascular network, as blood is the primary carrier of oxygen throughout the body. The human circulatory system comprises different types of vessels with complementary functions. *Arteries* transport oxygenated blood away from the heart towards tissues, while *veins* return deoxygenated blood back to the heart. The *microcirculation* refers to the network of vessels with diameters below 0.1–0.2 mm. Within this network, small arteries and veins are termed *arterioles* and *venules*, respectively, and they regulate the distribution of blood flow into the capillary beds where exchange takes place. *Capillaries* are the smallest vessels, with diameters ranging from approximately 4 to 9 μm in humans [5] and they connect the arterial and venous systems. Despite their size, they play a central role in oxygen delivery: their extremely thin endothelial walls enable the exchange of gases and nutrients.

The brain receives its blood supply from paired arteries on either side: the *internal carotid artery* and the *vertebral artery*. These arteries converge to form a ring-like structure known as the *Circle of Willis* (Figure 1.1 (a)), from which the *anterior cerebral artery*, *middle cerebral artery*, and *posterior cerebral artery* arise. Further branching of these vessels gives rise to an interconnected network of *pial arteries*, which lie on the *pia mater*, the innermost layer of the *meninges*.

(a) (b)

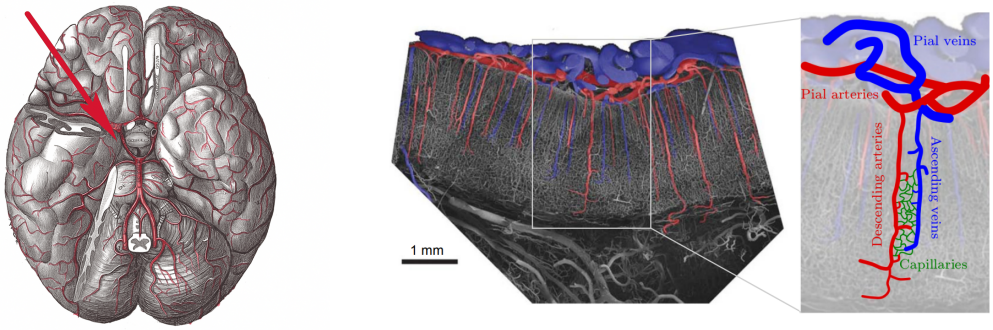

Figure 1.1: (a) Brain arteries and microvasculature: arteries at the base of the brain. The arrow point to the *Circle of Willis*. (Image from [6]). (b) Cortical vascular architecture. Left: Vascular corrosion cast from the monkey primary visual cortex (arteries in red, veins in blue) (Image from [7]). Right: Schematic representation of the cortical vasculature and its key components. (Image from [8])

Penetrating arterioles descend through the *pia mater* into the cortical grey matter, where they branch into tree-like structures that ultimately feed into the capillary bed, a dense network of deeply interconnected tiny vessels. Following exchange within the capillary bed, blood is then collected by *ascending venules*, which drain into the *pial veins*. Finally, oxygen-depleted blood returns to the heart through the venous circulation [6]. The organization of penetrating arterioles, capillaries, and venules in the cortical vasculature is illustrated in Figure 1.1 (b).

1.1.2 Blood

Blood itself is a suspension composed of a liquid and a solid phase. The liquid component, called *plasma*, makes up approximately 55% of the total blood volume. The solid phase consists of three main types of cells: *red blood cells* (RBCs), which are the most abundant and constitute about 44% of blood volume; *white blood cells* (approximately 1%), which are involved in the immune system; and *platelets* (around 1%), which play a critical role in blood coagulation [9]. The most important cells for oxygen transport are the RBCs, as they contain *hemoglobin*, a protein composed of four subunits (two α and two β). Each subunit carries a *heme group* with a central iron atom that binds oxygen. So each hemoglobin molecule can bind up to four oxygen molecules, and the fraction of hemoglobin binding sites occupied by oxygen is referred to as oxygen saturation [10]. The latter is a key physiological variable that reflects how much oxygen is being carried by hemoglobin relative to its maximum capacity. Saturation plays a central role in determining the oxygen

content of the blood and the ability of RBCs to release oxygen to the surrounding tissues.

Understanding blood composition is crucial for identifying the main components of oxygen transport, but this structural knowledge alone is not sufficient. Oxygen delivery also depends on how its carriers move within the vascular network. RBCs, beyond their role as oxygen carriers, also shape microcirculatory blood flow. In large vessels, they usually preserve their biconcave disk shape (7–8 μm in diameter and 2 μm thick), which ensures a high surface area-to-volume ratio for gas exchange and provides flexibility in flow [11]. Under these conditions, their influence on the overall hemodynamics is often negligible. In contrast, in capillaries with diameters comparable to or smaller than a RBC, their role becomes dominant. To pass through such narrow vessels, RBCs deform into axisymmetric, parachute-like shapes. They also migrate toward the vessel center, creating a plasma layer near the walls (the cell-free layer), which reduces flow resistance and affects interactions with the endothelium (this phenomenon is illustrated in Figure 1.2). This deformation, together with their high concentration, profoundly affects local flow patterns, velocity profiles, and pressure distribution, highlighting their active role in microvascular hemodynamics [12].

Studying blood flow dynamics, especially in the microcirculation, is therefore essential to capture the processes that govern oxygen distribution. To achieve a quantitative understanding of these dynamics, appropriate modeling approaches are required, as discussed in the following sections.

1.1.3 Blood flow modeling

Blood is frequently modeled as an incompressible, homogeneous, Newtonian fluid (e.g., [14], [15]). To properly characterize the flow regime, several dimensionless numbers must be considered. The Reynolds number [16] quantifies the ratio between inertial and viscous forces:

$$Re = \frac{\rho_b u D}{\mu_b},$$

where ρ_b is the blood density, u the characteristic velocity, D the vessel diameter, and μ_b the dynamic viscosity. In cases such as the microcirculation, this number is typically very low ($Re \ll 1$), indicating that inertial effects are negligible. As a result, the flow can be accurately described by the Stokes eqs.. The Womersley number [17] is defined as:

$$Wo = r_v \sqrt{\frac{\omega \rho_b}{\mu_b}},$$

with r_v being the vessel radius and ω the angular frequency of the cardiac cycle. This number quantifies the importance of pulsatile effects relative to viscous forces, is small in microvasculature networks. This implies that the pulsatile nature of

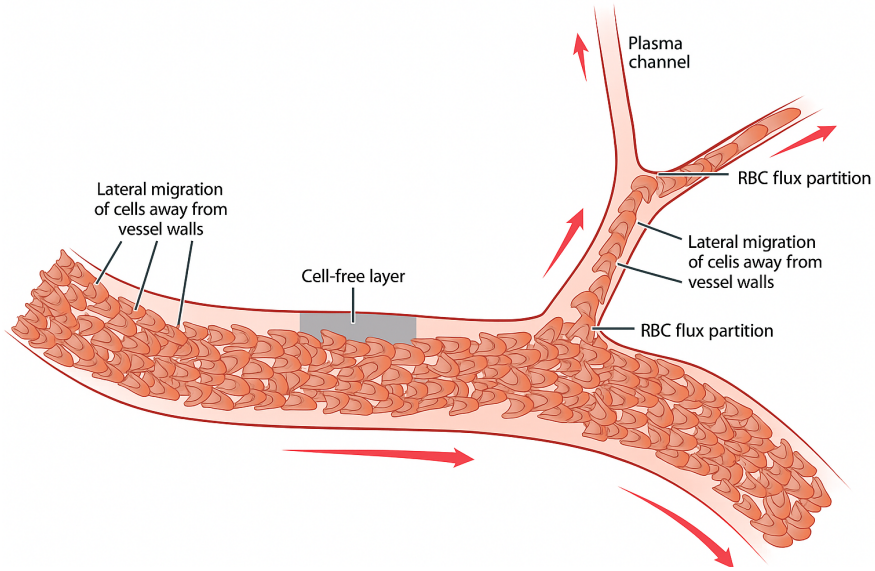

Figure 1.2: Schematic illustration of RBC lateral migration and the formation of a cell-free layer in microvessels. Due to hydrodynamic interactions, RBCs tend to migrate toward the center of the vessel, creating a plasma-rich layer near the vessel walls. At vascular bifurcations, RBCs partition unevenly between branches, with some branches carrying mainly plasma (plasma channel) and others showing single-file motion of RBCs. This partitioning affects the distribution of RBCs and plasma throughout the microcirculatory network. (Image from [13])

blood flow induced by the cardiac cycle can be neglected. This supports the use of steady-state flow eqs.. The Dean number [18] characterizes the influence of curvature, specifically the ratio between centrifugal and viscous forces in curved vessels. It is defined as:

$$De = Re\sqrt{\frac{D}{2r_c}},$$

where r_c is the radius of curvature of the vessel centerline. In microvessels, the Dean number is small, suggesting the impact of vessel tortuosity on flow dynamics can also be neglected. Vessels are usually modeled as rigid tubes with a no-slip boundary condition applied at the walls. Moreover, it is commonly assumed that vessels have a circular cross-section along their length, allowing the flow to be treated as axisymmetric [19].

Under these assumptions the flow within each vessel can be modeled as fully developed Poiseuille flow in rigid, cylindrical tubes (see Section 2.1 for the detailed mathematical formulation).

The effect of the red blood cells

As outlined previously, when the vessel diameter is comparable to the size of an RBC, these cells no longer behave as passive oxygen carriers, but actively shape the hemodynamics of microcirculatory flow. In particular, their deformation and lateral migration modify the velocity profile: instead of the Poiseuille flow observed in cell-free plasma, the presence of RBCs leads to a Couette-like flow, which allows for a description of the cell-free layer present near the vessel walls [12] (see Figure 1.3).

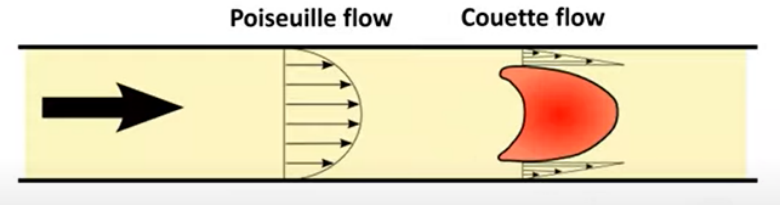

Figure 1.3: Comparison between Poiseuille flow and Couette flow: Poiseuille flow (left) shows a parabolic profile typical of a plasma vessel, while Couette flow (right) illustrates the effect of RBCs on the flow profile. (Image from [12])

The resulting reorganization of the flow has profound implications for microvascular physiology, affecting shear stresses, hydraulic resistance, and solute transport. These flow alterations are captured by three well-established effects:

- the *Fåhræus effect*,
- the *Fåhræus–Lindqvist effect*,
- the *phase separation* at vascular bifurcations.

A proper description of blood flow in the microcirculation therefore requires a systematic analysis of these effects, which are addressed below.

Fåhræus effect

The first of these effects is the Fåhræus effect, which describes how the distribution of RBCs within small vessels modifies the relationship between the local and systemic hematocrit. In order to understand the concept behind this effect, the definition of hematocrit must be introduced. The hematocrit is generally defined as the volume fraction of blood occupied by RBCs. In 1929, Robin Fåhræus, experimentally observed that the hematocrit measured within narrow blood vessels

is lower than the hematocrit of the same blood sample measured in a reservoir. This phenomenon, known today as the Fåhræus effect, arises from the axial migration of RBCs toward the center of the vessel, which leaves a cell-free plasma layer near the vessel walls. As a result, the average concentration of RBCs within small vessels (the tube hematocrit, H_t) is reduced compared to the hematocrit of blood entering or exiting the vessel (the discharged hematocrit, H_d). A representation of these two concepts can be seen in Figure 1.4.

Figure 1.4: Visualization of discharged and tube hematocrit. (Image from [12])

The relationship between H_t and H_d is given by:

$$H_d = \frac{u_{RBC}}{u} H_t, \tag{1.1}$$

where u_{RBC} is the average velocity of the RBCs and u is the average velocity of the blood [12].

Fåhræus observed that $H_t < H_d$, which, according to eq. (1.1), implies that $u_{RBC} > u$. This reflects the fact that RBCs, are predominately in the center of the vessel where the flow is faster, so the average velocity of the RBCs is higher than the velocity of the blood itself.

An empirical relationship between H_t and H_d was obtained by Pries et al. [20] based on experimental data from human RBC suspensions perfused through glass tubes of varying diameters:

$$\frac{H_t}{H_d} = H_d + (1 - H_d)\left(1 + 1.7e^{\alpha D} - 0.6e^{\beta D}\right). \tag{1.2}$$

where D is the vessel diameter. The coefficients α and β are constants with values $\alpha = -0.415\,\mu\text{m}^{-1}$ and $\beta = -0.011\,\mu\text{m}^{-1}$. This empirical relationship was derived from *in-vitro* experiments using glass tubes with diameters ranging approximately from 3 to 100 μm, which correspond to the physiological range of microvessels (capillaries, venules, and arterioles). A graphical illustration of eq. 1.2 is shown in the upper panel of Figure 1.5.

Fåhræus–Lindqvist effect

Closely related to the Fåhræus effect is the Fåhræus–Lindqvist effect, which describes how the apparent viscosity of blood depends on vessel diameter and hematocrit. In small microvessels, RBCs migrate toward the center, creating a plasma layer near the walls that reduces flow resistance compared to a homogeneous suspension.

Experimental studies by Pries et al. [20] showed that the apparent viscosity depends strongly on both the discharge hematocrit H_d and the vessel diameter D. This relationship, depicted in the lower panel of Figure 1.5, reveals that the relative viscosity increases exponentially with hematocrit in larger vessels ($D > 15\,\mu$m), while for smaller diameters ($D < 5\,\mu$m) the dependence on hematocrit is approximately linear. The observed behavior arises from the interplay between RBC deformation, axial accumulation, and interactions with the vessel wall.

The Fåhræus–Lindqvist effect therefore represents a fundamental mechanism governing microcirculatory flow, ensuring efficient capillary perfusion despite elevated hematocrit and the narrow dimensions of microvessels.

Phase separation

Phase separation is an important phenomenon to consider when describing microcirculatory blood flow, as it influences the distribution of RBCs at vessel bifurcations and thereby affects local hematocrit and oxygen delivery. In the microcirculation, when a *parent vessel* splits into two branches, RBCs do not necessarily distribute proportionally to the volumetric blood flow in each branch; this non-uniform partitioning is known as phase separation. Figure 1.2 shows this phenomenon's bifurcation graphically.

The primary mechanism underlying this behavior is the *Zweifach–Fung effect*: RBCs tend to preferentially enter the branch with higher flow. This tendency arises from the deformation and alignment of RBCs along the flow direction, as well as from their axial migration within the parent vessel. Consequently, the higher-flow branch receives a greater fraction of RBCs, while the lower-flow branch draws proportionally more plasma from the near-wall regions and receives fewer RBCs.

In very large vessels (diameter $D > 30\ \mu$m), phase separation is negligible and both RBC and plasma phases behave similarly. In vessels smaller than the size of an RBC, the separation approximates a step function: if the fractional flow into a branch is below 50%, essentially no RBCs enter that branch; if it exceeds 50%, the majority of RBCs follow that path. For intermediate vessel diameters, the transition is smoother and can be empirically described by an *S-shaped* function, as proposed by Pries et al. [20].

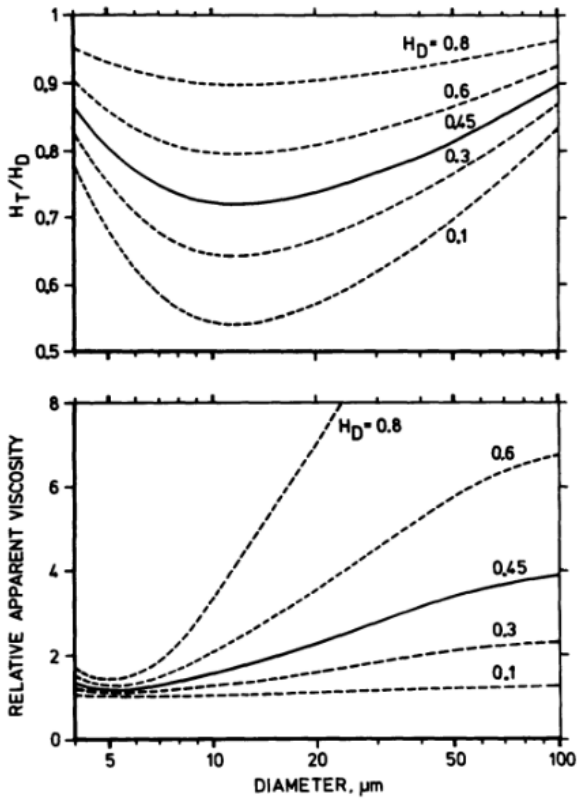

Figure 1.5: Both panels show empirical relations from [20]. Upper panel: Graph showing the Fåhræus effect. The ratio between tube hematocrit (H_t) and discharge hematocrit (H_d) versus tube diameter. Lower panel: Graph showing the Fåhræus-Lindqvist effect. Apparent blood viscosity divided by plasma viscosity (relative apparent viscosity) versus tube diameter.

In summary, RBCs profoundly influence the rheological properties of blood and its spatial distribution in microvessels, both of which critically affect oxygen transport and delivery.

1.1.4 Oxygen transport in the brain

After being transported by the blood flow and carried within RBCs, oxygen must leave the vascular compartment and reach the surrounding tissue in order to oxygenate the cells. This step marks the shift from transport along the microvascular network to exchange across the capillary wall. Through this process, RBC dynamics are directly coupled with the continuous metabolic demands of neuronal tissue, whose activity strongly depends on oxygen availability.

Once released from hemoglobin, oxygen can exist either unbound within RBCs or dissolved in plasma. A continuous exchange between these two fractions occurs as oxygen molecules dissociate from hemoglobin and enter the dissolved phase. To reach the tissue, oxygen must cross two main barriers: the RBC membrane and the capillary wall, beyond which it becomes available for cellular processes.

Due to the dense network of microvessels in brain tissue, the total surface area available for oxygen exchange across the capillary wall between the vasculature and the surrounding tissue far exceeds that of the arteries and veins of the macrocirculation. This high microvascular density ensures a sufficiently large exchange surface.

Oxygen exchange occurs mainly by diffusion, a passive process driven by the random motion of molecules. In the presence of a concentration gradient, molecules move from regions of higher concentration to regions of lower concentration. This behavior is described by Fick's first law, which states that the diffusive flux is proportional to the concentration gradient, with the diffusion coefficient as the proportionality constant. In this specific scenario neuronal cells, through their metabolic consumption of oxygen, locally lower the partial pressure, creating a gradient that promotes the flow of oxygen from the microvessels to the tissue. The small size and non-polar nature of oxygen allow it to cross both RBCs and vascular membranes with little resistance.

The amount of oxygen delivered to the cells directly influences oxidative metabolism and ATP production. Under aerobic conditions, a single glucose molecule yields more than 30 ATP molecules, compared to only 2 produced under anaerobic conditions. When tissue partial pressure is sufficient, the oxygen consumption rate is mainly regulated by the availability of ADP, reflecting the metabolic demand. Conversely, under conditions of low partial pressure, consumption becomes limited by oxygen supply and progressively decreases toward zero [1].

In summary, oxygen delivery to brain tissue depends on a complex interplay between RBC dynamics, diffusion through various compartments, and local metabolic demand.

1.2 *In-vivo* experiments and *in-silico* simulations

Computational models provide a powerful framework to investigate oxygen transport in the brain. Their predictive accuracy depends on experimental data for validation and parameterization. Therefore, a comprehensive understanding of microvascular oxygen transport requires integrating insights from both *in-silico* simulations and *in-vivo* measurements.

Direct measurements in humans are severely limited by ethical and technical constraints. As a result, detailed studies of the cortical microvasculature are typically performed in animal models, particularly mice, whose cortical networks share key structural and functional similarities with humans [21]. To probe oxygen dynamics, different imaging modalities are employed depending on the experimental or clinical context.

Two-photon microscopy and *blood-oxygen-level-dependent functional magnetic resonance imaging* (BOLD fMRI) are among the most widely used techniques. *Two-photon microscopy* enables deep imaging of cortical microvasculature at single-capillary resolution [22]. This technique provides extremely high spatial resolution but is limited to small fields of view, typically in the micrometer range. On the other hand, BOLD fMRI measures changes in the magnetic properties of hemoglobin, providing an indirect readout of local neural activity and vascular oxygenation [23]. BOLD fMRI is able to cover the entire brain, but at a lower (usually millimeter-scale) resolution. These techniques operate at much larger scales, creating a significant imaging gap. Bridging these scales experimentally remains a considerable challenge.

In addition, *in-vivo* experiments often face difficulties in isolating and manipulating specific vascular components without inducing systemic effects, which complicates the study of microvascular alterations such as capillary occlusions or density changes. For instance, recent work by Condrau et al. [24] demonstrates the induction of microstrokes using optical methods, but highlights the difficulty in measuring oxygen levels and monitoring adjacent areas simultaneously.

These limitations highlight the complementary role of *in-silico* modeling, which allows to investigate the effects of individual variables and mechanisms in a controlled, reproducible environment. For example, simulations can evaluate oxygen delivery under varying flow conditions or isolate the impact of a single occluded capillary, free from the physiological noise present in biological systems.

However, accurately modeling oxygen transport is challenging due to the complex, three-dimensional geometry of the capillary network, which is highly interconnected and spatially heterogeneous. This complexity spans multiple spatial scales from the whole brain (centimeters) to cortical regions (millimeters), individual capillaries ($\sim 100\,\mu$m), and down to RBCs ($\sim 10\,\mu$m). Achieving high fidelity across these scales increases computational cost, requiring a balance between accuracy and feasibility.

1.3 History of oxygen transport modeling

In this section, the most important steps of the history of oxygen transport modeling are highlighted. A summary of the main governing eq. is also provided

to illustrate the progressive refinement of modeling approaches from simplified analytical formulations to complex computational frameworks.

The first model for oxygen transport dates back to the work of August Krogh in 1919 [25]. Krogh considered muscle capillaries parallel to muscle fibers and represented the surrounding tissue with an ideal cylindrical domain, now known as *Krogh's cylinder*. He derived the radial steady-state diffusion eq.:

$$\frac{1}{r}\frac{d}{dr}\left(r\frac{dP_{\mathrm{T}}}{dr}\right) = \frac{M_0}{D_{\mathrm{T}}\alpha_{\mathrm{T}}}, \tag{1.3}$$

where P_{T} is the tissue oxygen partial pressure, D_{T} the diffusion coefficient, α_{T} the solubility of oxygen, and M_0 the tissue oxygen consumption rate. With boundary conditions $P_{\mathrm{T}}(r_w) = P_w$ at the capillary wall and $P_{\mathrm{T}}(r_{\mathrm{T}}) = P_{\mathrm{crit}}$ at the outer tissue boundary, integration gives the *Krogh–Erlang eq.*:

$$P_{\mathrm{T}}(r) = P_w - \frac{M_0}{4D_{\mathrm{T}}\alpha_{\mathrm{T}}}\left(r_w^2 - r^2 + 2r_{\mathrm{T}}^2 \ln\frac{r}{r_w}\right). \tag{1.4}$$

This expression determines the minimum capillary oxygen tension required to sustain tissue metabolism.

For nearly fifty years after Krogh's work, most models assumed that the resistance to oxygen transport was dominated by the tissue, neglecting intravascular gradients. This view changed with Hellums (1977) [26], who emphasized the discrete nature of RBCs. By modeling oxygen transport in plasma and across the RBC membrane, he introduced the concept of intravascular resistance, demonstrating that up to 50% of the total oxygen transport resistance could arise within the capillary itself. This work established that the oxygen flux from the RBCs is governed by a partial pressure difference and a mass transfer coefficient. This relationship was formalized in a subsequent model by Hellums [27] using the eq.:

$$J = k_m(P_{\mathrm{pl}} - P_{\mathrm{RBC}}), \tag{1.5}$$

where J is the oxygen flux, P_{pl} and P_{RBC} are the oxygen partial pressures in plasma and inside the RBC, respectively, and k_m is the membrane mass transfer coefficient.

In the following decades, numerous studies examined the other assumptions of Krogh's model, leading to various extensions still based on the original cylindrical geometry. These extensions incorporated factors such as convective transport, axial diffusion, diffusion facilitated by hemoglobin and myoglobin, time-dependent transport, oxygen consumption, oxygen-hemoglobin kinetics, and the influence of carbon dioxide [28].

A decisive advance in the development of models came with the introduction of more realistic geometries. Starting in the late 1970s, Popel [29] studied parallel arrays of capillaries, followed by other authors (e.g. [30], [31]) who highlighted how heterogeneity in oxygen distribution reduced the average tension in tissues [30] and how the irregular arrangement of capillaries increased the heterogeneity of tissue oxygenation [31]. Towards the end of the 1980s, Secomb and Hsu [32] introduced the first model for microvascular networks without predefined assumptions about the regions of tissue supplied by individual vessels. Their approach was based on Green's functions, which reduced the three-dimensional problem of oxygen diffusion to a one-dimensional problem along the capillaries. In their later review [33], the mathematical formulation is presented as follows. The tissue oxygen field P_{T} satisfies the steady-state diffusion eq.:

$$D_{\mathrm{T}}\alpha_{\mathrm{T}}\nabla^2 P_{\mathrm{T}} = M(P_{\mathrm{T}}), \tag{1.6}$$

where $M(P_{\mathrm{T}})$ represents the local oxygen consumption rate. Using Green's functions, P_{T} can be expressed as the superposition of contributions from all capillaries:

$$P_{\mathrm{T}}(\mathbf{x}) = P_0 + \int_{\text{vessels}} q(\mathbf{x}')\, G(\mathbf{x}, \mathbf{x}')\, d\mathbf{x}', \tag{1.7}$$

where $q(\mathbf{x}')$ represents the distribution of source strengths and $G(\mathbf{x}, \mathbf{x}')$ the Green's function describing the response of the tissue to a point source. This approach effectively reduces the 3D diffusion problem to a 1D formulation along the vessel centerlines.

Later, Goldman and Popel [34] proposed a model for oxygen transport from complex capillary networks based on a finite difference method, further contributing to the understanding of the effects of vascular heterogeneity. Additional models then extended the study to arterioles and venules, as described in Goldman's review [28].

More recently, the importance of combining computational models with experimental techniques has been emphasized by Lücker [1]. In his work, Lücker proposed a new computational framework for oxygen transport in the microcirculation designed to fulfill two key requirements. First, the model should take advantage of two-photon phosphorescence lifetime microscopy to allow a direct comparison between simulated and experimentally measured oxygen distributions. Second it provides new insights into the fundamental physics governing oxygen delivery from capillaries to surrounding tissue. Despite these advances, the framework still relies on simplifying assumptions, such as neglecting axial oxygen diffusion and using simplified kinetics between hemoglobin and oxygen, which limit its ability to fully capture the complexity of microvascular oxygen transport.

Overall, the progressive refinement of oxygen transport models, from the early Krogh cylinder to more complex network simulations, has significantly advanced the understanding of microvascular oxygen dynamics, while highlighting the need for continued efforts to connect theoretical predictions with *in-vivo* measurements.

In summary, while *in-vivo* studies provide valuable insights, computational models are indispensable for bridging experimental limitations. By complementing experimental data, *in-silico* simulations offer a detailed and controlled framework to explore how vascular structure influences oxygen delivery and neural function across multiple spatial and temporal scales.

1.4 Thesis Objectives and Structure

While mathematical models are essential tools for studying cerebral oxygen transport, their accuracy depends on the realistic parameterization of key physiological processes. This thesis focuses on improving one such critical parameter: the mass transfer coefficient (MTC), a factor governing the rate of oxygen release from RBCs to plasma. A detailed description of the MTC and its role in oxygen transport will be provided in Chapter 3.

The primary objective is therefore to derive relationships for the MTC from literature data and to integrate a variable formulation that accounts for local variations in hematocrit and oxygen saturation, moving beyond the assumption of a constant value.

To systematically address this goal, the thesis is structured as follows:

- **Chapter 1** establishes the biological foundations of cerebral oxygen transport and gives a general introduction on the modelling.
- **Chapter 2** introduces the mathematical modeling framework for the oxygen transport.
- **Chapter 3** details the derivation of the variable MTC formulation from published data.
- **Chapters 4-5** present the simulation setup, results, and discussion, evaluating the model's performance in both simplified test cases and a realistic microvascular network.
- **Chapters 6** provides conclusions, limitations, and future perspectives.

This structured approach aims to provide a more physiologically realistic representation of oxygen exchange in cerebral microcirculation.

Chapter 2

Mathematical Model for Oxygen Transport

In this chapter, the mathematical model for oxygen transport in cortical microvascular networks is presented. The model was developed as part of the PhD thesis [35] of the candidate, Gaia Stievano, a doctoral researcher at the University of Bern, under whose supervision this work was carried out. The formulation builds on hemodynamic theory for microcirculation, but introduces simplifying assumptions to allow tractable simulations of vascular networks while retaining the essential mechanisms of blood flow and oxygen delivery.

2.1 Blood flow

In the proposed model, blood is treated as a single-phase continuum, where RBCs are assumed to be homogeneously suspended in plasma. Under this assumption, blood behaves as a Newtonian fluid with constant viscosity, and RBCs move at the same velocity as plasma ($u = u_{\mathrm{RBC}} = u_{\mathrm{pl}}$). Consequently, the Fåhræus effect is neglected, and the discharge hematocrit H_d coincides with the tube hematocrit H_t, as it can be deducted from eq. 1.1. The Fåhræus–Lindqvist effect and phase separation at bifurcations are incorporated according to the empirical laws described in Section 1.1.3.

As previously mentioned in Section 1.1.3, the flow in the microcirculation is characterized by very low Reynolds numbers. For instance, the largest Reynolds numbers occur in the *pial vessels*, which have a diameter $D = 200$ μm and velocity $v = 59.9$ mm/s [36], giving $\mathrm{Re} \approx 1.0$. While in capillaries ($D = 4.0$ μm [37], $v = 1.0$ mm/s [38]) it decreases to $\mathrm{Re} \approx 4 \times 10^{-4}$. Since $\mathrm{Re} \leq 1$ throughout the network, inertial contributions can be neglected. In this regime, the Navier–Stokes

eqs. reduce to the Stokes eqs., describing creeping (viscous-dominated) flow of an incompressible fluid:

$$\nabla \cdot v = 0, \tag{2.1}$$

$$-\nabla p + \mu_b \nabla^2 v = 0, \tag{2.2}$$

where v denotes the velocity vector of the blood, p the hydraulic pressure, and μ_b the dynamic viscosity of blood.

At the level of a single vessel, assuming axisymmetric geometry and fully developed laminar flow, integration over the cross-section yields the Poiseuille solution. In this setting, the mass conservation along the vessel centerline s reads:

$$\frac{\partial}{\partial s}\left(A_v \rho_b u\right) = -\frac{\partial}{\partial s}\left(A_v \rho_b \frac{r_v^2}{8\mu_b}\frac{\partial p}{\partial s}\right) = 0, \tag{2.3}$$

where $A_v = \pi r_v^2$ is the cross-sectional area, ρ_b the blood density, u the mean velocity, r_v the vessel radius, and μ_b the blood viscosity.

From this vessel-level description, one can upscale to the entire vascular network. The volumetric flow rate q in a vessel is therefore expressed analogously to Ohm's law:

$$q = \frac{p_{\text{in}} - p_{\text{out}}}{R}, \tag{2.4}$$

where p_{in} and p_{out} denote the pressures at the vessel inlet and outlet, respectively, and R is the hydraulic resistance of the vessel segment. According to Poiseuille's law for laminar flow in cylindrical tubes, the resistance is:

$$R = \frac{8\mu_b}{\pi r_v^4} L, \tag{2.5}$$

with L denoting the vessel length and r_v the vessel radius.

This formulation leads to a linear system obtained from mass conservation at each node, from which pressures and flow rates across the microvascular network are determined.

2.2 Oxygen transport

Oxygen transport and consumption were modeled in a domain consisting of three components: RBCs, plasma, and tissue. The interstitial fluid (i.e., the extracellular fluid that fills the space between tissue cells [39]) is not explicitly modeled, in order to reduce model complexity while preserving the main features of oxygen transport in the tissue. The following assumptions were made: oxygen is consumed only in the tissue; brain tissue is represented as a homogeneous porous medium, which provides a suitable framework for diffusion analysis; in both plasma and RBCs,

oxygen is convected by the blood flow. Furthermore, RBCs contain hemoglobin, which binds oxygen, and therefore the model also accounts for oxygen saturation.

The dissolved oxygen can be quantified by its concentration C $[\mathrm{m}^3\,\mathrm{O}_2\,\mathrm{m}^{-3}]$ and oxygen partial pressure (generally denoted by PO_2 but for simplicity of notation here it is denoted by P), which are related by Henry's law as

$$C = \alpha P, \tag{2.6}$$

where α is the solubility coefficient $\left[\mathrm{m}^3\,\mathrm{O}_2\,\mathrm{mmHg}^{-1}\,\mathrm{m}^{-3}\right]$.

The main processes involved in oxygen transport are summarized in Figure 2.1, where the arrows of different colors highlight the respective mechanisms: grey for hemoglobin–oxygen reaction kinetics, green for RBC–plasma exchange, purple for plasma–tissue transport, and blue for oxygen consumption in the tissue. A comprehensive explanation of these processes is provided below.

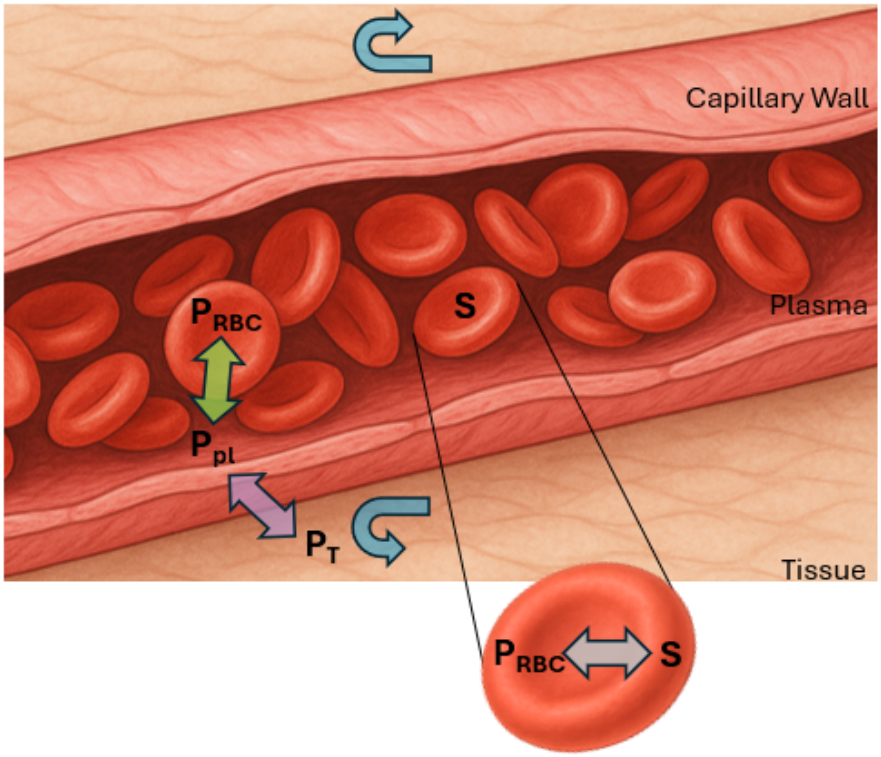

Figure 2.1: The picture describes the processes involved in the oxygen transport. The grey arrow represents the Clark term described in (2.8), the green one represents the Tsoukias rate described in (2.9), the purple one represents the oxygen passing through the vessel walls (2.13), and lastly the blue one describes the oxygen consumption (2.14). (Image from [35])

The first step in describing oxygen distribution is the transition from the bound form to the unbound form of oxygen in hemoglobin. Hemoglobin saturation, denoted by S, represents the ratio of oxyhemoglobin concentration to total hemoglobin concentration.

A complete kinetic description of the reaction between oxygen and hemoglobin in RBCs would require a detailed scheme such as the four-step Adair model [40]. However, the mathematical complexity of this approach is difficult to justify, especially since the reaction rates for the four steps are not well known. For this reason, many previous studies (e.g., [1], [28]) have employed a simpler one-step approximation [41]. In determining the reaction rate F, the strongest experimental constraint comes from equilibrium data: at equilibrium ($F = 0$), the model must reproduce the observed hemoglobin dissociation curve. This curve is well described by the Hill eq.:

$$S = \frac{P_{\mathrm{RBC}}^{n}}{P_{\mathrm{RBC},50}^{n} + P_{\mathrm{RBC}}^{n}}, \tag{2.7}$$

where P_{RBC} is the oxygen partial pressure in RBCs, $P_{\mathrm{RBC},50}$ is the partial pressure at which hemoglobin is half-saturated, and n is the Hill exponent.

To model the reaction rate when oxygen and hemoglobin are not in equilibrium, the approach proposed by Clark et al. [41] is followed:

$$F(S, P_{\mathrm{RBC}}) = K\left(S - (1 - S)\left(\frac{P_{\mathrm{RBC}}}{P_{\mathrm{RBC},50}}\right)^{n}\right), \tag{2.8}$$

where K is the dissociation rate constant [s^{-1}]. This process is represented by the grey arrow in Figure 2.1.

To model oxygen diffusion from RBCs into plasma, Tsoukias et al. [42] introduced a mass transfer eq. that accounts for the exchange of oxygen across the two phases. In this framework, the oxygen flux between RBCs and plasma is given by:

$$j_{\text{RBC-pl}} = k_{\mathrm{cell}}\left(P_{\mathrm{RBC}} - P_{\mathrm{pl}}\right), \tag{2.9}$$

where $j_{\text{RBC-pl}}$ is the oxygen flux per unit surface area, k_{cell} ([$\mathrm{m^3O_2s^{-1}mmHg^{-1}m^{-2}}$]) is the mass transfer coefficient between RBCs and plasma, P_{RBC} is the oxygen partial pressure inside the RBC, and P_{pl} is the oxygen partial pressure in the plasma. The green arrow in Figure 2.1 illustrates this RBC–plasma exchange.

From a physiological perspective, this exchange process is crucial because oxygen must first dissociate from hemoglobin within the RBCs, then dissolve into the plasma before it can diffuse into the surrounding tissue. The partial pressure difference between RBCs and plasma drives this transfer, while the mass transfer coefficient k_{cell} represents the efficiency of oxygen movement across the cell membrane and plasma layer. A detailed analysis of the mass transfer coefficient k_{cell} and its determinants, which is the focus of this work, is provided in Chapter 3.

Oxygen transport from plasma into tissue across the capillary wall can be formally derived starting from the Kedem–Katchalsky theory of coupled solute–solvent transport [43, 44]. In the present model, the convective flux across the vessel wall is neglected, since no transmural fluid exchange is assumed. Under this assumption, the transvascular oxygen flux reduces to the purely diffusive:

$$\hat{q}_C = 2\pi r_v \, K_s \, (C_T - C_{\mathrm{pl}}) \,, \tag{2.10}$$

where r_v is the vessel radius, K_s is the effective permeability coefficient of the vessel wall to dissolved oxygen, C_T is the oxygen concentration in the tissue adjacent to the wall, and C_{pl} is the oxygen concentration in plasma.

Applying Henry's law (eq. (2.6)) near the vessel wall, concentrations are related to partial pressures:

$$C_T = \alpha_w \, P_T, \qquad C_{\mathrm{pl}} = \alpha_{\mathrm{pl}} \, P_{\mathrm{pl}}, \tag{2.11}$$

where α_w and α_{pl} denote the oxygen solubilities in the vessel wall and in plasma, respectively.

Following the work of Koch [45], $\alpha_w = \alpha_{\mathrm{pl}}$ is set and the permeability coefficient K_s as follows:

$$K_s = (1 - \sigma) \frac{D_W}{\delta}, \tag{2.12}$$

where D_W is the diffusivity of oxygen in the vessel wall, δ is the wall thickness, and σ is the oxygen permeability ($\sigma = 0$ for a fully permeable wall and $\sigma = 1$ for an impermeable wall).

Substituting, we obtain the final expression used in this work:

$$\hat{q}_C = 2\pi r_v \, (1 - \sigma) \, \frac{D_W}{\delta} \, \alpha_{\mathrm{pl}} \, (P_T - P_{\mathrm{pl}}) \,. \tag{2.13}$$

Physiologically, this expression describes the diffusive transport of oxygen dissolved in plasma across the capillary wall into the surrounding tissue, driven by the partial pressure difference between plasma and tissue. The factor $(1 - \sigma)$ accounts for the hindrance to oxygen diffusion due to the structure of the capillary wall, while the product $D_W \alpha_{\mathrm{pl}}$ reflects both diffusion and solubility properties of oxygen within the barrier.

Lastly, oxygen reaches the tissue, where it is consumed according to a first-order Michaelis-Menten kinetics, as originally proposed by Goldman [28]:

$$M(P_{\mathrm{T}}) = M_0 \frac{P_{\mathrm{T}}}{P_{\mathrm{T}} + P_{\mathrm{T},50}}, \tag{2.14}$$

where M_0 is the maximal metabolic rate of oxygen consumption, expressed in units of $\mathrm{m^3\,O_2\,m^{-3}\,s^{-1}}$, and $P_{\mathrm{T},50}$ is the oxygen partial pressure at which consumption reaches half of M_0.

This formulation reflects the saturable nature of oxygen consumption by tissue: at low oxygen levels, consumption increases approximately linearly with the available oxygen, while at higher levels it approaches a maximum rate, consistent with the behavior of enzymatic reactions. This process corresponds to the blue arrow in Figure 2.1.

2.3 The mathematical model

All the processes presented in the previous section are described within the model proposed by Stievano [35]. In her work, she describes the oxygen transport using two distinct but interconnected domains: a 1D compartment representing the vasculature network, where oxygen is transported by convection along the vasculature, binds to and unbinds from hemoglobin, and diffuses into the plasma, then a 3D domain representing the brain parenchyma, where oxygen diffuses and is consumed. Let Λ denote the one-dimensional vascular domain, parameterized by $s \in \mathbb{R}$, and by Ω the three-dimensional tissue domain, whose points are $x \in \mathbb{R}^3$. These two domains interact through the vessel walls, where oxygen is exchanged between the plasma and the surrounding tissue. A schematic representation of the two compartments is shown in Figure 2.2.

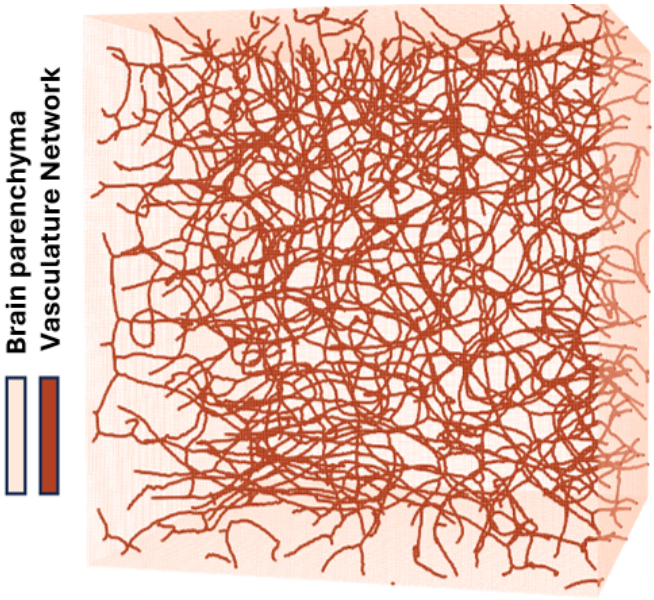

Figure 2.2: 3D porous domain (brain parenchyma) in which the vasculature is embedded. (Image from [35])

In the present formulation, no temporal derivatives appear in the governing eqs.. This reflects the assumption of steady-state conditions, under which the system has reached equilibrium and the oxygen concentrations do not change over time. This simplification is intentionally adopted to focus on the spatial distribution and coupling mechanisms of oxygen transport between the vascular and tissue compartments. Starting from a steady-state framework allows for a clearer understanding of the main transport and exchange dynamics before extending the model to time-dependent scenarios.

1D Vascular Compartment

The 1D vascular compartment Λ is governed by a system of advection-reaction eqs. describing oxygen transport. For all $s \in \Lambda$, the governing eqs. are:

$$\begin{cases} \frac{\partial}{\partial s}\left(A_v \rho_b u\right) = -\frac{\partial}{\partial s}\left(A_v \rho_b \frac{r_v^2}{8\mu_b}\frac{\partial p}{\partial s}\right) = 0 \\ \frac{\partial}{\partial s}\left((1-H_d)A_v u\, \alpha_{\text{pl}} P_{\text{pl}}\right) - A_v \gamma j_{\text{RBC-pl}} = \hat{q}_C \\ \frac{\partial}{\partial s}\left(H_d A_v u\, \alpha_{\text{RBC}} P_{\text{RBC}}\right) - H_d A_v C_0 F(P_{\text{RBC}}, S) + A_v \gamma j_{\text{RBC-pl}} = 0 \\ \frac{\partial}{\partial s}(A_v u\, S) + H_d A_v F(P_{\text{RBC}}, S) = 0 \end{cases} \tag{2.15}$$

Here, the vessel cross-sectional area A_v, which appears in all eqs., is a geometric scaling factor.

The first eq., describes the conservation of mass for blood in the vascular compartment under steady-state and incompressible conditions. It reflects the assumption of laminar flow and relates the volumetric blood flow rate to the axial pressure gradient via Poiseuille's law, as discussed in the previous section.

The second eq. governs the transport of oxygen dissolved in the plasma. The advective term $(1-H_d)u\,\alpha_{\text{pl}}P_{\text{pl}}$ represents the axial transport of oxygen carried in the plasma, where H_d is the discharged hematocrit, and α_{pl} is the plasma oxygen solubility. This transport is affected by two source/sink terms: oxygen transferred from RBCs to the plasma, represented by $j_{\text{RBC-pl}}$, as described in (2.9), and oxygen loss to the surrounding tissue, captured by the sink term $\hat{q}_C$, in accordance with (2.13). The flux $j_{\text{RBC-pl}}$ is multiplied by a geometric factor γ, representing the surface-to-volume ratio of the vessel. This factor has units of $[\text{m}^{-1}]$ and converts the oxygen flux per unit vessel surface into a volumetric source term along the vessel, ensuring dimensional consistency in the eq..

The third eq. describes the transport of oxygen within RBCs. Oxygen is carried in RBCs both in dissolved form and bound to hemoglobin. The advective transport term $H_d u\,\alpha_{\text{RBC}}P_{\text{RBC}}$ accounts for the dissolved component. The source term $H_d C_0 F(P_{\text{RBC}}, S)$ describes the unbinding of oxygen from hemoglobin, where $F(P_{\text{RBC}}, S)$ is a nonlinear function, as described in (2.8), that depends on the oxygen partial pressure within RBCs P_{RBC} and the hemoglobin saturation S. The

term $j_{\text{RBC-pl}}$ accounts for the flux of oxygen from RBCs into the plasma. Here, C_0 denotes the oxygen binding capacity, i.e., the maximum concentration of oxygen that hemoglobin can carry within RBCs.

The fourth eq. models the axial evolution of hemoglobin saturation S. The advective term $u\,S$ accounts for the transport of this intracellular state variable with the blood flow. Since S is a normalized quantity that characterizes each RBC rather than a concentration, its advection does not scale with hematocrit. In contrast, the reactive contribution $H_d F(P_{\text{RBC}}, S)$ is proportional to H_d, because the total binding and release of oxygen depends on the number of RBCs present.

3D Tissue Compartment

The 3D tissue domain Ω is governed by a diffusion-reaction eq., which models the distribution and consumption of oxygen within the tissue:

$$-\nabla \cdot (D_{\text{T}} \alpha_{\text{T}} \nabla P_{\text{T}}) + M(P_{\text{T}}) = q_C, \tag{2.16}$$

Here, the first term accounts for oxygen diffusion in the tissue, with D_{T} denoting the tissue diffusion coefficient and α_{T} the tissue oxygen solubility. The second term, $M(P_{\text{T}})$, represents oxygen consumption according to the Michaelis-Menten kinetics presented in (2.14). The source term q_C captures the oxygen delivered from the vasculature into the tissue.

A key point in this formulation is the distinction between $\hat{q}_C$ and q_C. The term $\hat{q}_C$ denotes the oxygen flux per unit length exchanged across the vessel wall in the 1D vascular framework, while q_C represents the corresponding volumetric source term in the 3D tissue domain.

These quantities are related through a distributional coupling that ensures mass conservation between compartments, which is proved as follow. Let denote the subset of tissue points lying on the vascular surface is indicated by $\Omega_\Lambda \subset \Omega$. The mapping $s(\cdot)$ assigns to each point $x \in \Omega_\Lambda$ its corresponding vascular coordinate s, thereby providing a geometric correspondence between vessel and tissue.

The relationship between the volumetric source term in the tissue, q_C, and the corresponding line source in the vascular network, $\hat{q}_C$, can then be expressed as:

$$\begin{cases} q_C(x) = -\hat{q}_C(s(x))\,\delta_\Lambda(x) & x \in \Omega_\Lambda \\ q_C(x) = 0 & x \in \Omega \setminus \Omega_\Lambda \end{cases} \tag{2.17}$$

where $\delta_\Lambda(x)$ is the Dirac delta distribution supported on the vascular centerline Λ, defined by the property:

$$\int_\Omega f(x)\delta_\Lambda(x)dx = \int_\Lambda f(s)ds \quad \forall f(x) \in L^1(\Lambda). \tag{2.18}$$

To ensure mass conservation, the relationship between q_C and $\hat{q}_C$ must satisfy the following balance for an arbitrary subregion of the domain. Let $\mathcal{V} \subset \Omega$ be an arbitrary subregion of the tissue domain and $\mathcal{V}_\Lambda = \mathcal{V} \cap \Omega_\Lambda$. The oxygen flux entering the tissue within $\mathcal{V}$ originates from the subset of the vasculature embedded in it, denoted by $\mathcal{L} = s(\mathcal{V}_\Lambda)$. Accordingly, the following relation holds:

$$\begin{aligned}
&\int_{\mathcal{V}} q_C(x)\,\mathrm{d}x = \int_{\mathcal{V}} q_C(x)\mathbb{1}_{\mathcal{V}_\Lambda}\mathrm{d}x = \int_{\Omega} q_C(x)\,\mathbb{1}_{\mathcal{V}_\Lambda}(x)\,\mathrm{d}x = \\
&= \int_{\Omega} -\hat{q}_C(s(x))\,\delta_\Lambda(x)\,\mathbb{1}_{\mathcal{V}_\Lambda}(x)\,\mathrm{d}x = \int_{\Omega} -\hat{q}_C(s(x))\,\delta_\Lambda(x)\,\mathbb{1}_{\mathcal{L}}(s(x))\,\mathrm{d}x = \\
&= \int_{\Lambda} -\hat{q}_C(s)\,\mathbb{1}_{\mathcal{L}}(s)\,\mathrm{d}s = \int_{\mathcal{L}} -\hat{q}_C(s)\,\mathrm{d}s. \qquad (2.19)
\end{aligned}$$

Note that by construction, the indicator function $\mathbb{1}_{\mathcal{V}_\Lambda}(x)$ is equal to $\mathbb{1}_{\mathcal{L}}(s(x))$, since a point x belongs to $\mathcal{V}_\Lambda$ if and only if its associated vascular coordinate $s(x)$ belongs to $\mathcal{L}$.

This equality shows that the oxygen flux entering an arbitrary tissue subregion $\mathcal{V}$ in the 3D formulation, $\int_{\mathcal{V}} q_C(x)\mathrm{d}x$, is exactly equal to the flux leaving the corresponding portion $\mathcal{L}$ of the vascular network in the 1D formulation, $\int_{\mathcal{L}} -\hat{q}_C(s)\mathrm{d}s$. In this way, mass conservation between the tissue and vascular domains is rigorously ensured, fully consistent with the numerical implementation based on point-source coupling.

2.3.1 Boundary conditions

For each computational domain, boundary conditions are imposed to represent the physical transport processes operating at the domain interfaces.

1D Vasculature Compartment

The mass conservation eq. requires boundary conditions for the hydraulic pressure p. Let $\partial\Lambda$ denote the boundaries for the 1D compartment. Dirichlet conditions are set:

$$p = p_{\text{bound}} \quad \text{on } \partial\Lambda, \qquad (2.20)$$

where p_{bound} are prescribed hydraulic on the boundary domain. These values are assigned based on the work of Schmid et al. [14], with higher pressures at inlet vessels and lower pressures at outlets.

For the oxygen transport eqs., inflow and outflow boundary conditions are prescribed for plasma, RBCs, and hemoglobin saturation in eqs. 2.21, 2.22 and

2.23[1] [45]. Let $\partial\Lambda_{\text{in}}$ and $\partial\Lambda_{\text{out}}$ denote the inflow and outflow boundaries of the vascular network, respectively.

For the plasma oxygen partial pressure, P_{pl}, the boundary condition is expressed as:

$$\begin{cases} \frac{\partial P_{\text{pl}}}{\partial s} = q\frac{P_{\text{pl}}\alpha_{\text{pl}}(1-H_d)}{A_v\xi_{\text{pl}}} & \text{on } \partial\Lambda_{\text{out}}, \\ \frac{\partial P_{\text{pl}}}{\partial s} = q\frac{P_{\text{pl,in}}\alpha_{\text{pl}}(1-H_d)}{A_v\xi_{\text{pl}}} & \text{on } \partial\Lambda_{\text{in}}. \end{cases} \tag{2.21}$$

At outflow boundaries, the normal derivative of P_{pl} is proportional to the local value of P_{pl}. The relationship accounts for the volume flux q, which is constant within each vessel segment and computed from the network flow solution according to eq. 2.4, the oxygen solubility (α_{pl}), the local plasma volume fraction ($1 - H_d$), and the vascular cross-sectional area (A_v). The term ξ_{pl} acts as a coefficient that converts the pressure-driven transport into an equivalent volumetric oxygen flux (it has units $[\text{m}^3\text{O}_2\,\text{m}^{-1}\,\text{s}^{-1}\text{mmHg}^{-1}]$). At inflow boundaries, the condition instead involves the prescribed inlet plasma oxygen partial pressure $P_{\text{pl, in}}$, thereby setting the incoming oxygen content carried by plasma.

Analogously, the oxygen partial pressure in RBCs, P_{RBC}, satisfies:

$$\begin{cases} \frac{\partial P_{\text{RBC}}}{\partial s} = q\frac{P_{\text{RBC}}\alpha_{\text{RBC}}H_d}{A_v\xi_{\text{RBC}}} & \text{on } \partial\Lambda_{\text{out}}, \\ \frac{\partial P_{\text{RBC}}}{\partial s} = q\frac{P_{\text{RBC,in}}\alpha_{\text{RBC}}H_d}{A_v\xi_{\text{RBC}}} & \text{on } \partial\Lambda_{\text{in}}. \end{cases} \tag{2.22}$$

The boundary condition for oxygen bound to RBCs is analogous to that for plasma. Here, ξ_{RBC} plays a similar role, scaling the RBC-related oxygen flux to reflect the effective cross-sectional transport of RBCs. However, the inlet value $P_{\text{RBC, in}}$ is not uniform across the network: it is assigned based on vessel type, with different prescribed values for arteries, veins, and capillaries to reflect their physiological roles. In capillaries, the inlet RBC oxygen content is further scaled by the local discharge hematocrit H_d, accounting for the heterogeneous distribution of RBCs and the resulting variation in oxygen delivery at the microvascular level (more details are available in Section 4.4).

Finally, the boundary condition for hemoglobin saturation, S, is given by:

$$\begin{cases} \frac{\partial S}{\partial s} = q\frac{S}{A_v\xi} & \text{on } \partial\Lambda_{\text{out}}, \\ \frac{\partial S}{\partial s} = q\frac{S_{\text{in}}}{A_v\xi} & \text{on } \partial\Lambda_{\text{in}}. \end{cases} \tag{2.23}$$

The saturation boundary condition follows the same logic, with outflow boundaries determined by the local saturation and inflow boundaries set by the prescribed

[1]These boundary conditions are implemented in the numerical framework DuMu$^{\text{x}}$ (see Chapter Section 4.1 for details) by specifying oxygen fluxes, which the solver interprets mathematically as Neumann conditions. The coefficients ξ ensure dimensional consistency between physical transport and numerical implementation.

inlet saturation (S_{in}). In this case, ξ is a coefficient with units of effective diffusivity ($[\text{m}^2\text{s}^{-1}]$). It governs the relationship between the convective transport of saturated hemoglobin and the resulting saturation gradient, thereby controlling the rate at which saturation equilibrates along the vessel.

This structure guarantees mass conservation and accounts for the physiological partitioning of oxygen between plasma and RBCs.

3D Tissue Compartment

In the tissue domain Ω, homogeneous Neumann boundary conditions are imposed on the boundary $\partial\Omega$:

$$\nabla P_{\text{T}} \cdot \mathbf{n} = 0 \quad \text{on } \partial\Omega, \tag{2.24}$$

where $\mathbf{n}$ denotes the normal vector to the tissue boundary. This zero-flux condition represents an impermeable set up at the tissue boundaries, preventing oxygen exchange with the external environment. As a result, tissue oxygen dynamics arise only from diffusion and from exchange with the embedded vascular network.

Chapter 3

Mass Transfer Coefficient

This chapter addresses the mass transfer coefficient (MTC), a critical parameter governing the rate of oxygen release from RBCs to plasma. The primary focus of this work is to evaluate and implement dynamic MTC formulations within a computational model of cerebral oxygen transport, moving beyond the common simplification of a constant coefficient.

The exchange of oxygen between RBCs and plasma is described by eq. (2.9). According to this formulation, the rate of oxygen exchange is driven by the partial pressure gradient between RBCs and plasma, $(P_{\mathrm{RBC}} - P_{\mathrm{pl}})$, and is modulated by the MTC k_{cell} ($[\mathrm{m^3O_2s^{-1}mmHg^{-1}m^{-2}}]$). The k_{cell} quantifies the oxygen transfer efficiency across the RBC membrane and through the surrounding plasma, and it can be interpreted as the inverse of the intravascular resistance to oxygen transport. A high value of k_{cell} reflects more efficient transfer, whereas a low value indicates a more substantial barrier to diffusion.

Building on the biological and mathematical foundations discussed in the previous chapters, this work now introduces the notations and conventions used throughout the study:

- k_{cell}: Generic mass transfer coefficient
- k_C: Constant MTC formulation
- k_L: MTC formulation derived from Lücker [1]
- k_V: MTC formulation derived from Vadapalli et al. [2]

In many existing models, such as the one proposed by Stievano [35], the MTC is treated as a constant parameter (k_C). However, several studies [1, 2, 42] demonstrate that k_{cell} is a variable parameter, varying with local physiological conditions like hematocrit and oxygen saturation. This work specifically investigates the formulations k_L and k_V, which express the MTC as a function of these variables.

The core objective is to analyze how these variable MTCs influence oxygen transport heterogeneity. To this end, the functions k_L and k_V were derived from the literature and implemented into the computational framework described in Chapter 2. A systematic numerical analysis was conducted, progressing from simplified scenarios to a realistic microvascular network. This approach allowed for the isolation of the MTC's effect and the assessment of its impact on both intravascular and tissue oxygen distributions.

The results provide new insights into the coupling between microvascular hemodynamics, oxygen release kinetics, and tissue oxygenation. Incorporating a physiologically grounded, variable MTC enhances the model's biological fidelity and its ability to simulate cerebral oxygenation in both health and disease.

3.1 MTCs in literature

Early models of microvascular oxygen transport, such as those proposed by Goldman et al. [19], adopt a simplified approach in which the oxygen partial pressure is assumed to be uniform across the entire blood compartment. This simplification effectively eliminates the need to consider any resistance to oxygen diffusion between RBCs and plasma, and consequently, it does not include the MTC. Indeed, under this condition, the gradient of pressure in (2.9) becomes null.

To address these limitations, other models introduced distinct partial pressures for RBCs and plasma, thereby acknowledging the presence of an intravascular resistance to oxygen diffusion. In these formulations, the MTC k_{cell} is used to characterize the rate of oxygen exchange across the RBC-plasma interface. Commonly, k_{cell} is treated as a constant parameter derived from empirical data, such as in the work by Hellums [27], but this constant approach may still oversimplify the complexity of the actual physiological environment, neglecting local condition impact.

An alternative class of models, such as those developed by Popel et al. [46], explicitly account for the discrete geometry and movement of RBCs within capillaries. These models describe RBCs as individual entities, often represented as cylinders traveling through the microvasculature, and explicitly simulate the spatio-temporal evolution of oxygen exchange. In this context, the overall resistance to oxygen transport is modeled as a series of components, including the intraerythrocyte resistance, the plasma sleeve, and the plasma gap. Each component contributes to the total resistance, and the MTC is defined as the inverse of the total resistance of the capillary segment. An illustration of the model here presented is reported in Figure 3.1. Despite their accuracy, such discrete resistance models have a very high computational cost, for example because they require resolving fine-scale spatial

gradients of oxygen within and around RBCs, and are therefore usually applied to single vessel studies or to simplified geometrical configurations. This level of detail,

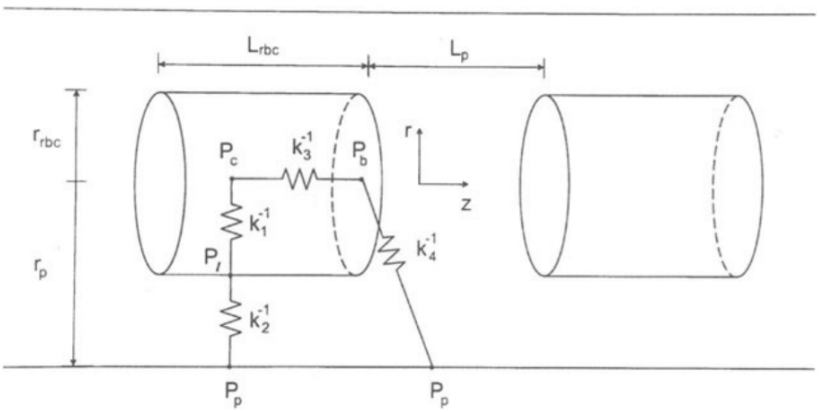

Figure 3.1: Intracapillary geometry proposed by Popel et al. [46], where MTCs are computed using a series of resistances. (Image from [46])

however, cannot be directly applied to the model presented in Chapter 2, where RBCs are not represented as discrete entities but rather as part of a continuum description of the blood phase.

Other models also explore the nonlinear dependence of k_{cell} on physiological variables. For example, the works of Lücker [1] and Vadapalli et al.[2], whose approaches are particularly relevant for this thesis.

In the work by Lücker [1], the authors investigate the respective roles of hematocrit, RBC velocity, and RBC flux on tissue oxygenation using a combination of analytical and numerical models. His results highlight that, for a fixed RBC flux, an increase in hematocrit leads to a rise in tissue oxygen partial pressure, primarily due to a reduction in intravascular resistance to oxygen diffusion. One of the key findings is the significant dependence of the MTC on the hematocrit, especially at low hematocrit levels as shown in Figure 3.2.

Although the original study focuses on tissue oxygenation and the interaction between hematocrit and flow, the present work relies only on a subset of their results: specifically, the relationship between the MTC and hematocrit. The analytical trend reported in the figures of their paper is used as a functional representation of k_{cell} in the continuum-based model presented in this work.

In the study by Vadapalli et al. [2], the authors developed a detailed theoretical model to investigate oxygen transport in capillary-sized vessels in the presence of hemoglobin-based oxygen carriers (HBOCs). Their model explicitly simulates

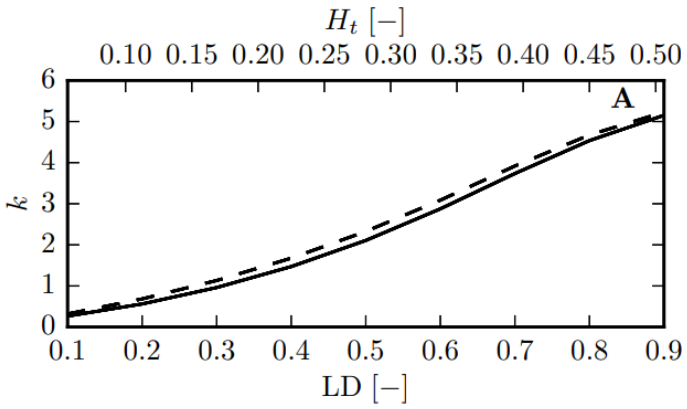

Figure 3.2: Mass transfer coefficient k_{cell} as a function of tube hematocrit H_t, reproduced from Lücker et al. [1]. The original linear density axis is omitted as it is directly related to H_t and thus redundant for the analysis. Solid and dashed lines represent red blood cell velocities (u_{RBC}) of 0.2 mm/s and 2.4 mm/s, respectively.

individual RBCs, represented with realistic parachute-like geometry, and includes both free and hemoglobin-facilitated oxygen transport, as well as reaction kinetics in RBCs and plasma, however the authors also present results in terms of MTCs that relate oxygen fluxes to effective pressure gradients. In this work, the full model proposed by Vadapalli is not adopted, but rather the empirical trend reported in the results of the paper, specifically the functional dependence of the MTC on hematocrit and oxygen saturation (see Figure 3.3).

3.2 MTC Functions

To incorporate variable MTCs (k_{cell}) into the oxygen transport model, functional relationships were extracted from the literature. Specifically, empirical trends were obtained from figures reported by Lücker [1] and Vadapalli et al.[2], which describe the dependence of k_{cell} on hematocrit and, in the case of Vadapalli, also on oxygen saturation. The extracted data were then fitted using analytical functions. The selection of appropriate functional forms involved testing several candidate eqs., with the final choice determined by optimizing the trade-off between fitting accuracy and physiological plausibility. Particular attention was paid to maintaining biologically sensible characteristics, such as positive values and monotonic behavior where physiologically justified. The resulting functions are discussed in detail below.

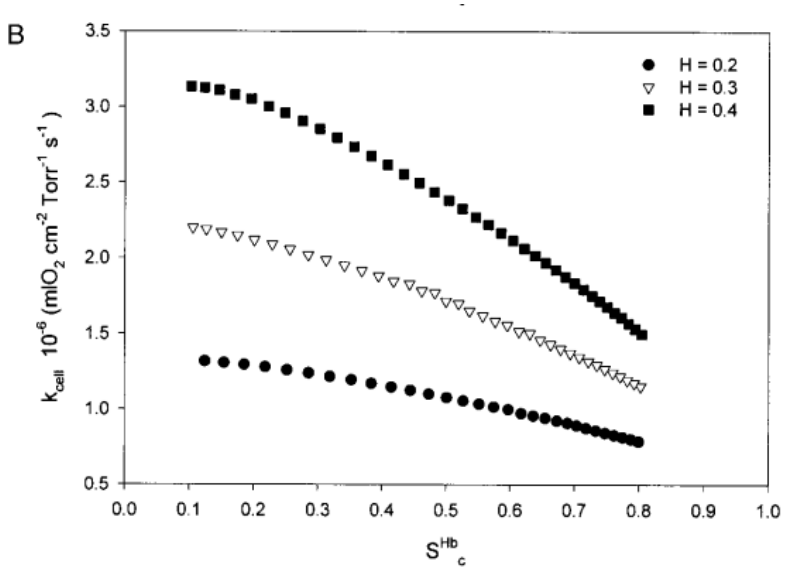

Figure 3.3: Data from Vadapalli et al. [2], showing the variation of k_{cell} with oxygen saturation S for three different values of tube hematocrit: $H_t = 0.20$, $H_t = 0.30$, and $H_t = 0.40$.

3.2.1 Lücker

To incorporate the hematocrit-dependent MTC proposed by Lücker [1], the function $k_{\text{L}}(H_t)$ is defined as an approximation of the mass transfer coefficient k_{cell}. Data extracted from the publication (Figure 3.2) show the relationship between k_{L} and tube hematocrit H_t[1].

A key limitation of the data obtainable from the published plots is the restricted range of hematocrit, spanning approximately from $H_t \approx 0.07$ to $H_t = 0.50$. However, by definition, the tube hematocrit spans the full interval $H_t \in [0.00, 1.00]$. Therefore, to define a continuous function over the entire physiological domain, an extrapolation strategy was required both below and above the range of values

[1]Before implementing these functions in the oxygen transport model, it was necessary to convert the discharge hematocrit values H_d into tube hematocrit H_t. Since both Lücker [1] and Vadapalli et al.[2] express the MTC k_{cell} as a function of H_t, while the present model formulation is based on the discharged hematocrit H_d.

To ensure consistency between the empirical functions and the model variables, the transformation was carried out using the empirical relationship proposed by Pries et al. [20], already introduced in Section 1.1.3 (see eq. (1.2)).

directly accessible from the plots.

To first reproduce the data within $H_t \in [0.07, 0.50]$, a fifth-degree polynomial was fitted to the points shown in Figure 3.2. This interpolation provided a smooth representation of $k_{\mathrm{L}}(H_t)$:

$$k_{\mathrm{L}}(H_t) = \Big(a_5 H_t^5 + a_4 H_t^4 + a_3 H_t^3 + a_2 H_t^2 + a_1 H_t + a_0\Big) \cdot 10^{-8}. \tag{3.1}$$

The values of the fitted coefficients a_i in eq. (3.1) are reported in Table 3.1.

Coefficient	**Value**
a_5	-394.354
a_4	380.475
a_3	-132.173
a_2	36.737
a_1	1.804
a_0	0.065

Table 3.1: Fitted polynomial coefficients for $k_{\mathrm{L}}(H_t)$.

This polynomial degree was selected as it preserved the monotonic increasing trend observed in the data throughout the interval, without compromising the quality of the fit.

At the lower boundary of the domain, the fitted polynomial was also used to extend the function to $H_t \in (0.00, 0.07]$, exploiting its monotonic behavior for $H_t \to 0.00$. This guarantees both continuity and smoothness in the transition toward the origin. The polynomial yields a small positive value at $H_t = 0.00$ ($k_{\mathrm{L}}(0) = a_0 \cdot 10^{-8} \approx 6.5 \times 10^{-10}$).

While one could, in principle, enforce the physically correct boundary condition $k_{\mathrm{L}}(0) = 0$ directly within the fitting process, this would have compromised the quality of the fit in the low hematocrit range ($H_t \in [0.07, 0.50]$) where data are available and the numerical stability of the model. The chosen polynomial form, optimized for the available data range, does not naturally pass through zero. Therefore, to satisfy both the physical constraint of negligible oxygen exchange at zero hematocrit and the requirements of numerical stability, the MTC value at $H_t = 0.00$ was set to:

$$k_{\mathrm{L}}(H_t = 0.00) = k_{\mathrm{L0}} = 10^{-12}\ \ \mathrm{m^3O_2\ s^{-1}\ mmHg^{-1}\ m^{-2}}.$$

This value is two orders of magnitude smaller than the polynomial's extrapolation and ensures no unphysical oxygen transfer occurs while maintaining solver robustness.

Having addressed the lower boundary with the polynomial fit, the next step was to extend the function beyond the last extracted data point from Figure 3.2 ($H_t > 0.50$). To this end, two extrapolation approaches were considered:

- **Constant extension**: for $H_t > 0.50$, the value of k_L was held constant and equal to the value at the last extracted point:

$$k_\mathrm{L}^{\mathrm{const}}(H_t) = \begin{cases} k_\mathrm{L}(H_t) & \text{if } H_t \leq 0.50, \\ k_\mathrm{L}(0.50) & \text{if } H_t > 0.50, \end{cases} \tag{3.2}$$

where $k_\mathrm{L}(H_t)$ is given by eq. (3.1). The constant extension was chosen as the primary method for extrapolation in this work. By assuming the MTC does not increase beyond its value at $H_t = 0.50$, the model avoids overestimating oxygen exchange efficiency at high hematocrit levels where robust literature data for cerebral capillaries are scarce.

- **Tangent extension**: for $H_t > 0.50$, the function was extended linearly using the tangent line at $H_t = 0.50$:

$$k_\mathrm{L}^{\mathrm{tan}}(H_t) = \begin{cases} k_\mathrm{L}(H_t) & \text{if } H_t \leq 0.50, \\ k_\mathrm{L}(0.50) + k_\mathrm{L}'(H_t)\Big|_{H_t=0.50} \cdot (H_t - 0.50) & \text{if } H_t > 0.50, \end{cases} \tag{3.3}$$

where $k_\mathrm{L}'(H_t)$ denotes the derivative of Eq. (3.1). The tangent extension is retained for sensitivity analysis. This allows quantification of how sensitive the model predictions are to a potentially increasing MTC beyond the data range, providing bounds for the uncertainty associated with the extrapolation.

Figures 3.4 and 3.5 show a comparison between the two extension methods applied to the fitted curve.

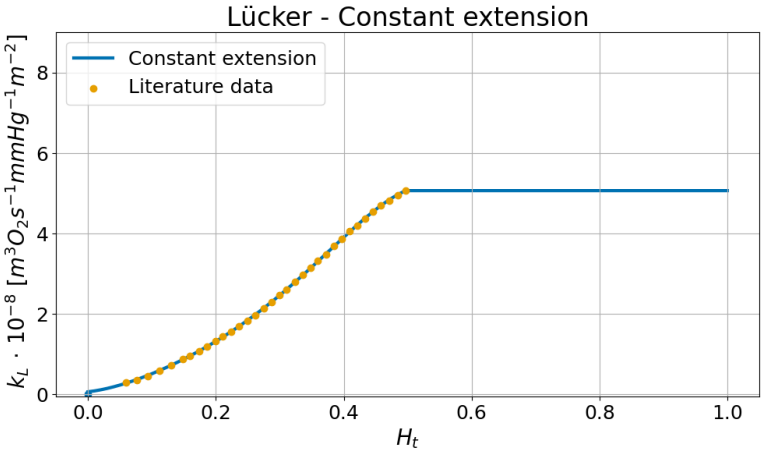

Figure 3.4: Extrapolation by assigning a constant value for $H_t > 0.50$ according to Lücker [1].

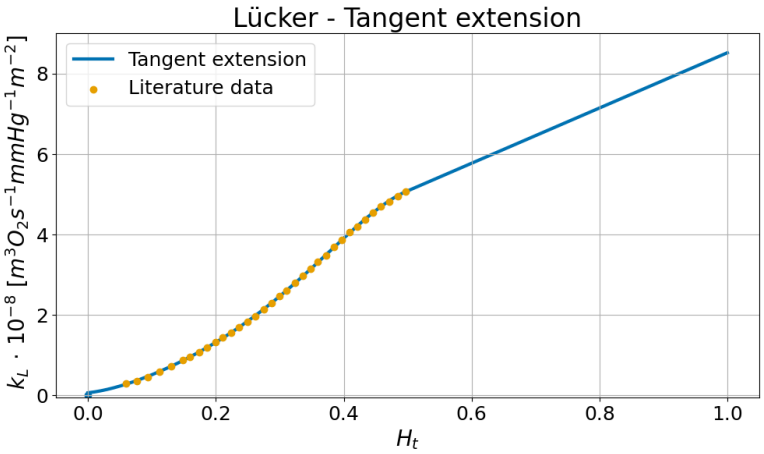

Figure 3.5: Extrapolation obtained by linear extension of the tangent at $H_t = 0.50$ according to Lücker [1].

An alternative representation of the Lücker data, not used in the main analysis, is provided in Appendix B.

3.2.2 Vadapalli

The data from Vadapalli et al. [2] were extracted from a figure reporting the MTC as a function of the saturation for three different values of H_t[1] (see Figure 3.3). Based on this data, the function $k_V(H_t, S)$ is defined as an approximation of the mass transfer coefficient k_{cell}.

The original data cover a limited physiological domain, with oxygen saturation values ranging from $S = 0.10$ to $S = 0.80$, and only three discrete values of tube hematocrit: $H_t = 0.20$, 0.30, and 0.40. However, the full physiological domain is $S \in [0.00, 1.00]$ and $H_t \in [0.00, 1.00]$. To define a continuous and smooth function across this entire range, a global analytical expression was fitted to the data:

$$k_V(H_t, S) = \exp\left(b_0 + b_1 S + b_2 S^2 + b_3 S^3\right) \cdot \left(c_0 + c_1 H_t + c_2 S H_t + c_3 S^2 H_t + c_4 S^3 H_t\right) \cdot 10^{-8}. \quad (3.4)$$

The coefficients b_i and c_i used in eq. (3.4) are summarized in Table 3.2.

This function ensures non-negative values over the domain and reflects the trends observed in the data. A visualization of the resulting surface is shown in Figure 3.6.

Coefficient	Value
b_0	$-1.363 \cdot 10^1$
b_1	0.877
b_2	0.971
b_3	-3.048
c_0	1.000
c_1	$6.632 \cdot 10^6$
c_2	$-8.926 \cdot 10^6$
c_3	$3.345 \cdot 10^6$
c_4	$4.628 \cdot 10^6$

Table 3.2: Coefficients for the expression of $k_V(H_t, S)$.

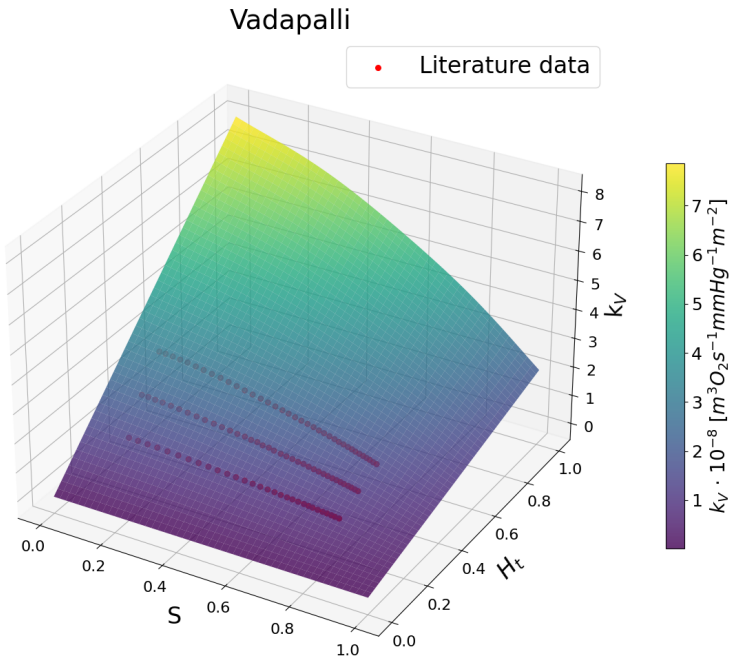

Figure 3.6: Interpolated surface $k_V(H_t, S)$ based on data from Vadapalli et al. [2].

The function exhibits a linear increasing trend with respect to H_t for fixed values of S, and a non-linear decreasing trend with respect to S for fixed H_t, as shown in Figure 3.7.

The analytical expression for $k_V(H_t, S)$ yields numerically critical values (on the order of 10^{-16}) for certain combinations of H_t and S, particularly at extremely low hematocrit or extreme saturation levels. Numerical tests confirmed that such

(a) (b)

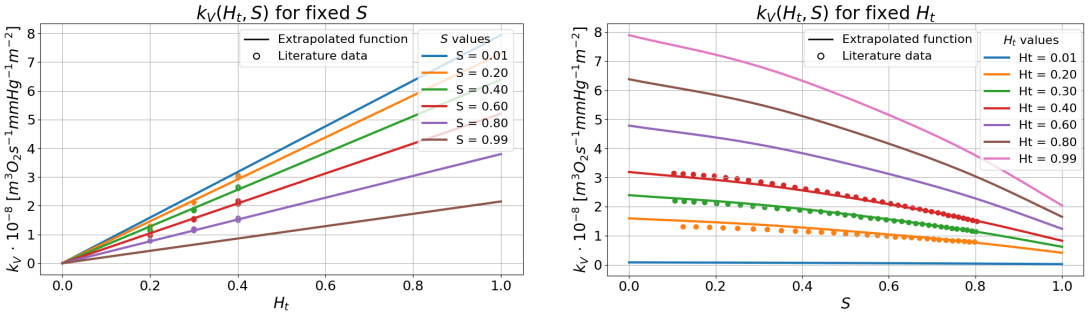

Figure 3.7: Behavior of the MTC k_V from Vadapalli et al. [2] based on the fitted analytical expression. (a) Variation of k_V with tube hematocrit H_t for different values of oxygen saturation S. (b) Variation of k_V with oxygen saturation S for different values of tube hematocrit H_t.

small values cause instability in the simulations. To ensure numerical stability, such values were bounded from below by imposing a threshold:

$$k_V(H_t, S) := \max\left(k_V(H_t, S),\, k_{V0}\right) \tag{3.5}$$

where $k_{V0} = 10^{-12}$ $\mathrm{m^3O_2s^{-1}mmHg^{-1}m^{-2}}$.

This ensures that the Tsoukias rate (2.9) remains well-defined across the entire domain, without significantly affecting the physical interpretation of the model at low hematocrit or saturation levels.

3.2.3 Biological interpretation

The observed trends of the fitted functions $k_L(H_t)$ and $k_V(H_t, S)$ are consistent with physiological mechanisms governing oxygen transport. The increasing behavior of both functions with respect to hematocrit H_t reflects the higher concentration of RBCs within the vessel. As H_t increases, the average spacing between RBCs decreases, resulting in narrower plasma gaps (regions through which oxygen must diffuse before reaching the capillary wall). This reduces the diffusion distance and enhances the efficiency of oxygen release events. This aspect is deeply discussed in [27].

Conversely, the decreasing behavior of k_V with respect to oxygen saturation S can be attributed to the reduced efficiency of facilitated diffusion by hemoglobin at higher saturation levels. Near full saturation, most hemoglobin binding sites are occupied, and the ability of RBCs to store and release additional oxygen decreases.

Since the facilitated component of oxygen transport depends on the slope of the oxygen dissociation curve, the overall mass transfer from RBCs to plasma becomes less effective at high S, thereby reducing the effective MTC. This behaviour is a consequence of the physiology of oxygen binding: the affinity of hemoglobin for oxygen changes more sensitively at intermediate saturations, where small changes in partial oxygen pressure cause large changes in saturation (as can be deducted from the hemoglobin–oxygen dissociation curve reported in [47]). This high sensitivity improves facilitated diffusion and thus increases the effective MTC k_{V}.

These dependencies support the use of $k_{\mathrm{L}}(H_t)$ and $k_{\mathrm{V}}(H_t, S)$ as functional MTCs in the model.

Chapter 4

Simulation Setup

To investigate the influence of different MTC expressions, a series of simulations was performed. Three different configurations were evaluated: a constant coefficient, and two empirical functions derived from data reported in the studies by Lücker and Vadapalli, discussed in the previous chapter. The simulations were designed to progressively increase in complexity, covering both an idealized and a realistic vascular configuration.

Specifically, two main scenarios were analyzed. The first consists of a single blood vessel (SV), representing a simplified configuration that allows isolating and understanding the local effects of each MTC formulation under controlled conditions. In this setup, the vessel geometry, flow rate, and boundary oxygen concentrations were prescribed to reproduce physiologically meaningful conditions while keeping the system analytically and numerically tractable.

The second scenario involves a realistic microvascular network (MVN), extracted from the somatosensory cortex of a mouse. This configuration captures the spatial heterogeneity of vessel diameters, hematocrit distribution, and flow conditions typical of brain microcirculation, providing a more comprehensive assessment of how the MTC formulations perform under physiologically realistic conditions.

Both configurations were simulated using the model presented in Chapter 2 and parameter set to ensure a consistent comparison between the different MTC expressions. The implementation of the governing eqs. and the numerical solution of the coupled problem were carried out using the open-source framework DuMu$^{\mathrm{x}}$, whose structure and main features are briefly introduced in the following section.

4.1 DuMu$^{\mathrm{x}}$

DuMu$^{\mathrm{x}}$ is an open-source framework developed for the numerical modeling of complex flow and transport processes in porous media. It is based on the DUNE

framework (Distributed Unified Numerics Environment), an open-source scientific numerical software framework for solving partial differential eqs. [48].

One of the central features of DuMu^{x} is the systematic use of the finite volume method (FVM). This approach ensures local conservation of physical quantities and robustness in solving strongly coupled balance eqs.. DuMu^{x} provides three main variants of the FVM: *box method*, *cell-centered finite volume*, and *staggered grid*. In this work, the governing eqs. were discretized using the cell-centered finite volume method. In this scheme, each element of the grid coincides with a control volume, and the variables are defined at the volume centers [49]. Fluxes across the cell faces are approximated using the *Two-Point Flux Approximation* (TPFA), which evaluates the transmissibility based only on the values of the two neighboring cells [49]. This choice ensures computational efficiency on grids. Although TPFA is less accurate on highly distorted meshes, it represents a standard and reliable approach for porous media flow problems.

The resulting discrete non-linear system of eqs. is solved using the *Newton method*. In this approach, the governing eqs. are implemented in residual form. For a general non-linear problem $\mathbf{F}(\mathbf{u}) = \mathbf{0}$, the residual function $\mathbf{r}(\mathbf{u})$ is defined as:

$$\mathbf{r}(\mathbf{u}) = \mathbf{F}(\mathbf{u}),$$

where $\mathbf{r} : \mathbb{R}^n \to \mathbb{R}^n$ is the residual operator, $\mathbf{u} \in \mathbb{R}^n$ is the vector of primary variables, and n is the number of eqs.. The solution strategy aims to find $\mathbf{u}^*$ such that $\mathbf{r}(\mathbf{u}^*) = \mathbf{0}$. Newton's method iteratively improves an initial guess $\mathbf{u}^0$ by assembling the Jacobian matrix $\mathbf{J}_r(\mathbf{u}^i)$ at each iteration i:

$$\mathbf{J}_r(\mathbf{u}^i) = \frac{\partial \mathbf{r}}{\partial \mathbf{u}}(\mathbf{u}^i),$$

where the Jacobian represents the sensitivity of the residual to changes in the primary variables.

At each Newton step, the linear system:

$$\mathbf{J}_r(\mathbf{u}^i)\,\Delta\mathbf{u}^i = -\mathbf{r}(\mathbf{u}^i)$$

is solved for the update $\Delta\mathbf{u}^i$, which represents the correction vector. The solution is then updated using the standard Newton update:

$$\mathbf{u}^{i+1} = \mathbf{u}^i + \Delta\mathbf{u}^i.$$

The relative shift criterion terminates the algorithm when the solution vector does not change significantly between iterations. This criterion computes the

maximum relative difference of any degree of freedom between the current and previous iteration:

$$\max_{j=1,\dots,n} \left(\frac{|u_j^{i+1} - u_j^i|}{\max(|u_j^{i+1} + u_j^i| \cdot 0.5, 1.0)} \right) < \epsilon_{\text{shift}},$$

where u_j^i is the j-th entry of the solution vector at iteration i, and ϵ_{shift} is a user-defined parameter.

To ensure physical consistency of the solution, a *chopped Newton method* [50] is employed. The adjective chopped refers to the fact that, during the Newton iterations, the updated primary variables are constrained to remain within physically admissible ranges (e.g., saturations between 0 and 1). If a Newton update would drive a variable outside its valid range, its value is "chopped" back to the closest admissible bound. This strategy prevents the occurrence of non-physical intermediate states, while preserving the convergence properties of Newton's method.

In the considered problem, the three-dimensional tissue domain and the one-dimensional vascular network are treated as two separate subproblems (*TissueTransportProblem* and *NetworkTransportProblem*). Each subproblem defines its own initial and boundary conditions, as previously discussed in Section 2.3.1, while the interaction between the domains is handled by a *coupling manager* [51], which governs the mass exchange across the vessel wall.

To implement this coupling numerically, the Cylinder Surface Method is used [52]. Each vessel (denoted with θ) is represented as a sequence of edges $i \in [1, ..., n_\theta]$ (more details on the graph structure of the network explained in Section 4.3). For each 1D element, denoted by its midpoint $\lambda_{i,\theta}$, we consider the cylindrical surface C_θ centered at $\lambda_{i,\theta}$ with vessel radius r_v. The Cylinder Surface Method identifies the set of tissue control volumes $\mathcal{K}_{i,\theta}$ that intersect this surface; these elements provide an approximation of the cylindrical tissue region surrounding the vessel. The local source term is then computed as:

$$\hat{q}_{C,(i,\theta)} = D_W \alpha_{\text{pl}} (1 - \sigma) \left(P^{\bigcirc}_{\text{T},(i,\theta)} - P_{\text{pl},(i,\theta)} \right) |C_\theta|, \tag{4.1}$$

where $P^{\bigcirc}_{\text{T},(i,\theta)} = \frac{1}{|C_\theta|} \int_{C_\theta} P_{\text{T}}$ is the average tissue oxygen pressure along the cylinder circumference C_θ, $P_{\text{pl},(i,\theta)}$ is the plasma pressure at $\lambda_{i,\theta}$, and $|C_\theta|$ is the circumference length. The source term $q_{C,(i,\theta)}$ is then obtained distributing $\hat{q}_{C,(i,\theta)}$ over the intersecting volumes $\mathcal{K}_{i,\theta}$ to represent the oxygen flux from the vessel to the surrounding tissue.

In this method, the distribution of P_{T} inside the cylinder $\mathcal{C}_{i,\theta}$ is computed assuming that the oxygen flux is applied on its boundary. However, the portion of $\mathcal{C}_{i,\theta}$ that overlaps with the vasculature is physically governed by the 1D vascular

oxygen transport eqs., and therefore this approximation introduces embedding errors. Nevertheless, these errors remain small in practice, since the overlap region is significantly smaller than the surrounding tissue volume considered for diffusion.

In this way, the 3D–1D coupling effectively represents the mass flux exchanged through the vascular surface, enabling a consistent simulation of solute transport between the vascular network and the surrounding tissue [51].

4.2 Single Vessel

The first simplified scenario was introduced to test and isolate the effects of different MTCs under controlled conditions. This allowed for a detailed analysis of how each coefficient influences oxygen transport, without the added complexity introduced by the network topology.

The geometry considered consists of a single straight cylinder, resembling a capillary, embedded in a surrounding tissue domain. The vessel has a diameter of 4 μm, a length of 50 μm, and is aligned with the depth of a three-dimensional parallelepiped representing the tissue. The other two lateral faces of the domain are squared, each with an edge length of 100 μm. This configuration ensures that the vessel is located 50 μm away from the domain boundaries, which corresponds to the typical diffusion influence range of a single capillary [53]. The geometry of the simplified configuration is illustrated in Figure 4.1.

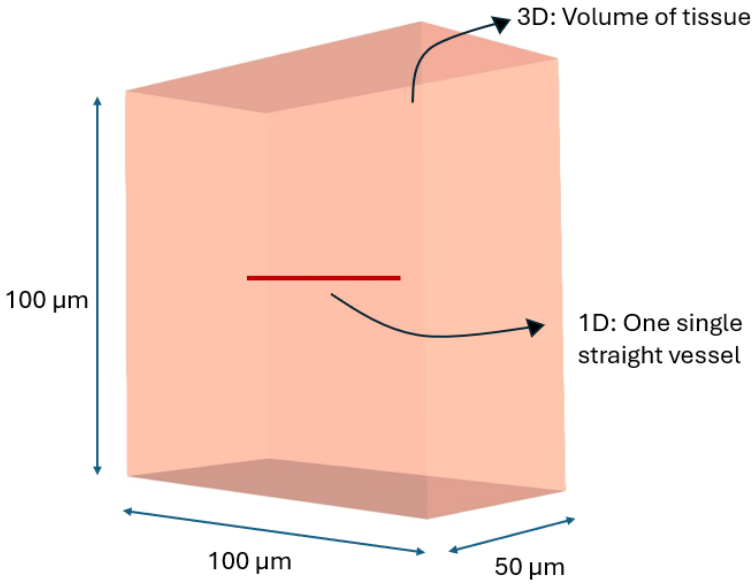

Figure 4.1: Schematic representation of the SV simulation domain.

Since one single vessel is considered, the hematocrit remains constant throughout the entire 1D domain. As discussed in Chapter 3, the MTC functions may depend on H_d; therefore, multiple simulations were performed, varying the value of H_d. For clarity and to avoid redundancy, only the cases with $H_d = 0.10$ (from law (1.2) $H_t = 0.08$) and $H_d = 0.90$ ($H_t = 0.88$) are presented here, as they capture the most notable differences while preserving the qualitative trends observed across intermediate values. (For other cases see Appendix A.1)

To isolate the effect of the analyzed MTC, the blood flow was prescribed and kept constant across all simulations (with a value of $1.26 \cdot 10^{-14}\mathrm{m}^3\mathrm{s}^{-1}$), removing the confounding influence of hemodynamic changes. To ensure physiologically realistic flow conditions, the pressure values at the inlet and outlet of the vessel were adjusted according to Poiseuille's law. For each hematocrit case, the apparent blood viscosity and thus the hydraulic resistance were updated based on the corresponding hematocrit value. In this simplified setup, the desired discharge hematocrit H_d was directly imposed in the vessel, and the pressure difference between the two ends was set such that the resulting flow rate matched a physiologically plausible value according to Poiseuille's law (see eq. (2.4) and eq. (2.5)).

Three different formulations for k_{cell} were tested and compared in the SV setup.

The first scenario assumes a constant value for the MTC, denoted as k_{C}. The value $k_{\text{C}} = 3.73 \cdot 10^{-8}\,\mathrm{m}^3\mathrm{O}_2\mathrm{s}^{-1}\mathrm{mmHg}^{-1}\mathrm{m}^{-2}$ is used uniformly across the domain. This reference value was chosen as the MTC computed evaluating Lücker function (3.1) at $H_d = 0.45$, which corresponds to the average hematocrit in the human brain [54]. This constant provides a baseline for comparison against variable formulations.

The second approach uses Lücker-based MTC, derived from the empirical polynomial fit introduced in Section 3.2.1. This model is originally defined for tube hematocrit values H_t between 0.00 and 0.50. Cases with $H_t > 0.50$ were handled using the extensions proposed in the previous chapter: a constant extension (eq. (3.2)) and a tangent extension (eq. (3.3)). In the case with $H_d = 0.10$, the corresponding H_t lies within the valid range of the original data, so both options yield the same coefficient value. On the other hand, for $H_d = 0.90$, the resulting H_t exceeds the supported range, and the two extensions produce different values for k_{L}.

The third formulation is based on Vadapalli model (3.5), which defines the MTC as a function of both hematocrit and local oxygen saturation. In this case, since hematocrit is uniform along the vessel, the spatial variation in k_{V} is solely driven by the saturation. As illustrated in Section 3.7, this leads to a decreasing profile of the coefficient as a function of saturation.

The specific values of k_{cell} assigned in each simulation case are reported in Table 4.1, based on the models described in Chapter 3.

method	$k_{\mathbf{cell}}$	$\left[\mathrm{m}^3\ \mathrm{O}_2\ \mathrm{s}^{-1}\ \mathrm{mmHg}^{-1}\ \mathrm{m}^{-2}\right]$	
		$H_t = 0.10$	$H_t = 0.90$
Constant	k_{C}	$3.73 \cdot 10^{-8}$	$3.73 \cdot 10^{-8}$
Lücker-constant	$k_{\mathrm{L}}^{\mathrm{const}}$	$0.38 \cdot 10^{-8}$	$4.43 \cdot 10^{-8}$
Lücker-tangent	$k_{\mathrm{L}}^{\mathrm{tan}}$	$0.38 \cdot 10^{-8}$	$7.68 \cdot 10^{-8}$
Vadapalli	k_{V}	$k_{\mathrm{V}}(H_t = 0.08, S)$	$k_{\mathrm{V}}(H_t = 0.88, S)$

Table 4.1: MTC values used in the SV simulations for two hematocrit cases.

It is worth noting that in this simplified configuration with constant hematocrit, the different MTC formulations essentially reduce to using distinct values or functional dependencies for the mass transfer coefficient. For the constant and Lücker models, this results in a fixed k_{cell} value along the vessel, while for the Vadapalli model, k_{cell} varies solely as a function of saturation. This setup allows for a direct comparison of how the choice and behavior of k_{cell} influence oxygen transport predictions, isolated from the confounding effects of hematocrit variations that would occur in a full network simulation.

The simulation domain was discretized using a uniform structured mesh consisting of $100 \times 50 \times 100$ cubic elements along the x, y, and z directions, respectively. Given the physical domain size of $100\,\mu\mathrm{m} \times 50\,\mu\mathrm{m} \times 100\,\mu\mathrm{m}$, each element corresponds to a cube with side length $1\,\mu\mathrm{m}$. This resolution ensures accurate representation of steep concentration gradients near the vessel wall while keeping the computational cost manageable.

4.3 Realistic Microvascular Network

To test the different MTC formulations under realistic conditions, a realistic microvascular network was employed. This network was extracted from the somatosensory cortex of a mouse (shown in Figure 4.2), a highly vascularized brain region that is frequently investigated in neurovascular research.

The full dataset corresponds to a tissue volume of approximately $1\,\mathrm{mm}^3$, including 10 descending arterioles (DAs), 30 ascending venules (AVs), and approximately 20,000 capillaries. From this reference volume, a smaller network was selected, occupying a cubic volume of $0.064\,\mathrm{mm}^3$ (edge length 400 of μm), and used for the numerical simulations (see Figure 4.3). (For additional networks and corresponding simulations see Appendix D.)

The vascular geometries and the corresponding boundary conditions were originally

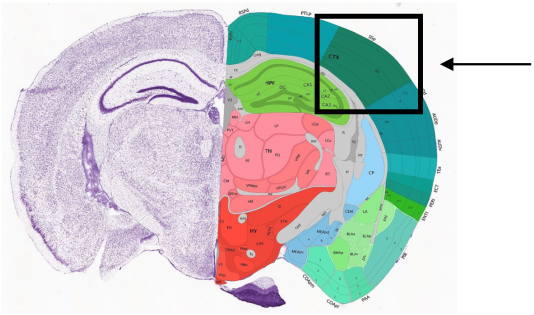

Figure 4.2: Coronal section of the mouse brain: on the left, a reference histological slice; on the right, schematic representation of major brain regions. The black square and arrow highlight the somatosensory cortex. (Image from [55])

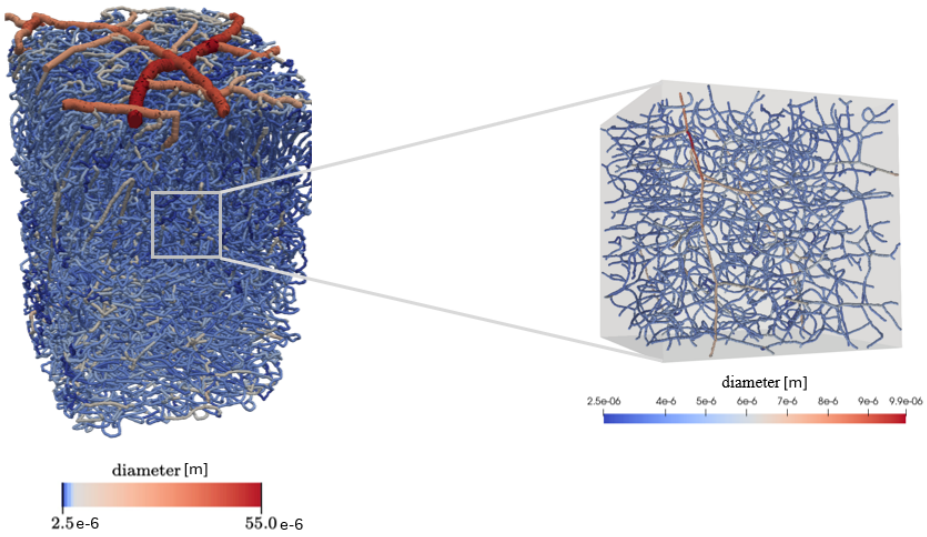

Figure 4.3: Three-dimensional representation of the cerebral microvascular network. The full reference volume ($\sim 1\,\mathrm{mm}^3$) is shown on the left, with vessels colored by diameter. Immage source: [56]. On the right, a cubic subnetwork of $0.064\,\mathrm{mm}^3$ used for the numerical simulations is highlighted, with vessels colored by diameter. (Image from [35])

obtained from *in-vivo* measurements using two-photon microscopy of the mouse somatosensory cortex. The three-dimensional vascular architecture was obtained from the measurements, whereas the boundary blood pressures were prescribed based on literature data (for more details see Schmid et al. [14]). The acquired network was then represented as a graph, with vertices corresponding to vessel junctions and edges representing individual vessel segments, each characterized by

attributes including diameter, length, and blood pressure boundary conditions. A small illustrative example of this graph structure is shown in Figure 4.4, providing an intuitive overview of nodes, edges, and their associated attributes.

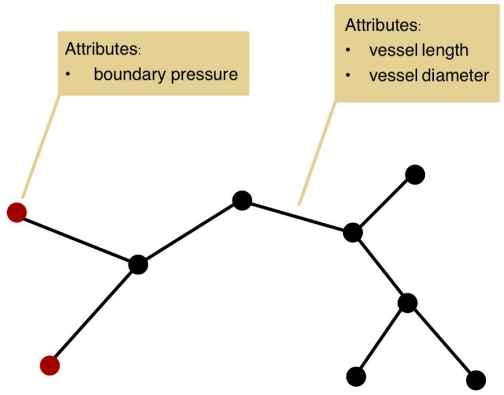

Figure 4.4: Illustrative example of the vascular graph structure. Vertices represent vessel junctions, with boundary nodes highlighted in red, while edges correspond to individual vessel segments. Boxes display the associated attributes for each vertex and edge, providing detailed information on the network elements.

This graph representation was used as input for *microBlooM*, an open-source simulation framework developed at the ARTORG Center for studying microvascular blood flow. *MicroBlooM* simulates blood flow in microvascular networks either assuming plasma-only flow or accounting for the effects of RBCs, as discussed theoretically in Section 1.1.3. The model is based on Poiseuille's law and the continuity eq.. Specifically, the iterative blood flow model consists of two main procedures: the first computes the flow in each vessel and the pressure at each node, while the second determines the hematocrit and apparent viscosity in each vessel. Hematocrit distribution at a bifurcation is calculated using the phase separation rule, applied through either an iterative or a waterfall approach. Further details are available on the GitHub repository [57] and in the publication by Schmid et al. [14].

From *microBlooM*, several key outputs were obtained: blood pressure at network vertices, flow rates, hematocrit distribution, and RBC velocities. These data were subsequently used as input for DuMu^{x} to simulate oxygen transport within both the vascular and tissue domains.

Although this approach provides a highly realistic physiological scenario, problems arise when there are vessels of the network characterized by extremely low hematocrit. These introduce numerical challenges when solving the vascular eqs. presented in Chapter 2. Specifically, when $H_d \sim 0.00$, the system of eqs. reduces

to:

$$\begin{cases} \frac{\partial}{\partial s}\left(A_v \rho_b u\right) = -\frac{\partial}{\partial s}\left(A_v \rho_b \frac{r_v^2}{8\mu_b}\frac{\partial p}{\partial s}\right) = 0 \\ \frac{\partial}{\partial s}\left(A_v u_{\text{pl}} \alpha_{\text{pl}} P_{\text{pl}}\right) - A_v j_{\text{RBC-pl}} = \hat{q}_C \\ A_v j_{\text{RBC-pl}} = 0 \\ \frac{\partial}{\partial s}(A_v u_{\text{RBC}} S) = 0 \end{cases} \tag{4.2}$$

Under these conditions, the system may become numerically ill-conditioned. In particular, in vessels where $H_d \sim 0.00$, RBCs are absent; therefore the exchange flux $j_{\text{RBC-pl}}$ should vanish, as no oxygen exchange between RBCs and plasma is physically possible. As a result, the value of P_{RBC}, although still formally present in the model eqs., does not influence any physiological exchange process and lacks biological interpretability. In these vessels, the focus was therefore shifted away from the absolute value of P_{RBC}, which can become arbitrarily large due to the weak coupling. Instead, attention was placed on the exchange term $j_{\text{RBC-pl}}$, which remains physically meaningful and is treated carefully in the numerical implementation. To ensure numerical stability, it was necessary to assign to $j_{\text{RBC-pl}}$ a small non-zero value, on the order of 10^{-10}, sufficient to regularize the system while avoiding biologically unrealistic oxygen exchange. From a numerical standpoint, assigning a strictly zero oxygen exchange term would result in a singular system matrix, making the simulation unsolvable.

To prevent the emergence of unrealistic values, the partial pressures of oxygen in both RBCs and plasma are constrained within a biologically plausible range:

$$P_{\text{RBC}},\ P_{\text{pl}} \in [0, 200]\,\text{mmHg}.$$

The lower bound reflects the physiological non-negativity of partial pressures, while the upper bound was chosen to limit excessive oxygen exchange in plasma vessels, without excluding physiologically relevant values in the results. Indeed, the *in-vivo* results obtained by Lyons et al. [58] confirm that the range of oxygen partial pressure proposed here is consistent with *in-vivo* values.

It is important to emphasize that these bounds were not applied as a post-processing truncation of computed values (i.e., replacing values exceeding 200 mmHg with the bound). Instead, they were incorporated directly into the numerical formulation as box constraints, consistent with the chopped Newton approach introduced in Section 4.1, guiding the Newton solver to search for admissible solutions within the specified range. This approach preserves the integrity of the computed solution and avoids artifacts that would arise from a posteriori value clipping. A deeper analysis on the importance of this limitation can be found in Appendix C.

Consequently, post-processing required filtering non-physical data points arising from these edge cases.

With the numerical issues fixed, attention was directed to the comparison of different models for the MTC.

In the first case, the model employs a constant value for the cellular MTC k_{C}; this parameter was assigned based on Lücker formulation described in Section 3.2.1. Specifically, k_{C} was computed using the expression obtained by Lücker, by converting a representative discharge hematocrit H_d into the corresponding tube hematocrit H_t using eq. (1.2). For this conversion, a reference vessel diameter of $D = 4\,\mu$m was used, which is representative of the vessel scale. The discharge hematocrit employed in the calculation corresponds to the mean value extracted from the hematocrit distributions.

In the context of Lücker approach, as previously discussed, two options are available. However, in this case, only the tangent extension is considered, so $k_{\mathrm{L}} = k_{\mathrm{L}}^{\tan}$ (as defined in (3.3)). This choice was driven by the need to maintain smoothness in the functional dependence of k_{cell} with respect to H_t, and to avoid artificial discontinuities in the derivative. The constant extension, while simpler, introduces a flat region that may distort the physical behavior of the model and suppress sensitivity to local hematocrit variations in regions where $H_t > 0.50$. On the contrary, the tangent extension ensures continuity and a physically reasonable trend, reflecting the assumption that oxygen transfer may continue to increase slightly at high hematocrit values. (Additional results supporting this choice are provided in Appendix A.2.)

For Vadapalli formulation, the eq. discussed in (3.4) is used.

The simulation domain was discretized using a uniform structured mesh consisting of $200 \times 200 \times 200$ cubic elements along the x, y, and z directions, respectively. Given the physical domain size of $400\,\mu\mathrm{m} \times 400\,\mu\mathrm{m} \times 400\,\mu\mathrm{m}$, each element corresponds to a cube with side length $2\,\mu$m. The chosen resolution balances accuracy in capturing steep concentration gradients near the vessel wall with computational efficiency.

4.4 Model parameters

The parameters used in the oxygen transport simulations can be grouped into two main categories. The first category includes the parameters that define the oxygen transport model introduced in Chapter 2. These values are considered constant and are shared across all simulations, independently of the vascular geometry under investigation. Table 4.2 summarizes these global model parameters.

Parameter	**Description**	**Value**	**Units**	**Reference**
$\alpha_{\mathbf{RBC}}$	O_2 solubility in RBCs	$3.38 \cdot 10^{-5}$	$m^3\,O_2\,mmHg^{-1}\,m^{-3}$	[59]
$\alpha_{\mathbf{pl}}$	O_2 solubility in plasma	$2.82 \cdot 10^{-5}$	$m^3\,O_2\,mmHg^{-1}\,m^{-3}$	[60]
$\alpha_{\mathbf{T}}$	O_2 solubility in the tissue	$3.89 \cdot 10^{-5}$	$m^3\,O_2\,mmHg^{-1}\,m^{-3}$	[61]
$D_{\mathbf{T}}$	O_2 diffusivity in the tissue	$2.41 \cdot 10^{-9}$	$m^2 s^{-1}$	[62]
$D_{\mathbf{W}}$	O_2 diffusivity in the capillary wall	$8.73 \cdot 10^{-10}$	$m^2 s^{-1}$	[63]
M_0	Oxygen consumption	$4 \cdot 10^{-4}$	$m^3\,O_2\,m^{-3}\,s^{-1}$	[1]
n	Hill exponent	2.65	-	[41]
K	Dissociation rate constant	44	s^{-1}	[41]
C_0	Oxygen binding capacity	0.52	$m^3\,O_2\,m^{-3}$	[1]
$P_{\mathbf{RBC,50}}$	P_{RBC} at hemoglobin half saturation	47.9	mmHg	[1]
$P_{\mathbf{T,crit}}$	Critical P_{T}	1.0	mmHg	[28]
σ	Oxygen permeability	0	-	model assumption
ρ_b	Blood density	1050	$kg\,m^{-3}$	[57]
μ_b	Blood dynamic viscosity	0.0012	mmHg s	[57]

Table 4.2: Parameters used in the oxygen transport model (common to all simulations).

The second category includes parameters that are specific to each case study, such as boundary conditions. These parameters differ between the SV configuration and the MVN. A detailed list of case-specific parameters is provided in Table 4.3.

Parameter	**Description**	**SV**		**MVN**		**Units**
		Value	**Reference**	**Value**	**Reference**	
$P_{\mathbf{pl,\ in}}$	P_{pl} inflow	90	model parameter	25	[1]	mmHg
$P_{\mathbf{RBC\text{-}DA,\ in}}$	P_{RBC} inflow for descending arteries	-	-	75	based on [64][65][58] [66][67]	mmHg
$P_{\mathbf{RBC\text{-}AV,\ in}}$	P_{RBC} inflow for ascending veins	-	-	40	based on [64][65][58] [66][67]	mmHg
$P_{\mathbf{RBC\text{-}CP,\ in}}$	P_{RBC} inflow for capillaries	40	model parameter	$f(H_d)$	[58]	mmHg
$S_{\mathbf{in}}$	S inflow	0.38	[a]	-	[a]	-

[a] Values are set in equilibrium with $P_{\mathrm{RBC\text{-}\cdot,in}}$ via (2.7).

Table 4.3: Parameters used for the SV and MVN configurations.

This choice allows one to isolate and analyze the mechanisms of oxygen transport without the additional variability introduced by flow redistribution.

Another important modeling aspect concerns the assignment of the inflow $P_{\mathrm{RBC,in}}$ for the capillaries, $P_{\mathrm{RBC\text{-}CP,\ in}}$. As previously mentioned in Section 2.3.1, this value is not fixed a priori but determined as a function of the discharge hematocrit, H_d. To this end, a piecewise-defined function $f(H_d)$ was employed. The function $f(H_d)$ was derived by Stievano, based on data extracted from the work of Lyons et al. [58]. This approach ensures that the model captures the variability of oxygen availability within RBCs as a function of hematocrit, providing a more physiologically accurate description of microvascular oxygen transport.

Chapter 5

Results

In this chapter, the results obtained from the numerical simulations performed with DuMu^{x} are presented and discussed. The analysis focuses on both simplified and realistic vascular configurations to investigate oxygen transport mechanisms under different conditions.

First, the results for a single vessel (SV) are shown, comparing the pressure fields in plasma (P_{pl}) and RBCs (P_{RBC}) for two different hematocrit values, following the setup described in 4.2.

Subsequently, the focus shifts to the realistic MVN, where the global oxygen distribution in the tissue is analyzed and the different modeling approaches are compared. In this context, representative paths are selected to investigate the local behavior of P_{pl} and P_{RBC} along specific flow trajectories. Finally, the volume and spatial localization of hypoxic regions within the realistic model are examined.

The simulation outputs generated by DuMu^{x} were post-processed and analyzed using Python, which provided an efficient framework for data visualization and quantitative comparison between the different simulation configurations.

5.1 Single Vessel

The SV simulations were conducted to assess the model's ability to reproduce oxygen transport dynamics in an isolated geometry, under controlled flow and boundary conditions.

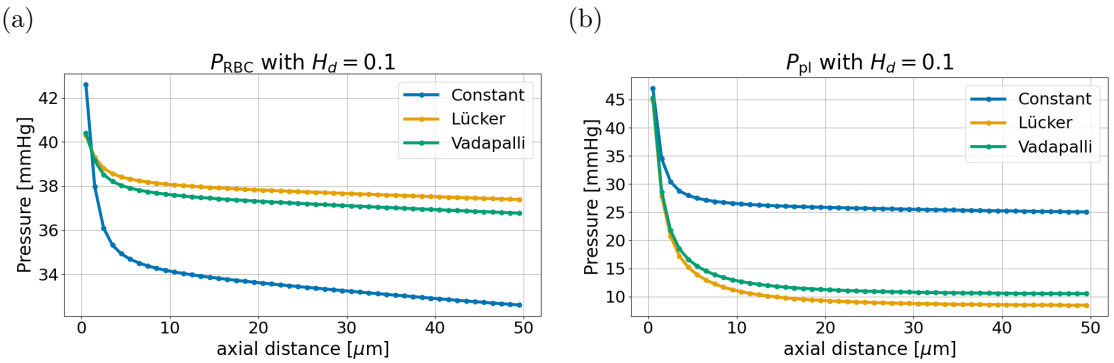

Figure 5.1: Oxygen partial pressure variation along a single vessel with $H_d = 0.10$, comparing different methods. Variation of P_{RBC} (a) and P_{pl} (b) along the vessel.

The two plots in Figure 5.1 show the spatial profile of oxygen partial pressure in plasma (P_{pl}) and RBCs (P_{RBC}) as a function of the axial distance along the vessel. Each plot compares the results obtained using the four different formulations of the MTCs as described in Section 4.2: Constant (blue), Lücker (yellow), and Vadapalli (green). Since the values of $k_{\mathrm{L}}^{\mathrm{const}}$ and $k_{\mathrm{L}}^{\mathrm{tan}}$ are numerically identical for the given value of H_d (Table 4.1), their corresponding curves are perfectly overlapping. For this reason, they are represented by a single yellow curve. Specifically, the left panel of Figure 5.1 presents the variation of P_{RBC} along the vessel. For Vadapalli, Lücker-constant, and Lücker-tangent approaches, the decrease in P_{RBC} is relatively modest, with values dropping from approximately 40 mmHg at the inlet of the vessel to around 37 mmHg at the outlet. This limited variation suggests that, under the low hematocrit conditions considered here, the RBC phase undergoes limited oxygen depletion along the flow path. In contrast, the constant k_{cell} predicts a steeper decrease, with P_{RBC} decreasing by almost 10 mmHg over the same distance. Regarding the plasma phase, the right panel shows that P_{pl} decreases monotonically with increasing axial distance. However, the choice of MTC has a more pronounced influence on plasma than on RBCs. In particular, the constant k_{cell} yields higher values of P_{pl}, with the maximum difference relative to the other approaches reaching about 20 mmHg. This corresponds to a slower decrease of oxygen from the plasma phase when using the constant value for the MTC k_{C}, in contrast to the more pronounced declines observed with Lücker and Vadapalli methods.

A common feature of all models is the mirrored behaviour of the two phases: segments along the vessel where P_{pl} exhibits a steeper drop correspond to a milder decrease in P_{RBC}, and vice versa.

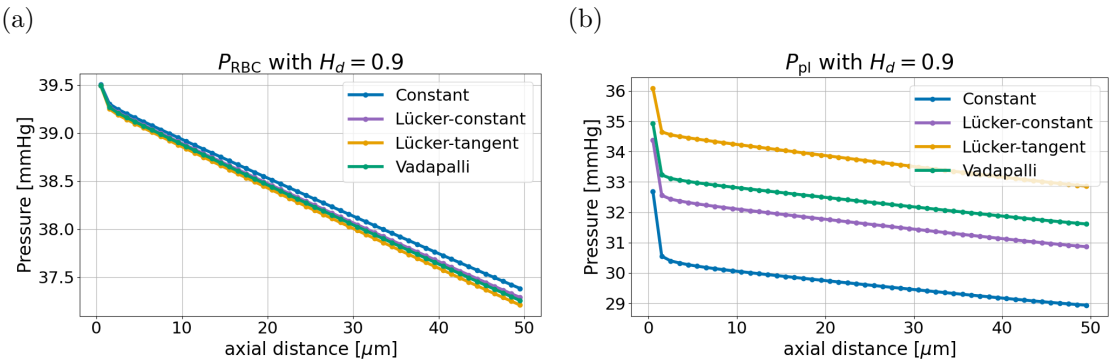

Figure 5.2: Oxygen partial pressure variation along a single vessel with $H_d = 0.90$, comparing different methods. Variation of P_{RBC} (a) and P_{pl} (b) along the vessel.

Figure 5.2 shows the results obtained for $H_d = 0.90$. Unlike the previous case, we now find two distinct curves for the Lücker formulation: a purple one for the constant extension and a yellow one for the tangent extension. This is because, for this specific hematocrit, the values of $k_{\mathrm{L}}^{\mathrm{const}}$ and $k_{\mathrm{L}}^{\mathrm{tan}}$ are distinct, as evident from Table 4.1.

As in the previous case, both plots show a decreasing trend for P_{RBC} and P_{pl}. However, the decreases are generally less pronounced. Specifically, P_{RBC} drops from about 39.5 mmHg at the inlet of the vessel to roughly 37 mmHg at the outlet, while the largest decrease in P_{pl} is approximately 4 mmHg observed for the constant k_{cell}.

As in the $H_d = 0.10$ case, a mirrored behaviour between the two phases is observed: P_{pl} decreases more steeply correspond to a milder decrease in P_{RBC}, and vice versa.

A notable difference from the low hematocrit case is that, for $H_d = 0.90$, the choice of MTC formulation has a smaller impact on the results. In the left panel, the curves for the different methods are almost indistinguishable, whereas in the right panel, they exhibit the same trend but are offset by only a few mmHg.

A similar mirrored trend can also be observed when comparing results for the same variable between low and high hematocrit cases. However, this pattern is not consistently preserved for Lücker-constant formulation when $H_d > 0.50$, indicating a deviation from the expected symmetry in high hematocrit regimes.

5.1.1 Discussions

The SV simulations provide key insights into the interplay between hematocrit, oxygen transport dynamics, and MTC formulation.

At low hematocrit ($H_d = 0.10$), the most relevant differences among the models arise from the definition of the MTC. Lücker and Vadapalli formulations show consistent and nearly overlapping results, indicating that they describe the oxygen

exchange process with a comparable efficiency. In contrast, the constant k_{cell} deviates significantly, yielding higher values of P_{pl} and lower values of P_{RBC}, as shown in Figure 5.1. This behaviour can be traced back to the assumption underlying the constant MTC, which was calibrated for an average hematocrit representative of whole blood (see Chapter 4). In the current low hematocrit setting, this results in a constant MTC coefficient higher than that obtained with the other approaches, implying a greater exchange efficiency than physiologically expected. Consequently, the redistribution of oxygen between plasma and RBCs predicted by the constant k_{cell} is biased: plasma retains higher oxygen levels, while RBCs exhibit a stronger depletion. In other words, the discrepancy is not merely numerical but reflects a structural inconsistency between the assumed transfer efficiency and the physiological conditions being modelled.

At high hematocrit ($H_d = 0.90$), the discrepancies between the different MTC formulations become minimal (see Figure 5.2). This consistency can be attributed to the biological mechanisms dominating oxygen transport in this regime. When RBCs are abundant, the large storage capacity of hemoglobin provides a continuous reservoir of oxygen that buffers plasma fluctuations. As a result, oxygen levels in plasma are steadily replenished by hemoglobin desaturation, making the overall dynamics less sensitive to the precise definition of the transfer coefficient. In practical terms, the efficiency of the exchange process is not determined by the MTC formulation but by the intrinsic ability of hemoglobin to release oxygen in response to local gradients. Hence, under high hematocrit conditions, all models converge towards nearly identical trends, with only minor deviations in the plasma phase.

The mirrored trends observed between the plasma and RBC phases highlight the coupled nature of the two compartments: when plasma exhibits a steeper decline in oxygen partial pressure, RBCs display a correspondingly milder decrease, and vice versa. This behaviour reflects the bidirectional exchange mediated by the MTC, where the phase with the larger concentration gradient tends to dominate the dynamics.

5.2 Realistic Microvascular Network

Simulations in a microvascular network were performed to evaluate the model under physiologically relevant geometries and flow distributions.

To characterize the selected network, the hematocrit distribution was first computed using the *microBlooM* framework, with the results shown in Figure 5.3. The overall mean discharge hematocrit is $H_d = 0.37$. This value corresponds to the representative hematocrit employed in Chapter 4 for the computation of the constant MTC $k_{\text{C}} = 2.67 \cdot 10^{-8}\,\text{m}^3\text{O}_2\text{s}^{-1}\text{mmHg}^{-1}\text{m}^{-2}$ based on Lücker formulation

(see Figure 3.5).

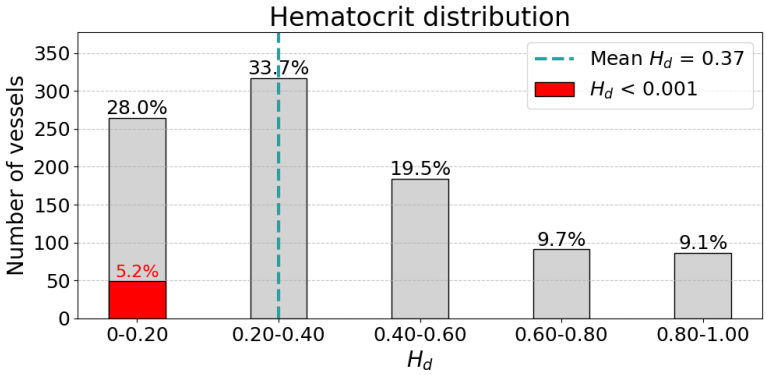

Figure 5.3: Mean discharge hematocrit (H_d) distribution across vessels. The first bin (0–0.20) is partially highlighted in red to indicate vessels with $H_d < 0.001$. Percentages refer to the total vessel count, while the dashed line marks the overall mean H_d.

As can be observed in Figure 5.3, 5.2% of the vessels exhibit a very low hematocrit value. As discussed in Chapter 4, such vessels lead to numerical ill-conditioning; therefore, for the analyses reported in this chapter, they were excluded from the analysis of the results.

5.2.1 3D visualization and global distributions

The first stage of the analysis is intended to emphasize the differences between the three methods under investigation. Since the ultimate objective is to determine how much oxygen effectively reaches the brain tissue, the discussion is focused on the resulting oxygen partial pressure of the tissue (P_{T}), which directly reflects oxygen availability. For clarity, the comparison is presented in a pairwise manner: first between constant and Lücker k_{cell}, then between constant and Vadapalli k_{cell}, and finally between Lücker and Vadapalli k_{cell}.

Constant-Lücker

When comparing these two approaches, the corresponding MTCs are shown in Figure 5.4. The yellow curve represents the MTC adopted in Lücker method, as defined by eq. (3.3), while the blue line corresponds to the constant value k_{C}. By construction, the two functions intersect at $H_t = 0.37$. The largest deviations between the two MTCs occur at high hematocrit values.

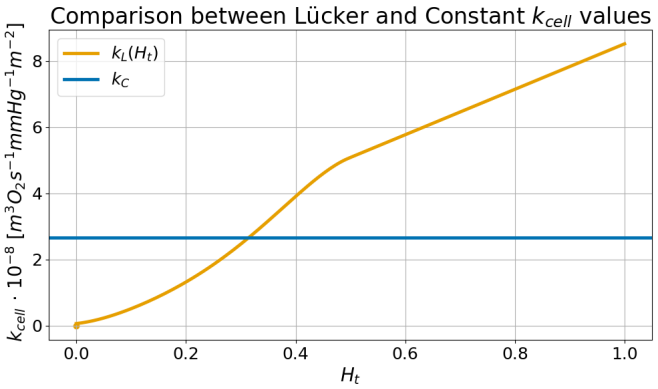

Figure 5.4: Comparison between the MTC functions used in Lücker and constant k_{cell}.

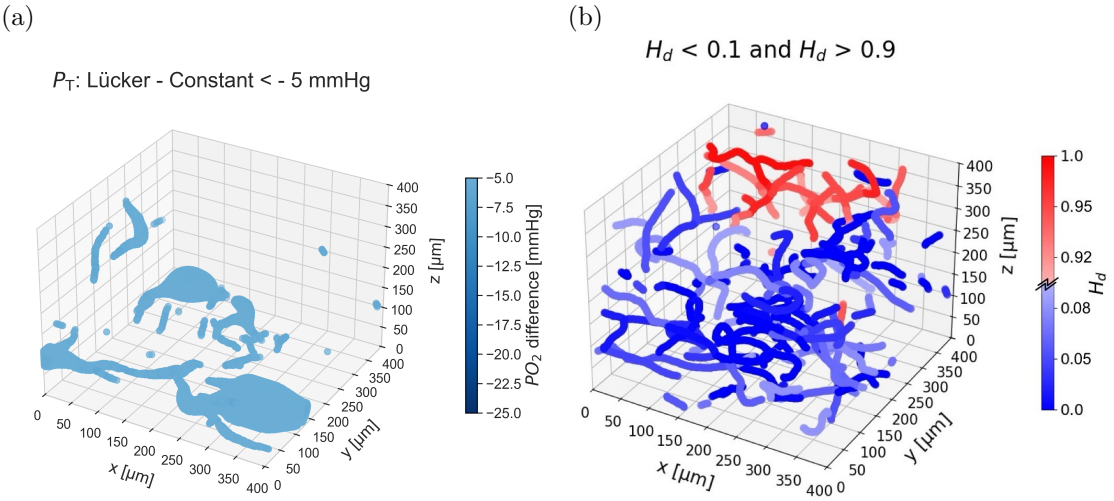

Figure 5.5: (a) Spatial distribution of the difference in tissue oxygen partial pressure (P_{T}) between constant and Lücker k_{cell}. Only regions where this difference exceeds -5 mmHg are shown. (b) Distribution of discharge hematocrit (H_d) within the vascular network, independent of the chosen method. Only vessels with very low ($H_d < 0.10$) or very high ($H_d > 0.90$) hematocrit values are displayed.

The spatial distribution of differences in tissue oxygen partial pressure (P_{T}) between the two methods is shown in Figure 5.5(a). Regions where the constant k_{cell} model predicts higher P_{T} values than the Lücker method by more than 5 mmHg are shaded in blue.

The direct 3D visualization immediately reveals that these discrepancies are predominantly localized in regions characterized by very low discharge hematocrit

values, as shown in Figure 5.5(b). Here, blue shades denote $H_d < 0.10$ and red shades denote $H_d > 0.90$. By focusing exclusively on these hematocrit extremes while masking intermediate values, we highlight precisely where the two MTC functions differ most significantly (see Figure 5.4), and consequently where the largest differences in P_{T} are expected to occur.

To complement this spatial analysis and better quantify the magnitude of these differences, contour plots at selected z-slices ($z \approx 50$ and $z \approx 100$) are presented alongside the 3D plots. These slices were chosen based on the 3D visualization, which shows the most pronounced differences occurring near the domain base.

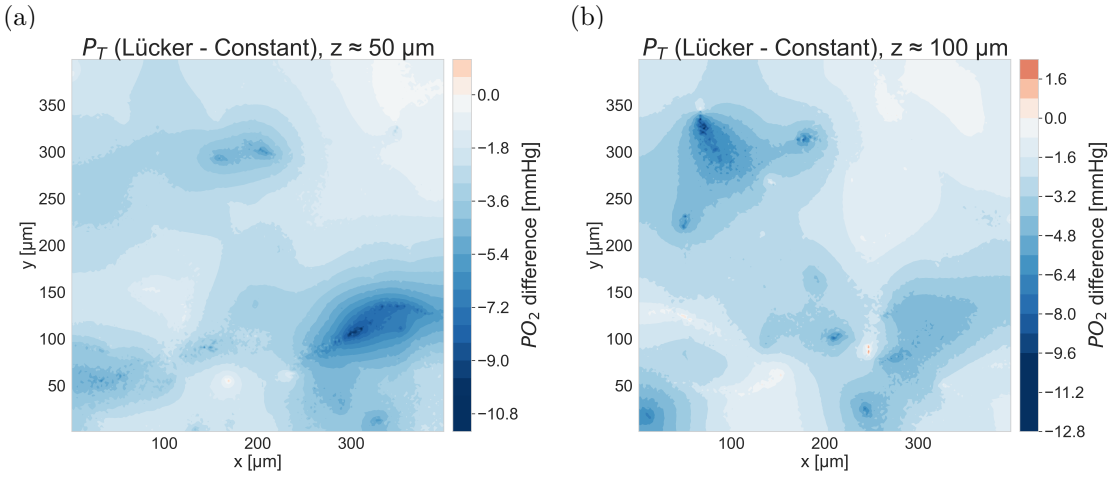

Figure 5.6: Contour plots of differences in tissue oxygen partial pressure at two cross-sections: (a) $z \approx 50$ and (b) $z \approx 100$. These slices highlight the internal distribution of P_T and emphasize regions where the differences between results using k_{C} and k_{L} are most pronounced.

These contour plots confirm the predominantly negative differences observed in the 3D visualization, while revealing that the internal tissue regions are characterized by much more severe local peaks than apparent from the surface rendering.

The two representations provide complementary information: while the 3D plots allow to identify the location and spatial context of regions affected by the MTC choice in relation to hematocrit distribution, the contour plots reveal that within these regions, the local differences in P_{T} can be much larger than the uniform blue shading might suggest like shown in Figure 5.5 (a).

Constant-Vadapalli

When comparing constant and Vadapalli approaches, the corresponding MTCs are shown in Figure 5.7.

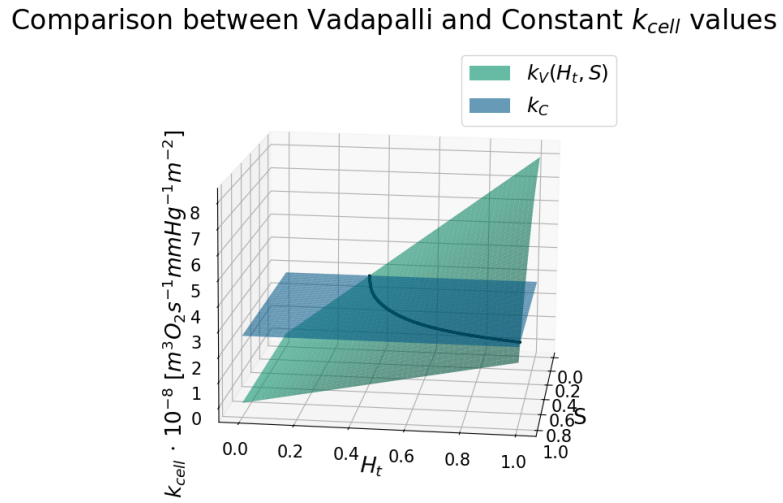

Figure 5.7: Comparison between the MTC functions used in Vadapalli and constant k_{cell}. The intersection between the two functions is highlighted with a darker line.

As previously discussed in Chapter 3, k_{V} depends not only on hematocrit but also on the local oxygen saturation, introducing an additional spatial variability compared to the other methods. For very low hematocrit ($H_t \sim 0.00$), the difference between the two functions is nearly constant across all S values, where k_{V} is significantly lower than k_{C}. For a high value of the hematocrit, Vadapalli model predicts a strong dependence of k_{V} on oxygen saturation. At high S, k_{V} is slightly below the constant value k_{C}, but as S decreases, k_{V} rises sharply, exceeding k_{C} by a wide margin when saturation approaches its minimum.

The spatial distribution of P_{T} differences between the two methods is reported in Figure 5.8 (a). Blue-shaded regions correspond to locations where the constant k_{cell} predicts P_{T} values higher (more than 5 mmHg) than Vadapalli method. Compared to Constant–Lücker case, these regions are generally larger, and an additional cluster appears in the upper part of the domain.

Since k_{V} is a function of both hematocrit and oxygen saturation, Figure 5.8 (b) displays vessels with very high saturation values. Here, only Vadapalli results are shown, as the qualitative behavior relevant for this type of analysis was very similar to Lücker. In this scenario, it is reasonable to focus on high-saturation values. Although the model differences in k_{V} are more pronounced at low saturation, k_{V}

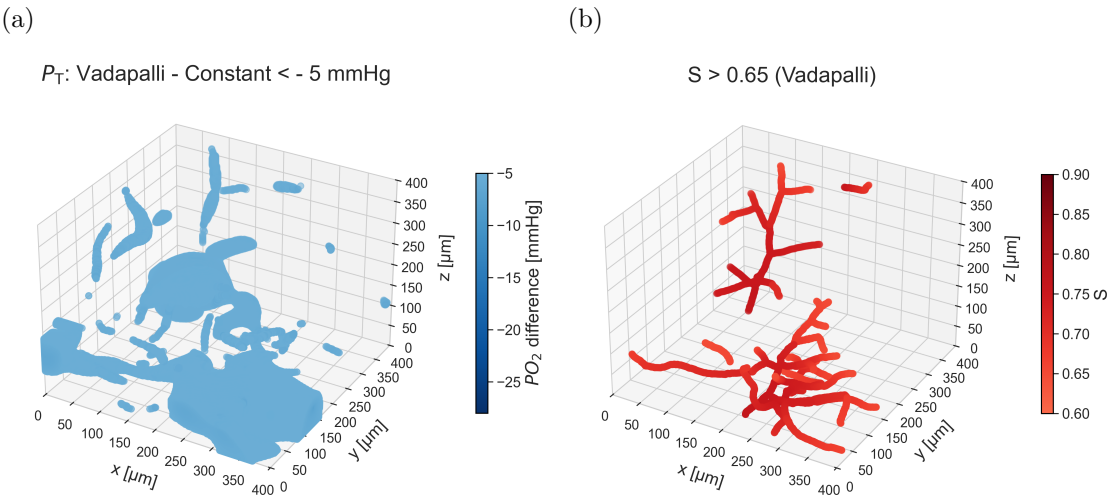

Figure 5.8: (a) Spatial distribution of the difference in tissue oxygen partial pressure (P_T) between constant and Vadapalli k_{cell}. Only regions in the tissue where the difference exceeds -5 mmHg are shown. (b) Distribution of oxygen saturation along the vascular network for Vadapalli method. Only vessels with a saturation greater than 0.65 are displayed.

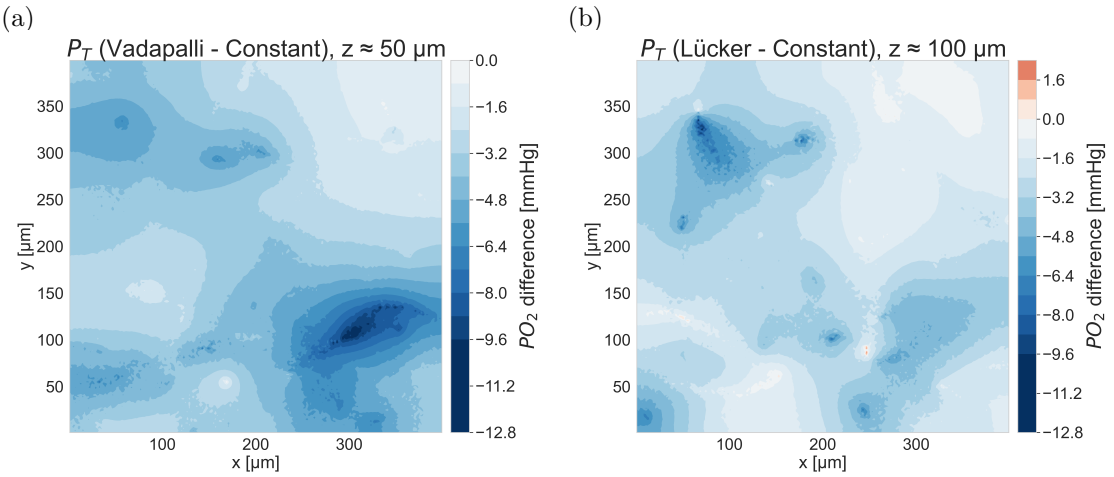

Figure 5.9: Contour plots of differences in tissue oxygen partial pressure at two cross-sections: (a) $z \approx 50$ and (b) $z \approx 100$. These slices highlight the internal distribution of P_T and emphasize regions where the differences between results using k_C and k_V are most pronounced.

becomes smaller when saturation is high (see Figure 5.7). As discussed in the SV analysis, lower k_{cell} values tend to have a stronger influence on the resulting

oxygen transport. The comparison of Figures 5.8 (a) and 5.8 (b) indicates that the newly observed regions of discrepancy (absent in Constant–Lücker comparison) correspond to areas where hematocrit and saturation are both high. This behavior highlights the role of saturation in k_{V}, influencing tissue oxygen availability.

However, the contour plots in Figure 5.9 reveal that the actual magnitude of these differences is substantially larger than what the 3D visualization suggests. The surface rendering primarily captures superficial patterns, while the cross-sectional analysis exposes localized internal regions where P_{T} deficits reach much more significant values. These deep tissue hotspots were completely masked in the 3D overview, demonstrating how internal oxygen distribution patterns can differ substantially from what surface observations suggest.

Lücker-Vadapalli

When comparing Lücker and Vadapalli approaches, the key distinction lies in the additional dependence of k_{V} on oxygen saturation. While Lücker formulation links mass transfer exclusively to hematocrit, Vadapalli method introduces a modulation by S. Figure 5.10 shows this distinction by comparing the MTCs predicted by the two models, $k_{\mathrm{L}}(H_t)$ and $k_{\mathrm{V}}(H_t, S)$. The yellow surface represents k_{L}, which varies only with hematocrit and therefore remains constant across S. In contrast, the green surface corresponds to k_{V}, which exhibits dependence on both H_t and S. At low hematocrit values, the two models predict similar magnitudes of k_{cell} across the full saturation range. At higher hematocrit, however, Vadapalli formulation shows a marked dependence on the oxygen saturation: at low S, k_{V} remains close to k_{L}, whereas at high S it decreases sharply, diverging from Lücker function. Thus, the key distinction between the two formulations is the saturation, which becomes more evident at elevated hematocrit.

Figure 5.11 (a) shows the spatial distribution of P_{T} differences between the two methods. In this case, a threshold of 3 mmHg was adopted, since the discrepancies between Lücker and Vadapalli are generally smaller in magnitude. Red-shaded regions correspond to regions where Lücker method predicts P_{T} values higher than those obtained with Vadapalli method.

By comparing Figure 5.11 (a) with Figure 5.11 (b) and Figure 5.5 (b) (which display the hematocrit distribution in the network), it can be observed that the regions with the largest differences between the two methods correspond to areas where hematocrit is not null and oxygen saturation is high.

The contour plots in Figure 5.12 confirm these observations, revealing that the differences between the two methods are indeed less pronounced compared to previous cases. The maximum differences reach only about 5 mmHg, and the predominantly red color scheme consistently shows Lücker predicting higher P_{T} values than Vadapalli throughout the tissue volume.

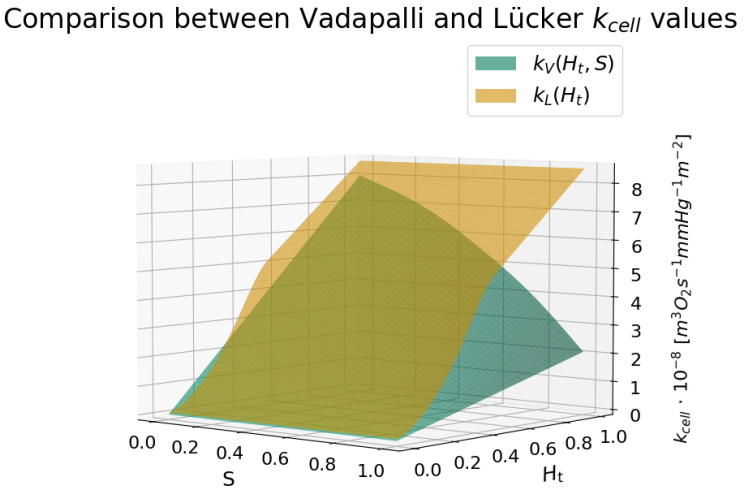

Figure 5.10: Comparison between the MTC functions used in Vadapalli and Lücker methods.

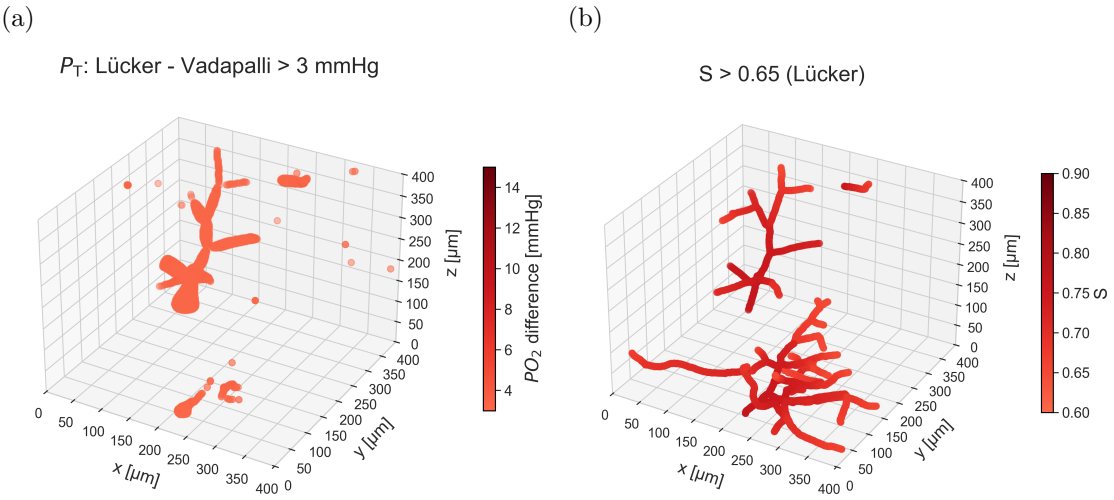

Figure 5.11: (a) Spatial distribution of the difference in tissue oxygen partial pressure (P_T) between Lücker and Vadapalli methods. Only regions in the tissue where the difference exceeds 3 mmHg are shown. (b) Distribution of oxygen saturation along the vascular network for Lücker method. Only vessels with a saturation greater than 0.65 are displayed.

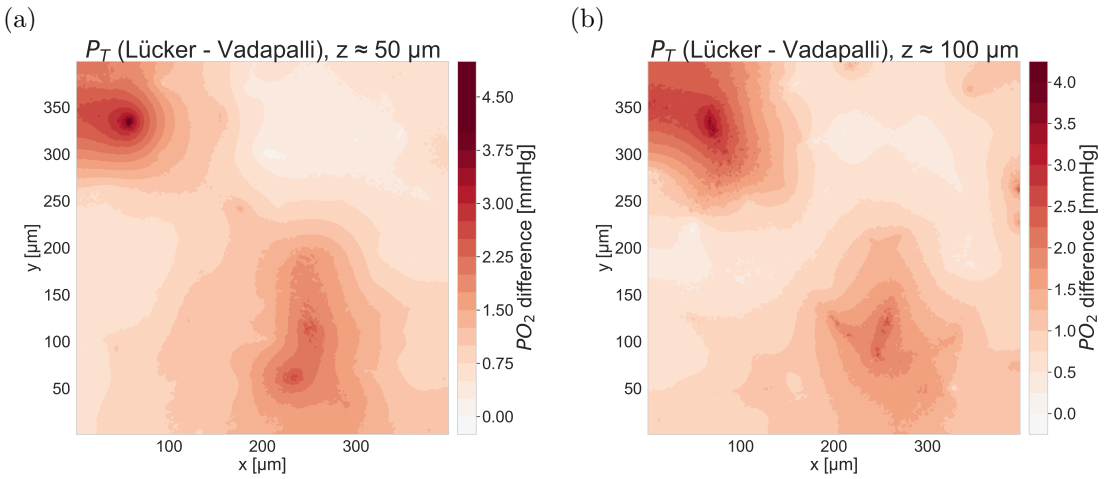

Figure 5.12: Contour plots of differences in tissue oxygen partial pressure at two cross-sections: (a) $z \approx 50$ and (b) $z \approx 100$. These slices confirm the reduced magnitude of differences between k_{L} and k_{V} approaches compared to other method pairs.

A complementary analysis can be carried out by examining the global distribution through the frequency histograms in Figure 5.13. These reveal that the overall oxygenation profiles remain broadly comparable, with no major shifts across the range of P_{T}. All three curves exhibit a pronounced peak in the range of 30-40 mmHg and follow a bell-shaped trend, gradually decreasing toward the extremes. Then,

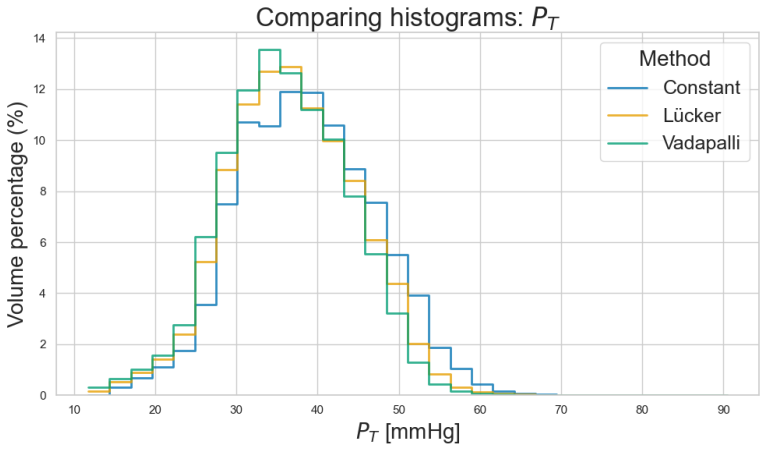

Figure 5.13: Frequency distribution of P_{T} for the different methods are compared

the analysis is extended using boxplots, which provide a clearer view of how the distributions diverge. The distribution of P_{T} differences among the three model

comparisons is illustrated in Figure 5.14. When comparing Lücker and constant k_{cell}, the differences are predominantly negative, with a median shift below zero. This observation is consistent with what was previously noted from the analysis of Figure 5.5 (a). Moreover, this comparison exhibits a wide variability, as highlighted by the large interquartile range and the presence of numerous outliers, some of which reach values below −20 mmHg. A similar trend is observed in Vadapalli–Constant comparison, where the median difference is again negative. In this case, the variability is even larger than in Lücker–Constant comparison, and extreme outliers reach approximately −25 mmHg. In contrast, the comparison between Lücker and Vadapalli models shows a distribution with a median close to zero, with a narrow spread and only a limited number of mild outliers. This suggests that, while both models deviate from constant reference, Lücker and Vadapalli gave results that are more consistent with each other.

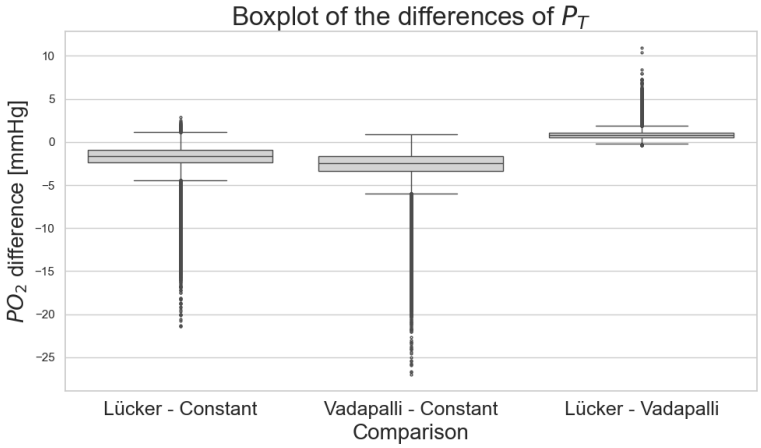

Figure 5.14: Boxplots of the differences in P_{T} for the three model comparisons.

Although the frequency distributions did not indicate substantial differences between the models, the boxplots provide a complementary analysis, revealing systematic discrepancies in the results. These observations suggest that, even if global distributions appear broadly comparable, local variations may still play a significant role in shaping the overall behavior of the models. To explore these aspects in greater detail, the analysis is extended to specific paths extracted from the network.

5.2.2 Analysis along representative paths

Three representative paths are considered, each characterized by a different hematocrit distribution: the first with a variable hematocrit, the second with a low hematocrit, and the third with a high hematocrit. These paths, which follow the blood flow, are shown in Figure 5.15 and allow for a more localized comparison between the different modeling approaches.

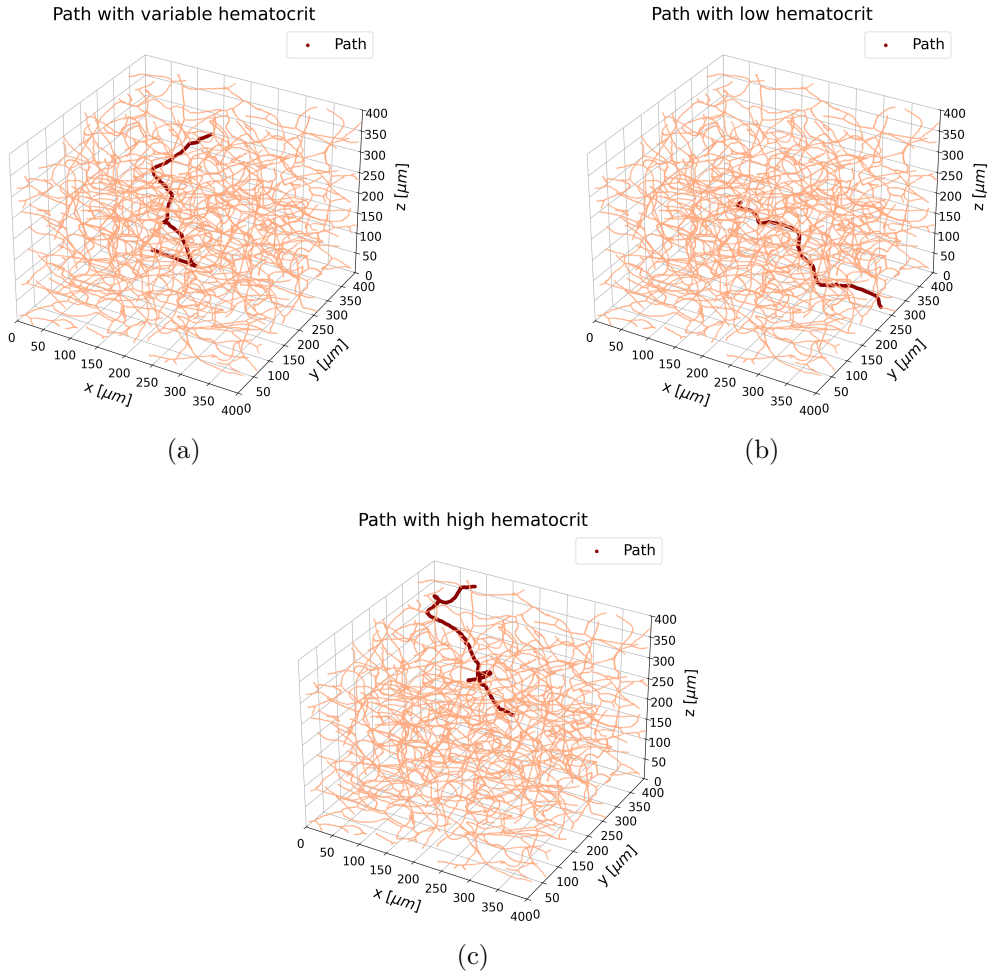

Figure 5.15: Three-dimensional view of the selected path, extracted from the vascular network with variable hematocrit (a), low hematocrit (b) and high hematocrit (c).

In the previous section, the analysis focused on P_T, as it provides a direct measure of oxygen availability at the tissue level. However, to investigate the impact of local hematocrit variations along specific vascular paths, it is more

informative to examine the intravascular pressures P_{RBC} and P_{pl}. Indeed, these quantities directly reflect how the different MTCs influence oxygen transport from RBCs to plasma and, ultimately, to the surrounding tissue.

The first selected path, shown in Figure 5.15 (a), is characterized by a variable hematocrit. As illustrated in Figure 5.16 (a), the first 150 segments of the path exhibit a relatively low average hematocrit. Beyond this point, the values remain systematically above the mean hematocrit of the entire network ($H_d = 0.37$), with an overall average along the path of $H_d = 0.33$. This pattern directly affects the MTC values obtained with the different approaches. As can be seen in Figure 5.16 (b), in the initial part of the domain k_{L} and k_{V} are lower than k_{C}. As the hematocrit approaches $H_d = 0.37$ (the reference value used to compute k_{C}) all three coefficients converge to similar values. In the final part of the path, where the hematocrit is higher than the network average, both k_{L} and k_{V} become larger than k_{C}.

(a) (b)

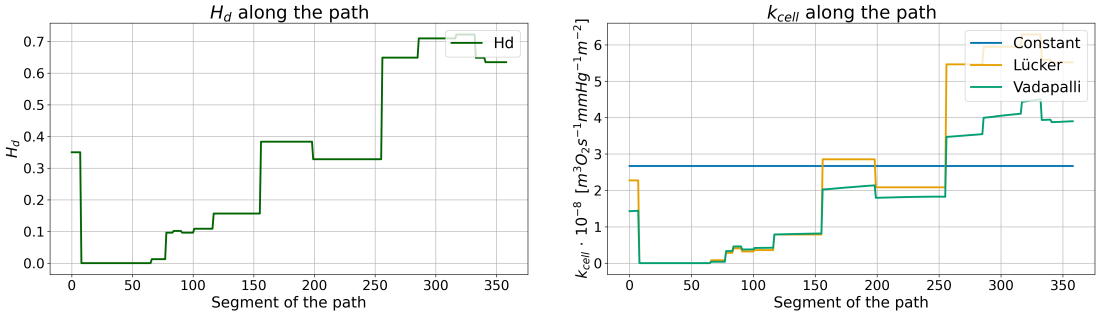

Figure 5.16: (a) Hematocrit profile along the path. (b) MTCs k_{C}, k_{L} and k_{V} computed along the path.

Figure 5.17 shows the variations of P_{pl} and P_{RBC} along the path. Before step 150, clear differences between the methods are visible: in particular, the blue curve corresponding to the constant k_{cell} deviates the most from the other two. In the second part of the path, however, all methods display a very similar behavior.

The second path, shown in Figure 5.15 (b), is characterized by a consistently low hematocrit along its entire length. As illustrated in Figure 5.18 (a), the hematocrit remains below $H_d = 0.20$ throughout the path, the mean value is $H_d = 0.09$. Figure 5.18 (b) shows that both k_{L} and k_{V} are generally lower than k_{C}, reflecting the influence of the low hematocrit on the MTC value.

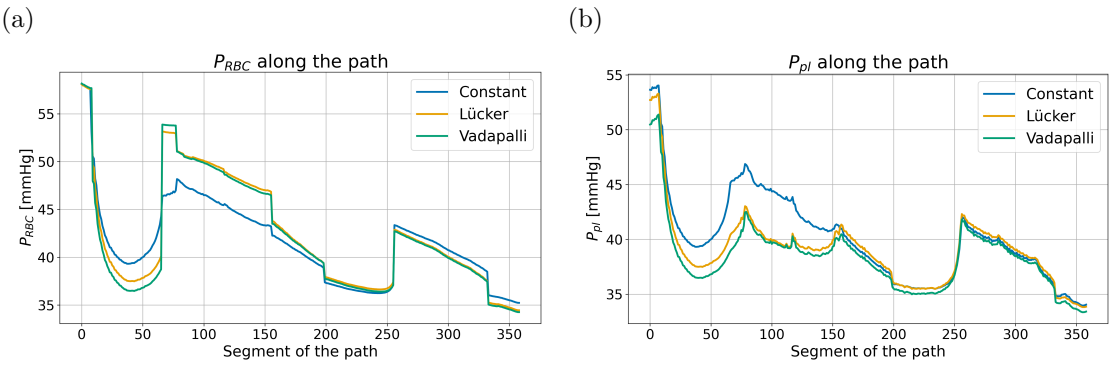

Figure 5.17: Variations of P_{RBC} (a) and P_{pl} (b) along the path for the three different methods.

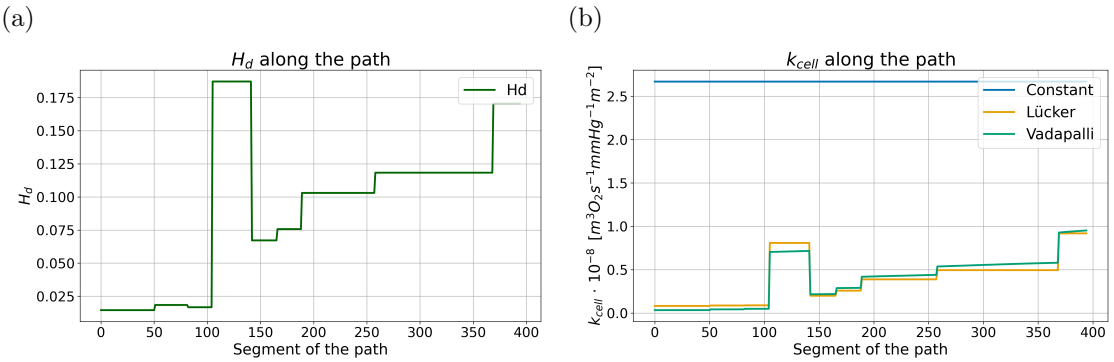

Figure 5.18: (a) Hematocrit profile along the low hematocrit path. (b) MTCs k_{C}, k_{L}, and k_{V} along the path.

Figure 5.19 shows the variations of P_{RBC} and P_{pl} along the path. Due to the uniformly low hematocrit, the differences between the methods are more pronounced than in the path with variable hematocrit. In particular, the constant k_{cell} tends to overestimate P_{pl} compared to the other two methods, with differences reaching up to 20 mmHg. A mirrored behavior is observed for P_{RBC}, where the constant k_{cell} underestimates the pressure relative to the other methods, with a maximum difference of 15 mmHg.

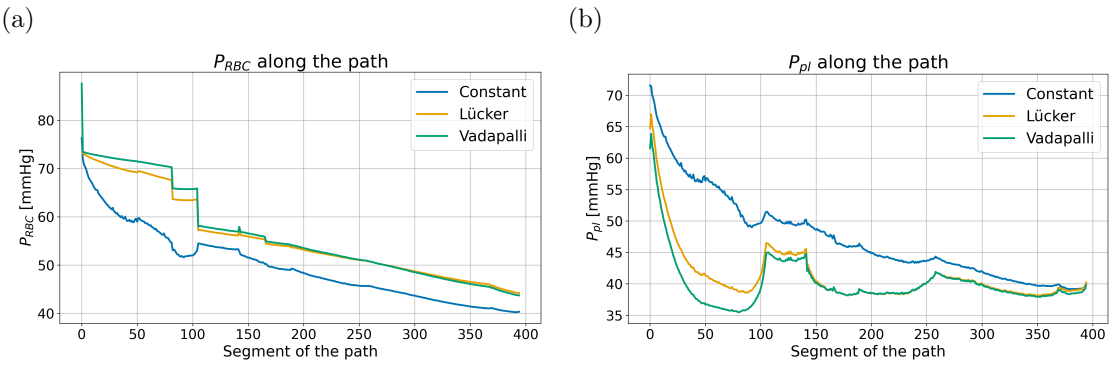

Figure 5.19: Variations of P_{RBC} (a) and P_{pl} (b) along the low hematocrit path for the three different methods.

The third path, shown in Figure 5.15 (c), is characterized by a consistently high hematocrit along its entire length. As illustrated in Figure 5.20 (a), the hematocrit remains above $H_d = 0.80$ along the entire path, the mean value is $H_d = 0.88$. In Figure 5.20 (b), both k_{L} and k_{V} exceed k_{C} throughout the path, reflecting the enhanced mass transfer due to the higher RBC concentration. Furthermore, the divergence between k_{L} and k_{V} is more evident in this case. This observation is consistent with the analysis presented in Chapter 3, which highlighted that at high hematocrit levels the influence of oxygen saturation on k_{V} becomes more pronounced.

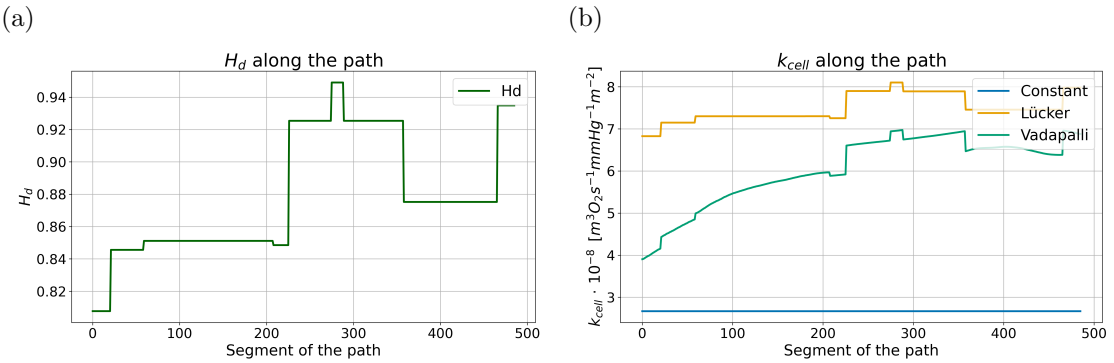

Figure 5.20: (a) Hematocrit profile along the high hematocrit path. (b) MTCs k_{C}, k_{L}, and k_{V} along the path.

Figure 5.21 shows the variations of P_{RBC} and P_{pl} along the high hematocrit path. In this case, the pressures predicted by the three methods are very similar, with no significant differences observable, unlike in the previous paths where the choice of method had a noticeable impact. This indicates that, at high hematocrit, the effect of the MTC on the predicted pressures is minimal.

(a) (b)

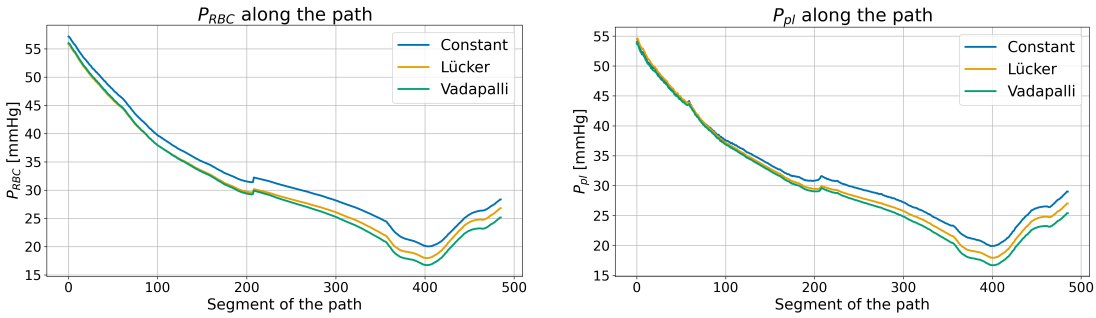

Figure 5.21: Variations of P_{RBC} (a) and P_{pl} (b) along the high hematocrit path for the three different methods.

5.2.3 Hypoxia region

Analysis of individual flow paths reveals that local variations in the MTC contribute to discrepancies between models, and these variations have a functional impact that is especially pronounced in hypoxia regions.

Following the work of Beinlich et al. [68], the hypoxia region is identified as the portion of tissue in which the oxygen partial pressure falls below 18 mmHg. Such regions are highly sensitive to even minor changes in oxygen transport, and thus provide a meaningful context for assessing the implications of the different modeling approaches. Based on this definition, the spatial distribution of the hypoxia region is reported in Figure 5.22, allowing for a direct comparison across the MTC functions.

From Figure 5.22 is possible to notice that the hypoxia region are consistently located in the upper part of the domain. The extent of this region varies across the methods: using k_{C}, it represents 0.92% of the total tissue volume, whereas with k_{L} this fraction increases to 1.61%. Finally, with k_{V} the hypoxia volume reaches 2.03% of the total domain.

A complementary analysis was carried out on the vascular network. Figure 5.23 shows the results for the vascular compartment, where the hypoxic region is defined as the portion of the network with $P_{\mathrm{RBC}} < 18$ mmHg. The spatial distribution of the hypoxia region closely matches that observed in the tissue analysis, being mainly located in the upper part of the domain. However, as for P_{T}, the extent of the hypoxia region is method-dependent, further underlining the sensitivity of oxygen availability to the choice of mass transfer formulation.

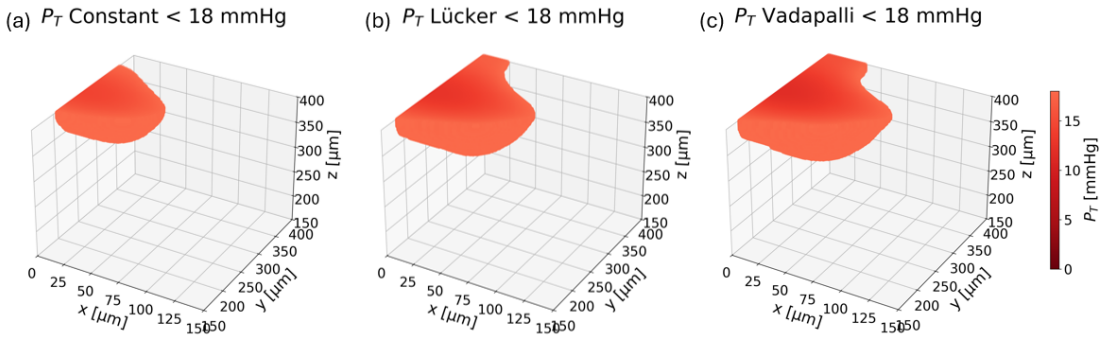

Figure 5.22: Spatial variation of the tissue oxygen partial pressure (P_{T}) for the three considered methods: Constant (a), Lücker (b), and Vadapalli (c). Regions with $P_{\mathrm{T}} < 18$ mmHg are highlighted to identify hypoxic areas.

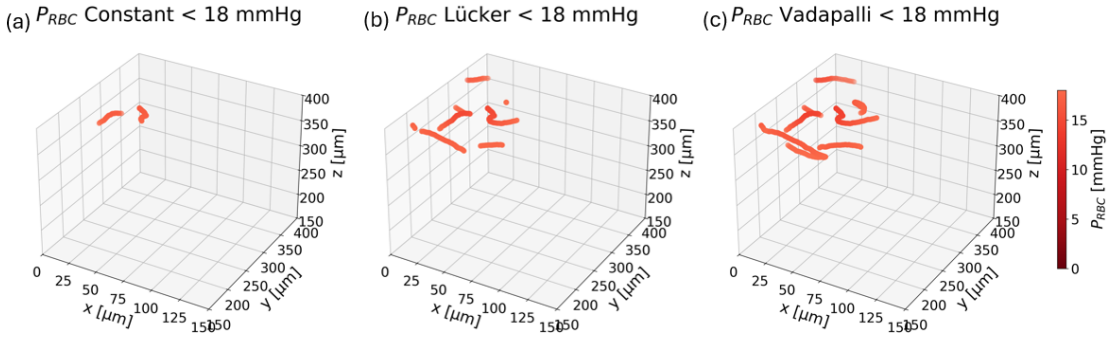

Figure 5.23: Spatial variation of the red blood cell oxygen partial pressure (P_{RBC}) for the three considered methods: Constant (a), Lücker (b), and Vadapalli (c). Regions with $P_{\mathrm{RBC}} < 18$ mmHg are highlighted to indicate hypoxic areas.

To further characterize the hypoxia region, the blood pressure distribution was examined in Figure 5.24. This analysis was performed to verify whether the identified hypoxia zone coincides with areas of preferential outflow. The results confirmed that the upper region of the domain, where hypoxia develops, is also associated with lower hydraulic pressures of the blood.

5.2.4 Computational time

The computational performance of the five networks was evaluated to provide a complete assessment of this study.

While only the outputs of Network 1 are detailed in this chapter, Table 5.1 reports the raw execution times of all networks measured on a computer with an Intel(R) Core(TM) i5-9400 CPU @ 2.90 GHz.

Since execution times strongly depend on the hardware, the mean execution

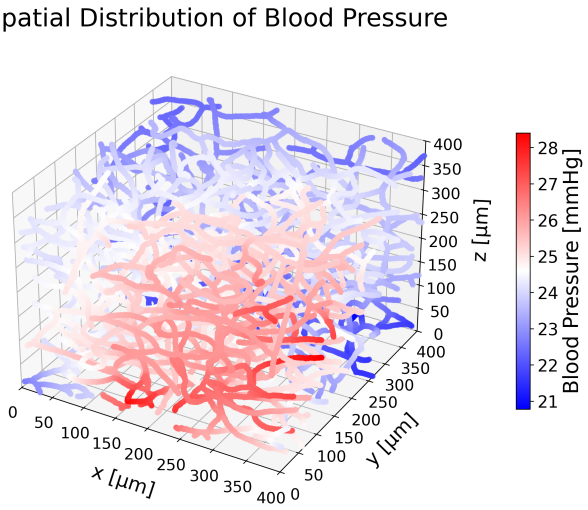

Figure 5.24: Spatial distribution of blood pressure within the vascular network. The upper part of the domain, corresponding to the hypoxia region, is characterized by reduced pressures.

Network	**Computational time [s]**			**Relative difference (% vs Constant)**	
	Constant	Lücker	Vadapalli	Lücker	Vadapalli
1	1800.629	2077.547	1671.742	+15.38%	−7.16%
2	1684.235	1555.868	1696.613	−7.62%	+0.73%
3	1660.335	1515.269	2135.515	−8.74%	+28.62%
4	1543.785	2880.595	3000.935	+86.59%	+94.39%
5	2115.329	2076.975	2112.479	−1.81%	−0.14%
Mean [s]	**1760.863**	**2021.251**	**2123.457**	**+16.76%**	**+23.29%**

Table 5.1: Execution times for the five networks and relative differences (in %) compared to the constant k_{cell}. Positive values indicate longer computation times, negative values shorter ones. The mean percentage differences were computed as the average of per-network relative differences.

times were also calculated and expressed as percentages relative to simulation with constant k_{cell}. These mean normalized times are presented in Table 5.1, allowing for a concise comparison of computational efficiency across networks, independent of the specific hardware used. The relative differences reported in Table 5.1 show a noticeable variability among networks. Most cases remain within a deviation range of approximately ±10%, while Network 4 exhibits substantially longer computation

times for both Lücker and Vadapalli. This variability reflects differences in network-specific characteristics, such as geometry or solver convergence, rather than a consistent trend across all configurations.

5.2.5 Discussions

Building upon the SV results, the analysis of the realistic MVN offers a broader framework to investigate how spatial heterogeneity in hematocrit and local differences in MTC formulation affect the overall efficiency and distribution of oxygen delivery within tissues.

Low hematocrit regions exhibit pronounced model-dependent behaviours similar to those observed in the SV simulations. In this regime, where RBCs are distant from each others, oxygen must diffuse over larger distances within the plasma before reaching the tissue. Consequently, the efficiency of the plasma–RBC exchange becomes a critical factor in determining local oxygen availability. Differences in MTC formulation thus directly translate into distinct spatial distributions of both P_{RBC} and P_{pl} along the vascular network. The constant formulation tends to overestimate oxygen transfer when H_d is low. As a result, it predicts artificially elevated plasma oxygen partial pressures and an unrealistic equilibration between the two phases. In contrast, Lücker and Vadapalli formulations scale the transfer coefficient with local hematocrit and oxygen saturation, producing more physiologically realistic gradients. These differences highlight the sensitivity of low hematocrit regions to local parameterization and underscore the importance of adapting MTCs to microvascular conditions (see Figure 5.5 and Figure 5.8).

At higher hematocrit levels, the discrepancies among the models are reduced significantly. This agreement, also observed in the SV simulations, reflects the increasing dominance of RBCs in oxygen transport. Under these conditions, hemoglobin acts as the dominant oxygen reservoir, minimizing local variation in oxygen concentration and the influence of the MTC formulation. The alignment of the models at high H_d thus reflects a physiological transition: oxygen exchange becomes limited not by interphase transfer but by saturation kinetics of hemoglobin itself. This observation reinforces the idea that the influence of MTC formulation is hematocrit-dependent: pronounced at low H_d, negligible at high H_d.

Comparing Lücker and Vadapalli formulations, only minor differences are observed across the network, particularly under high hematocrit conditions. This similarity can be explained by the relatively weak dependence of Vadapalli coefficient on local oxygen saturation (see Figure 3.7): since changes in saturation induce only minor variations in Vadapalli, the saturation-independent Lücker formulation produces comparable results. In addition, the largest differences between k_{L} and

k_V, which arise from saturation effects, occur at high hematocrit values (see Figure 5.10). As previously discussed, in this regime the overall impact of the MTC on oxygen transport is minimal. Together, these factors explain why the two models yield very similar oxygen distributions across the network.

Despite the local discrepancies among the different methods highlighted above, the frequency distributions of tissue oxygen tension remain relatively stable across models. The histograms and boxplots in Figure 5.13 and Figure 5.14 confirm that the global level of oxygen are not substantially affected by the choice of MTC. This robustness suggests that the overall oxygenation pattern is primarily dictated by the network topology (i.e., the spatial arrangement of vessels, their connectivity and length distribution), rather than by the specific MTC formulation. In other words, the microvascular architecture establishes the dominant framework for oxygen delivery, while the MTC modulates the local exchange dynamics within that structure.
However, these local deviations in tissue oxygen partial pressure should not be neglected. Local differences can reach up to 20 mmHg, as shown in the path plot in Figure 5.19, which corresponds to about 25% of the maximum tissue oxygen tension ($\sim$ 80 mmHg). Such variations may shift local regions from normoxic to near-hypoxic conditions. A closer inspection reveals that these strong discrepancies occur predominantly along vascular paths characterized by low hematocrit, where the oxygen supply is inherently limited and the system becomes more sensitive to changes in mass transfer efficiency. In regions with moderate or high H_d, these deviations are much smaller because oxygen exchange is less constrained and the higher availability of oxygen carriers mitigates the effect of MTC variations. This behavior explains why the overall distributions, obtained by integrating over the entire domain, appear more similar than the underlying pointwise results. Overall, while the global oxygenation trends remain consistent across models, the local picture reveals a different aspect: the choice of MTC can substantially influence where and how severe oxygen depletion occurs, potentially affecting the onset and extent of hypoxic microdomains.

The spatial redistribution of oxygen induced by MTC variability is not merely a numerical artifact but has clear physiological relevance. The presence of hypoxic regions is closely associated with zones where P_{RBC} and P_T are simultaneously low. These areas are typically located near vessel outflows, where oxygen has been progressively consumed along the upstream branches, and the capacity of hemoglobin to release additional oxygen becomes limited. As a result, oxygen tensions can drop below physiologically safe thresholds. This mechanism is illustrated by comparing Figure 5.22 with Figures 5.23 and 5.24, which show that low tissue oxygen levels coincide with regions of reduced RBC oxygen content. A realistic MTC formulation

is therefore essential to capture this depletion accurately. Simplified assumptions, such as a constant transfer efficiency, cannot fully represent the oxygen partial pressure differences between RBCs and plasma, because they fail to account for the dependence of oxygen exchange on local hematocrit and oxygen saturation. Consequently, the extent and severity of hypoxic microdomains may be masked.

The latest observations on local oxygen dynamics underscore the importance of the MTC choice and naturally lead to computational efficiency evaluation. More physiologically realistic formulations, such as Lücker and Vadapalli, improve the accuracy of local oxygen predictions but also require longer simulation times compared to the constant formulation, as shown in Table 5.1. On average, Lücker increases execution time by approximately 17% and Vadapalli by around 23% relative to the constant formulation. These findings highlight a trade-off between physiological fidelity and computational efficiency. For small networks or exploratory studies, the additional computational cost may be acceptable given the improved representation of oxygen dynamics. However, for large-scale networks or parametric studies, longer runtimes could become a limiting factor. Careful selection of the MTC is essential, as it determines both the localization and severity of hypoxic regions and influences the computational efficiency of simulations in realistic MVN models.

In summary, the analyses at both SV and realistic microvascular scales provide complementary insights into the mechanisms governing oxygen transport in microcirculation. The SV simulations allowed for a detailed examination of how hematocrit and MTC formulation influence local oxygen exchange, revealing the importance of capturing bidirectional dynamics between plasma and RBC compartments. Extending these observations to realistic MVNs demonstrated that, while global oxygenation patterns are largely determined by network geometry, local oxygen distribution and the emergence of hypoxic regions are strongly modulated by the choice of MTC. These findings underscore the critical role of physiologically consistent MTC formulations, which are essential not only for accurately representing local oxygen exchange but also for reliably identifying regions at risk of hypoxia in realistic microvascular network simulations.

Chapter 6

Conclusions and Future Perspectives

6.1 Concluding Remarks

This thesis investigated the role of the MTC in modeling oxygen transport in the brain. The MTC analyzed governs the exchange of oxygen between RBCs and plasma, thereby influencing both vascular and tissue oxygenation. While it is often simplified as a constant, recent studies have shown that the MTC depends on local hematocrit and oxygen saturation, reflecting the heterogeneous nature of microvascular flow and oxygen exchange.

The main objective of this work was to assess how incorporating variable MTC formulations affects oxygen transport predictions and to identify which approach provides the most reliable balance between physical realism and computational cost. Relationships between MTC, hematocrit, and oxygen saturation were extracted from literature and implemented in a 3D–1D computational framework for cerebral oxygen transport.

The numerical analysis followed a hierarchical approach. First, simplified test cases were used to isolate and quantify the effects of variable MTCs on intravascular oxygen exchange. This allowed a direct comparison of the constant, Lücker, and Vadapalli formulations under controlled conditions. Subsequently, the study was extended to a realistic MVN, where spatial heterogeneity and interaction between vessels and tissue were fully represented.

Results indicate that accounting for MTC variability improves the fidelity of the model, particularly in regions characterized by low hematocrit values. Both Lücker and Vadapalli formulations provide a physiologically consistent representation of oxygen exchange; whereas, the constant k_{cell} can lead to local deviations in oxygen levels, either underestimating or overestimating oxygen depletion depending on

local microvascular conditions. Importantly, realistic formulations like Lücker or Vadapalli produce more conservative predictions, capturing hypoxic regions that may be neglected by simplified models, thereby reducing the risk of overlooking tissue areas susceptible to oxygen deprivation.

Overall, the results across all tested networks are consistent with the main findings, indicating that the qualitative behavior of the model is robust with respect to network geometry and topology. In other words, the general trends are preserved across different network configurations. However, the quantitative predictions of local oxygen levels remain sensitive to geometric and physiological details. This distinction highlights that the conclusions are robust in terms of trends and mechanisms, but that specific numerical outcomes may vary between different vascular networks.

From the results, it can be inferred that the most suitable formulation depends on the specific goals of the study. When the objective is to capture the general distribution of oxygen across the vascular network, the constant MTC offers a computationally efficient and sufficiently accurate approximation. Conversely, when the focus is on obtaining more reliable and physiologically grounded predictions of local oxygen exchange, variable formulations should be preferred. Among these, the function extrapolated from the results obtained by Lücker [1] (see eq. (3.3)) provides the best compromise between physical accuracy and computational efficiency. The differences between Lücker and Vadapalli methods are relatively small, but the former requires a considerably lower computational cost.

These findings underline the importance of considering microvascular heterogeneity in models of cerebral oxygen transport. Neglecting the variability of the MTC can lead to an oversimplified representation of intravascular exchange and, consequently, to less accurate predictions of tissue oxygenation. By integrating a variable MTC formulation, this work advances current modeling approaches and provides a more physiologically grounded description of oxygen dynamics. This is particularly relevant in the brain, where different regions support distinct functions. Even small local reductions in oxygen availability can have region-specific effects on neural circuits, potentially leading to varied functional impairments or symptoms. By resolving these local heterogeneities, variable MTC formulations offer a more precise picture of vulnerable areas, enhancing the physiological realism of the model and providing a basis for exploring links between microvascular dysfunction, tissue hypoxia, and regional brain function.

In summary, this work underscores the importance of accounting for MTC variability to achieve realistic and computationally efficient simulations of cerebral oxygen transport.

6.2 Limitations and Outlook

Although this study provides valuable insights into the role of the MTC in cerebral oxygen transport, several limitations need to be acknowledged. The relationships between the MTC, hematocrit, and oxygen saturation were partly extrapolated from the literature, resulting in missing data in boundary regions of the parameter space. This introduces a degree of uncertainty in the extrapolated domains and may affect the accuracy of the predicted oxygen levels. Furthermore, while the qualitative trends identified in this work appear robust across different network geometries, the specific quantitative predictions are expected to vary depending on vessel arrangement, hematocrit distribution, or boundary conditions. This sensitivity implies that absolute oxygen levels should be interpreted with caution and that comparative analyses across networks or subjects require consistent model assumptions and boundary settings.

Another limitation concerns the potential dependence of the MTC on blood flow velocity. In the present model, the MTC is assumed to be independent of local flow conditions, as previous studies (e.g., Lücker [1]) have reported only a weak sensitivity of the MTC to velocity variations under physiological conditions. Therefore, neglecting this coupling represents a reasonable simplification that allows isolating the dominant effects of hematocrit and oxygen saturation. Nevertheless, blood flow still plays a key role in oxygen transport, as it determines the residence time of RBCs and, consequently, the time available for oxygen exchange within each vessel. In the present model, this indirect influence is captured through the dependence of oxygen delivery on flow changes in advective transport.

A further limitation arises from the assumption that RBCs can exchange oxygen only with the plasma phase and not directly with the surrounding tissue. In reality, direct RBC–tissue exchange can occur in situations where the available plasma layer is significantly reduced, such as in vessels with high hematocrit levels. Under these conditions, the proximity of RBCs to the vessel wall may facilitate a more efficient oxygen transfer to the tissue than what is captured by the present model. Neglecting this mechanism could therefore lead to an underestimation of oxygen delivery in high hematocrit regions. This aspect becomes particularly relevant considering that the results of this study indicate a limited impact of MTC variability at high hematocrit values. Incorporating direct RBC–tissue exchange into future modeling frameworks would thus represent an important step toward improving the physiological realism of microvascular oxygen transport simulations.

In addition, future works could investigate the mutual impact of different oxygen-transport mechanisms, such as metabolic consumption, plasma–tissue diffusion, and RBC oxygen desaturation, on the efficiency of oxygen delivery. Exploring how these factors interact with each other and with flow dynamics would provide a deeper understanding of the complex interplay between hemodynamics and oxygen

exchange in the cerebral microcirculation.

Overall, while the present study provides valuable insights into cerebral oxygen transport and the role of the MTC, the limitations discussed highlight areas where further investigation is needed. Addressing these aspects in future studies will help improve the physiological realism of the model and strengthen the generalizability of its predictions.

Appendix A

Single Vessel - Other results

This appendix presents additional results for the single vessel (SV) simulations introduced in Section 4.2. The aim is to provide further examples for different values of discharge hematocrit (H_d) and additional analyses supporting the observations discussed in the main text.

A.1 Other cases

Figures A.1 and A.2 show the oxygen partial pressure distributions for two additional discharge hematocrit values ($H_d = 0.30$ and $H_d = 0.70$), complementing the cases discussed in the main text. The MTC values used for the simulations are reported in Table A.1:

method	$k_{\mathbf{cell}}$	$\left[\mathrm{m}^3\ \mathrm{O}_2\ \mathrm{s}^{-1}\ \mathrm{mmHg}^{-1}\ \mathrm{m}^{-2}\right]$	
		$H_t = 0.30$	$H_t = 0.70$
Constant	k_{C}	$3.73 \cdot 10^{-8}$	$3.73 \cdot 10^{-8}$
Lücker-constant	$k_{\mathrm{L}}^{\mathrm{const}}$	$1.82 \cdot 10^{-8}$	$4.43 \cdot 10^{-8}$
Lücker-tangent	$k_{\mathrm{L}}^{\mathrm{tan}}$	$1.82 \cdot 10^{-8}$	$6.09 \cdot 10^{-8}$
Vadapalli	k_{V}	$k_{\mathrm{V}}(H_t = 0.25, S)$	$k_{\mathrm{V}}(H_t = 0.65, S)$

Table A.1: MTC values used in the SV simulations for two hematocrit cases.

The differences between models remain consistent across hematocrit levels, suggesting that the conclusions drawn are not limited to a specific H_d value.

(a) (b)

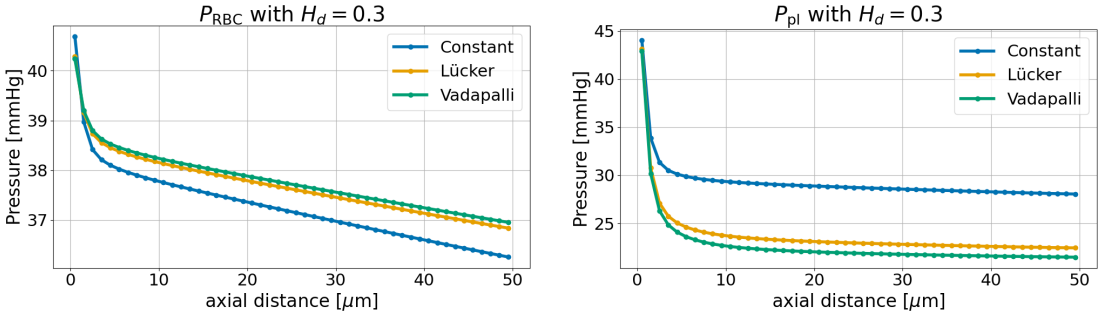

Figure A.1: Oxygen partial pressure variation along a single vessel with $H_d = 0.30$, comparing different methods. Variation of P_{RBC} (a) and P_{pl} (b) along the vessel.

(a) (b)

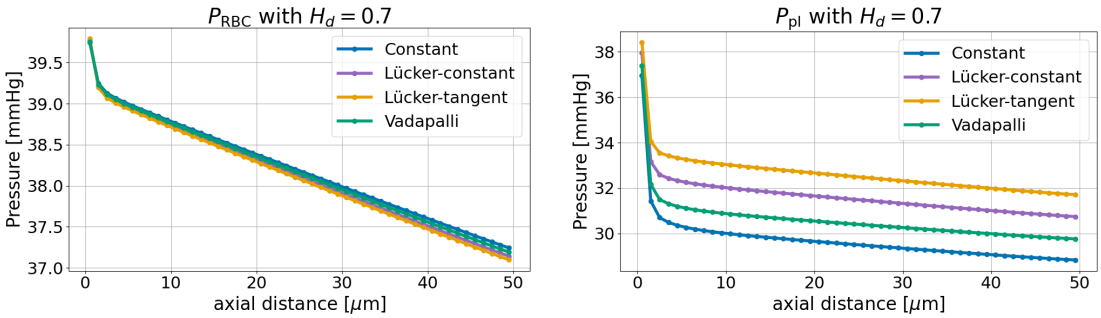

Figure A.2: Oxygen partial pressure variation along a single vessel with $H_d = 0.70$, comparing different methods. Variation of P_{RBC} (a) and P_{pl} (b) along the vessel.

A.2 Further analysis

To justify the choice of the methods used for the realistic MVN in Section 4.3, additional simulations were carried out to compare the oxygen partial pressures predicted by the four different formulations used for the SV case: Constant (k_{C}), Lücker-constant ($k_{\mathrm{L}}^{\mathrm{const}}$), Lücker-tangent ($k_{\mathrm{L}}^{\mathrm{tan}}$), and Vadapalli ($k_{\mathrm{V}}$).

Figures A.3 and A.4 show the resulting distributions of P_{pl} and P_{RBC} along the vessel for each model. All plots exhibit a decreasing trend along the vessel, consistent with the results obtained for individual hematocrit values. Moreover, both P_{RBC} and P_{pl} display an upward shift of the curves as H_d increases. This behavior is expected from a physiological standpoint, since a higher hematocrit

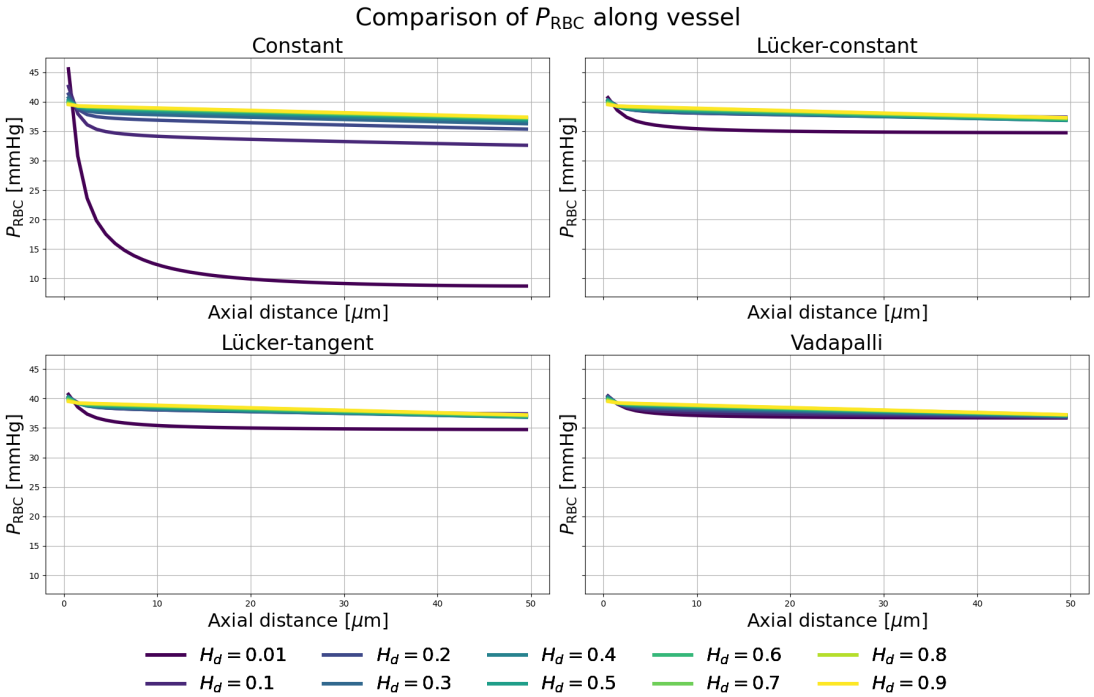

Figure A.3: Comparison of the oxygen partial pressure P_{RBC} along the vessel for four different models: Constant (upper left), Lücker-constant (upper right), Lücker-tangent (lower left), and Vadapalli (lower right).

corresponds to a larger oxygen-carrying capacity of the blood and therefore to higher oxygen partial pressures in both compartments.

When examining the P_{RBC} plots, the constant k_{cell} shows that curves corresponding to low hematocrit values deviate more markedly from the others, producing abrupt changes between successive hematocrit levels. The mirrored behavior is observed between P_{pl} and P_{RBC}, as discussed in Chapter 5. A clearer comparison between the methods analyzed can be made by focusing on P_{pl}: in this case, the constant k_{cell} produces less gradual variations with hematocrit, confirming that this formulation is not well suited to represent oxygen exchange between RBCs and plasma in a modeling framework.

Another relevant observation concerns Lücker-constant formulation. For this model, an anomaly appears for discharge hematocrit values above 0.50, where the corresponding curves overlap in upper right plot of Figure A.4 and the expected upward translation with increasing hematocrit is lost. Together with the considerations presented in Section 4.3, this outcome further supports the preference for Lücker-tangent formulation in the analysis of realistic oxygen transport models.

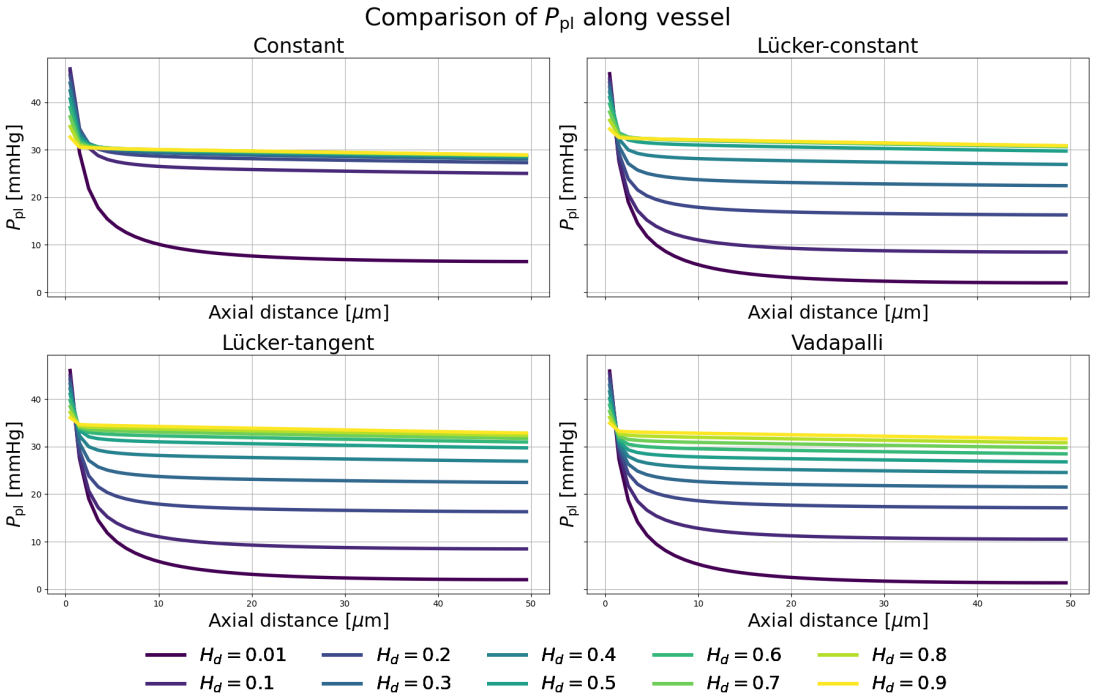

Figure A.4: Comparison of the oxygen partial pressure P_{pl} along the vessel for four different models: Constant (upper left), Lücker-constant (upper right), Lücker-tangent (lower left), and Vadapalli (lower right).

The analyses presented in this appendix provide additional insight into the SV simulations and reinforce the conclusions discussed in the main text. The results obtained for different discharge hematocrit values confirm the consistency of the model predictions under varying physiological conditions.

Appendix B

Alternative Fitting Function for Lücker Data

The polynomial function in eq. (3.1) accurately interpolates the experimental data within the accessible range ($H_t \in [0.07, 0.50]$). Outside this range, its behavior must be controlled using extrapolation strategies, such as constant or tangent extension. Within the measured range, the polynomial preserves the monotonic trend of the data and provides excellent fitting accuracy, making it the preferred formulation in the main analysis.

For completeness, an alternative logistic function was also considered to describe k_{cell} over the full physiological domain ($H_t \in [0.00, 1.00]$). The polynomial and logistic curves differ primarily at high hematocrit values, where the model predictions are less sensitive to the exact value of k_{cell}. Therefore, the logistic function is presented here as a supplementary comparison and is not used in the main simulations.

The logistic function is defined as:

$$k_{\text{L}}^{\log}(H_t) = \frac{L}{1 + \exp[-\beta\,(H_t - H_0)]} + C, \tag{B.1}$$

where the constant shift C is computed to satisfy

$$k_{\text{L}}^{\log}(0) = k_{\text{L0}}.$$

To satisfy the physical requirement that no RBC–plasma exchange occurs in the absence of erythrocytes, k_{L0} was fixed to:

$$k_{\text{L0}} = 10^{-12}\ \text{m}^3\,\text{O}_2\,\text{s}^{-1}\,\text{mmHg}^{-1}\,\text{m}^{-2},$$

ensuring that the flux term becomes negligible at $H_t = 0.00$ while preserving numerical stability of the oxygen transport solver (as previously done for the polynomial function).

In this parametrization L controls the amplitude of the logistic contribution at large hematocrit, β determines the steepness of the logistic transition, and H_0 is the inflection point of the curve. Importantly, L is not the upper asymptote by itself: the effective upper asymptotic value of the function is

$$\lim_{H_t \to +\infty} k_{\mathrm{L}}^{\log}(H_t) = L + C.$$

The fitted parameters used in the simulations are reported in Table B.1.

Coefficient	**Value**
C	$-5.550 \cdot 10^{-9}$
L	$8.021 \cdot 10^{-8}$
β	7.033
H_{50}	0.3695

Table B.1: Fitted coefficients for $k_{\mathrm{L}}^{\log}(H_t)$.

This functional form ensures a smooth, monotonic increase of the mass transfer coefficient with hematocrit and introduces a physiologically plausible saturation at high cell volume fractions, thereby avoiding unrealistically large values in regions where experimental evidence is scarce.

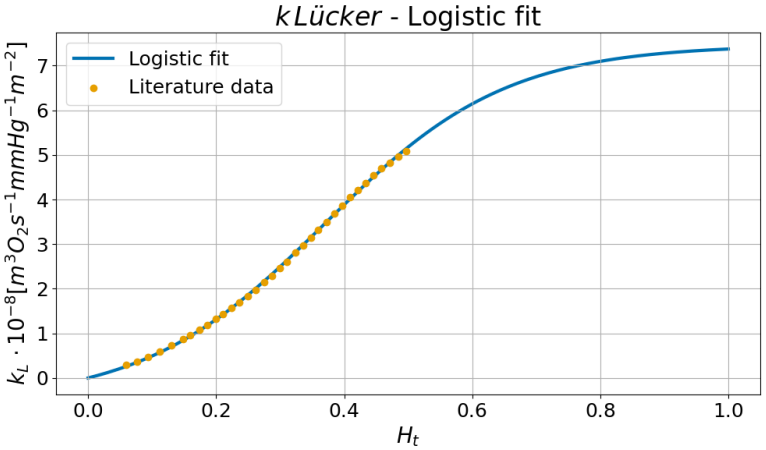

Figure B.1: Interpolated logistic function $k_{\mathrm{L}}^{\log}(H_t)$ based on data from Lücker [1].

B.1 Comparison between Lücker-tangent and Lücker-logistic Formulations

The two formulations were compared across the realistic microvascular network (MVN) to assess their impact on network-scale oxygen distributions. Both the 3D visualization and the statistical analysis presented in Figure B.2 indicate that differences between the two models are small. Local deviations in tissue oxygen partial pressure (P_T) reach at most approximately 6 mmHg, confirming that both approaches provide physiologically consistent representations of oxygen levels.

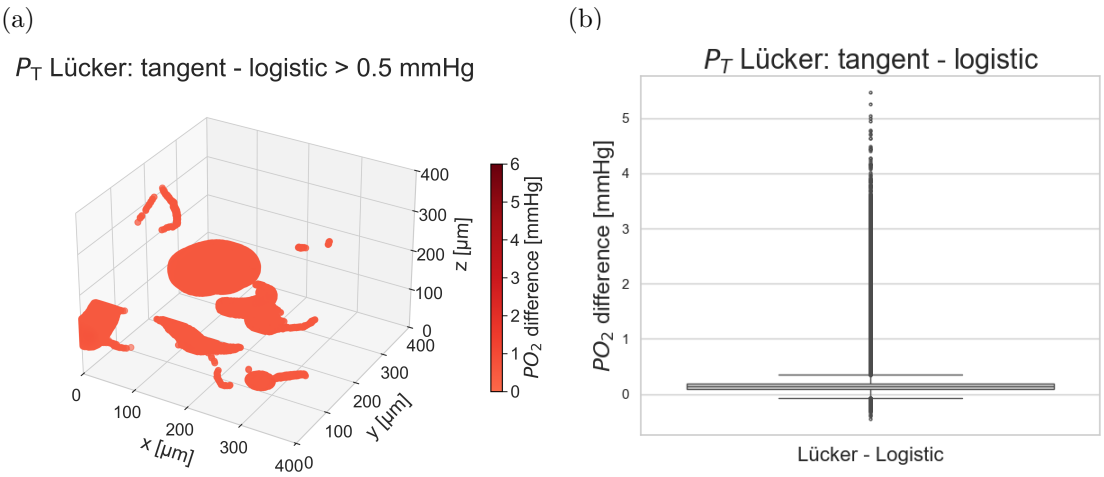

Figure B.2: Comparison of tissue oxygen partial pressure (P_T) computed using the Lücker-tangent and Lücker-logistic formulations. (a) Spatial distribution across the network. (b) Boxplot of local deviations. Differences are generally small, up to approximately 5 mmHg.

Differences in the results between the two approaches are mainly observed at low hematocrit values, where the logistic function was forced to pass through k_{L0}. Despite this adjustment, the overall impact on network-scale oxygen distributions is minimal.

Overall, these results support the use of the polynomial-based formulation in the main analysis. The logistic extrapolation remains a valid alternative, capturing a plausible biological behavior at the extremes of the hematocrit range. It does not significantly alter network-scale oxygen predictions.

Appendix C

Rationale for Bounding P_{RBC} and P_{pl} within Physiological Limits

This appendix illustrates the necessity of constraining the partial pressures of oxygen in RBCs (P_{RBC}) and plasma (P_{pl}) to the range $[0, 200]$ mmHg.

The Tsoukias rate, which models oxygen exchange between RBCs and plasma, exhibits linear behavior with respect to the gradient of these pressures (see eq. (2.9)). When the hematocrit is zero, the problem becomes ill-conditioned (as discussed in Section 4.3), thus P_{RBC} and P_{pl} values can diverge. This results in unrealistic pressure gradients (and consequently in oxygen exchanges) that should not occur, since no RBCs are present. Applying bounds on P_{RBC} and P_{pl} prevents these nonphysical behaviors and ensures that the model outputs remain meaningful across all hematocrit levels.

Figures C.1–C.3 compare the Tsoukias rate as a function of hematocrit for constant, Lücker, and Vadapalli k_{cell}.

For the constant k_{cell} (see Figure C.1), even with the [0, 200] mmHg bounds applied, the oxygen exchange rate remains relevant at zero hematocrit. This indicates that this approach is not sufficiently sensitive to hematocrit and does not correctly reflect the absence of RBCs: the predicted fluxes remain non-physiological. In contrast, both Lücker and Vadapalli methods show oxygen fluxes tending toward zero at null hematocrit, as expected biologically (see Figures C.2 and C.3).

All methods display noticeable peaks at hematocrit values around $H_d \approx 0.18$ and $H_d \approx 0.37$. The points contributing to these peaks are located near the domain boundaries (as verified through an additional analysis not reported here), and the observed behavior is likely due to non-uniform oxygen consumption close to the vessels involved.

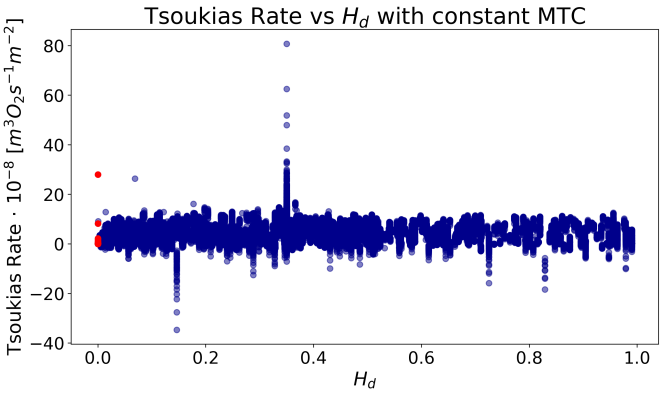

Figure C.1: Relation between the Tsoukias release rate and the discharge hematocrit H_d using a constant k_{cell}. Data points at $H_d = 0$ (highlighted in red) correspond to non-physiological conditions. These are expected to be filtered by the oxygen partial pressure limitation, but this mechanism fails in the present scenario.

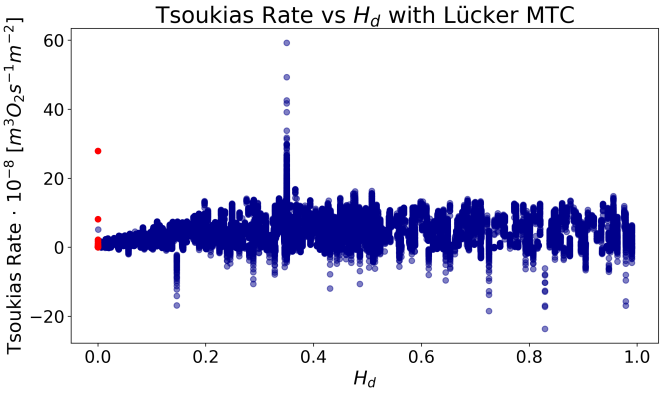

Figure C.2: Relation between the Tsoukias release rate and the discharge hematocrit H_d using Lücker function. Data points with $H_d = 0$ are highlighted in red; these correspond to non-physically admissible conditions and are supposed to be removed when the limitation on the oxygen partial pressure is applied.

For the constant k_{cell} (see Figure C.1), the rate appears largely independent of hematocrit, as evidenced by the approximately rectangular scatter of points, suggesting that under this approach oxygen exchange is not substantially modulated by the hematocrit. In contrast, both Lücker and Vadapalli methods exhibit an increase in oxygen flux with rising hematocrit (see Figures C.2 and C.3). Biologically, this behavior reflects the fact that higher RBC concentrations increase oxygen availability, thereby facilitating greater exchange between RBCs and plasma.

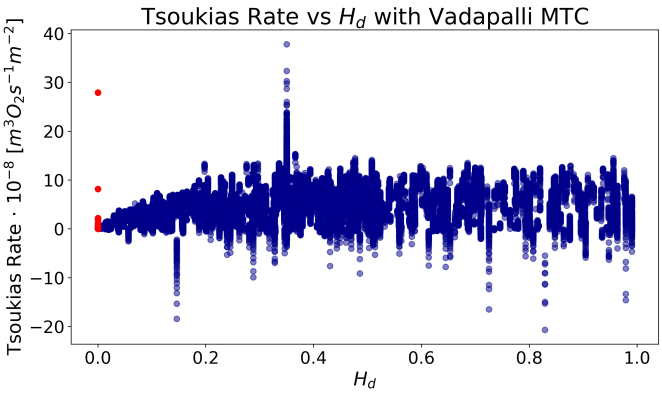

Figure C.3: Relation between the Tsoukias release rate and the discharge hematocrit H_d using Vadapalli function. Data points with $H_d = 0$ are highlighted in red; these correspond to non-physically admissible conditions and are removed when the limitation on the oxygen partial pressure is applied.

Bounding P_{RBC} and P_{pl} within reasonable limits is essential to maintain model stability and produce biologically meaningful outputs. The [0, 200] mmHg constraint prevents non-physiological oxygen gradients and fluxes at low or zero hematocrit, while allowing the model to capture realistic trends for different hematocrit levels. Among the tested approaches, Lücker and Vadapalli methods respond appropriately to this constraint, showing vanishing fluxes at null hematocrit, whereas the constant k_{cell} remains insensitive to hematocrit and continues to predict non-physiological exchanges. Nevertheless, applying these bounds ensures overall stability and comparability across methods.

Appendix D

Other MVNs

This appendix presents the results obtained for two additional MVNs, analyzed using the same methodology described in Chapter 5. The purpose is to verify the consistency and robustness of the findings across different networks. Only the main quantitative and qualitative outcomes are shown here, while the detailed discussion is omitted since the trends are analogous to those reported in the main text. The same threshold values adopted in Chapter 5 were used here as well, in order to enable a direct and consistent comparison among the different networks.

For both networks, the mean discharge hematocrit (H_d) was 0.30, used to set the constant MTC $k_C = 1.82 \cdot 10^{-8}\,\mathrm{m^3O_2s^{-1}mmHg^{-1}m^{-2}}$ as described in Section 4.3.

Figure D.1 shows the distribution of H_d across vessels. The first bin (0–0.20) is partially highlighted in red to indicate vessels with $H_d < 0.001$. These percentages refer to the portion of vessels not considered in the subsequent analyses, as already discussed for the results presented in Chapter 5.

As discussed in Chapter 5, the global distribution of tissue oxygen partial pressure remains largely consistent across the different methods (see Figure D.3). Nevertheless, differences become evident upon closer inspection of the boxplots, which exhibit numerous and non-negligible outliers (see Figure D.4).

In these networks differences between the methods become evident at low hematocrit values when comparing Lücker and constant k_{cell} (see Figures D.6 and D.2), confirming what observed in Chapter 5. For the comparison between Vadapalli and constant k_{cell}, discrepancies arise either at low hematocrit values or high oxygen saturation (see Figures D.7, D.2, and D.5). Finally, when comparing Vadapalli and Lücker methods, differences emerge mainly at high oxygen saturation and non-zero hematocrit values (see Figure D.8, D.2, and D.5).

Overall, the results across all tested networks are broadly consistent with the main findings, indicating that the model's behavior is generally robust with

(a) (b)

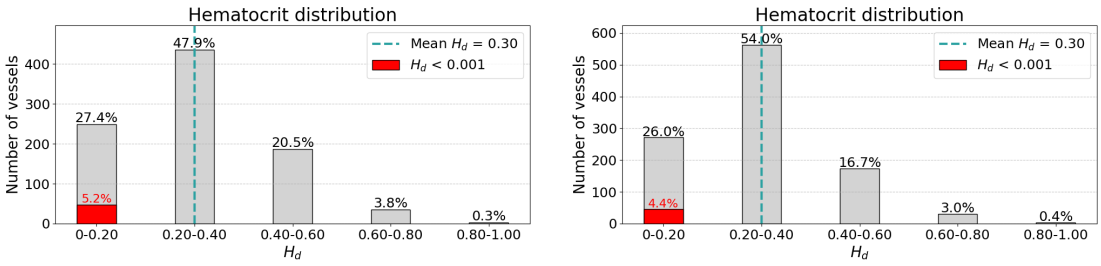

Figure D.1: Discharge hematocrit (H_d) distribution across vessels for Network 2 (a) and Network 3 (b). The first bin (0–0.20) is partially highlighted in red to indicate vessels with $H_d < 0.001$. Percentages refer to the total vessel count, while the dashed line marks the overall mean H_d.

(a) (b)

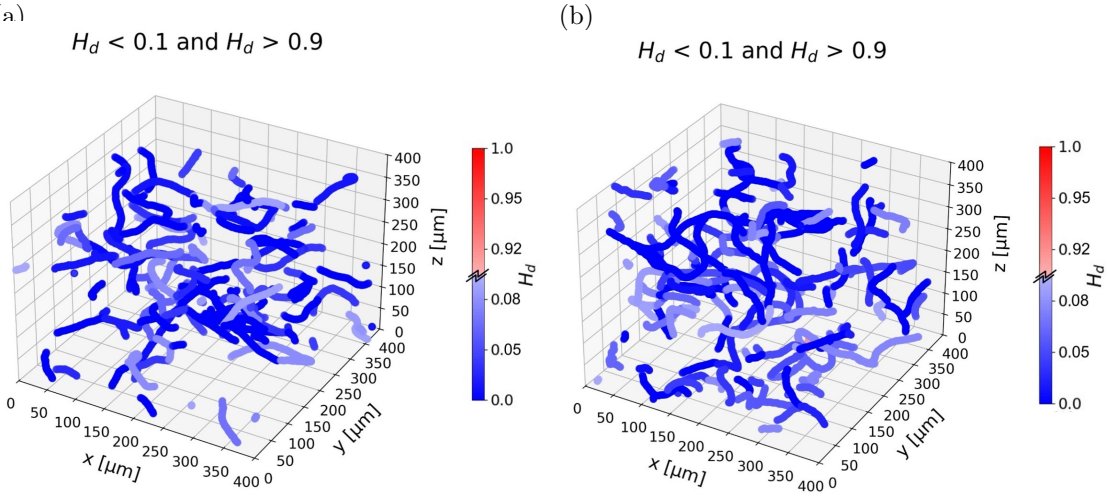

Figure D.2: Distribution of discharge hematocrit (H_d) within the vascular network for Network 2 (a) and Network 3 (b). Only vessels with very low ($H_d < 0.1$) or very high ($H_d > 0.9$) hematocrit values are displayed.

respect to typical variations in network geometry and topology. However, extreme differences in vessel arrangement, density, or boundary conditions could still lead to local deviations in oxygen distribution, especially in regions of low hematocrit or limited plasma availability.

(a) (b)

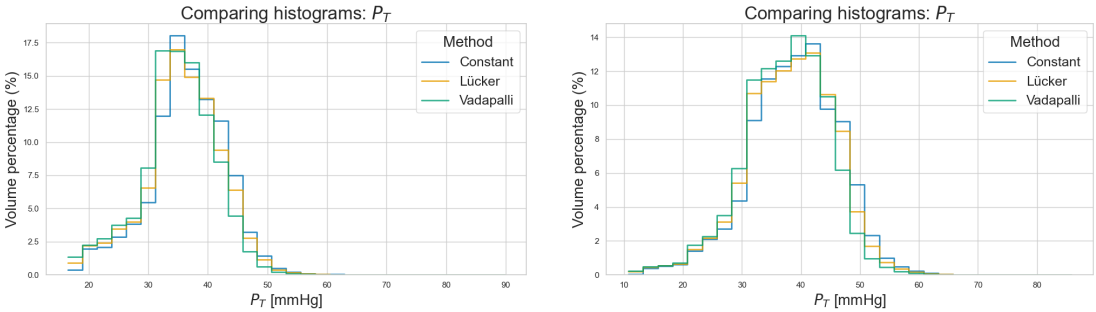

Figure D.3: Frequency distribution of P_{T} for the different methods are compared for Network 2 (a) and Network 3 (b).

(a) (b)

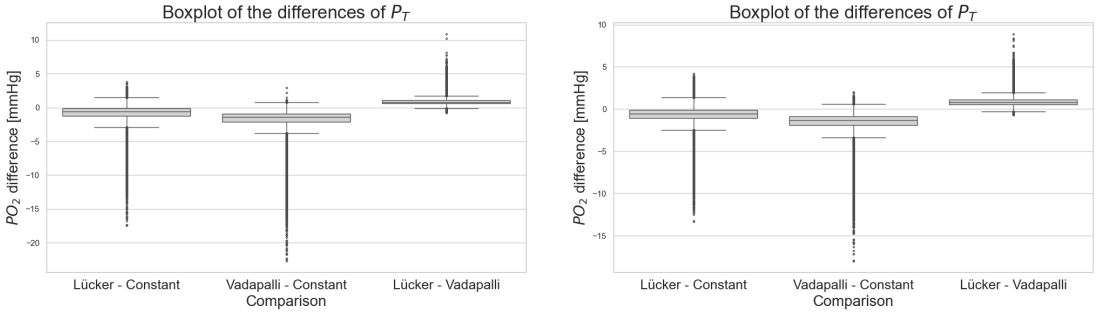

Figure D.4: Boxplots of the differences in P_{T} for the three model comparisons for Network 2 (a) and Network 3 (b).

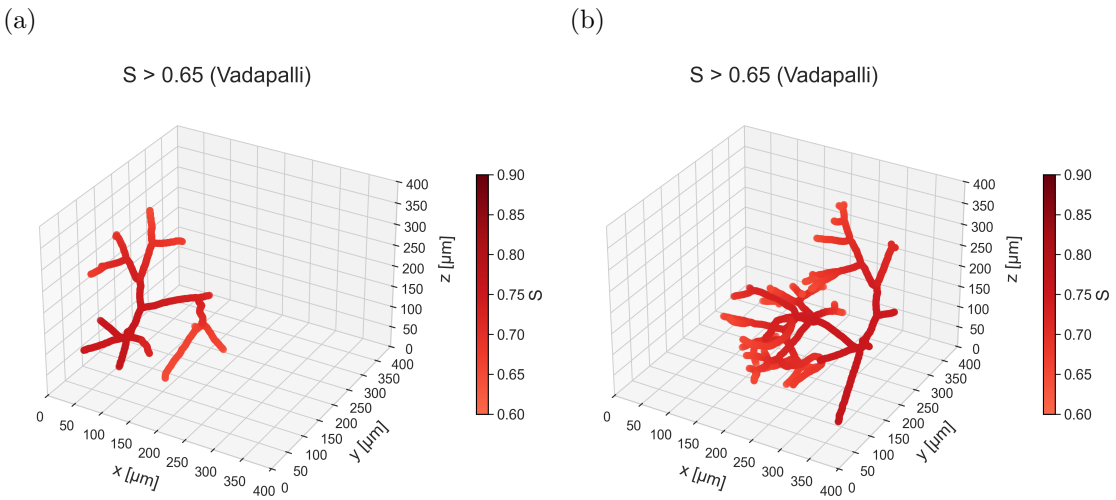

Figure D.5: Distribution of oxygen saturation (using Vadapalli method) for Network 2 (a) and Network 3 (b). Only vessels with a saturation greater than 0.65 are displayed.

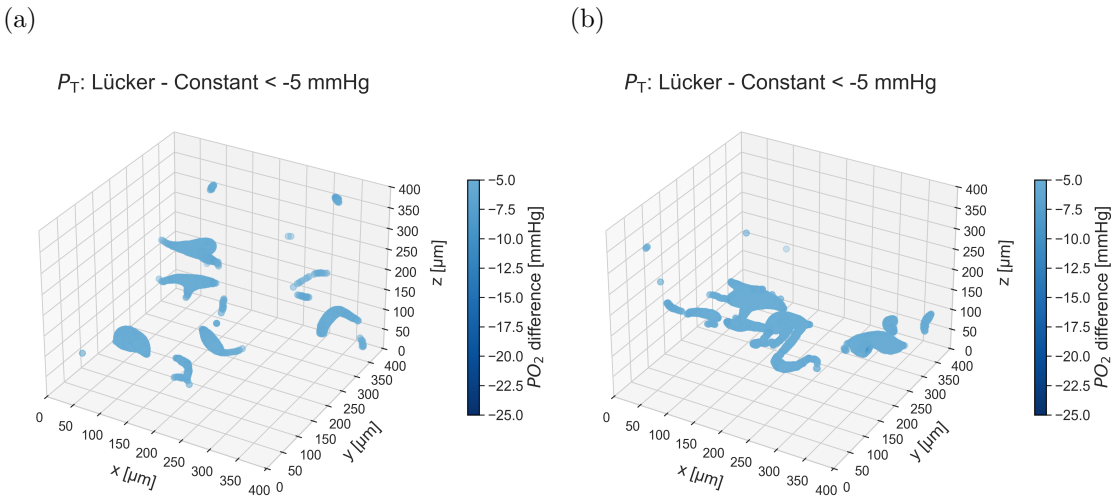

Figure D.6: Spatial distribution of the difference in tissue oxygen partial pressure (P_T) between Lücker and constant k_{cell} for Network 2 (a) and Network 3 (b).

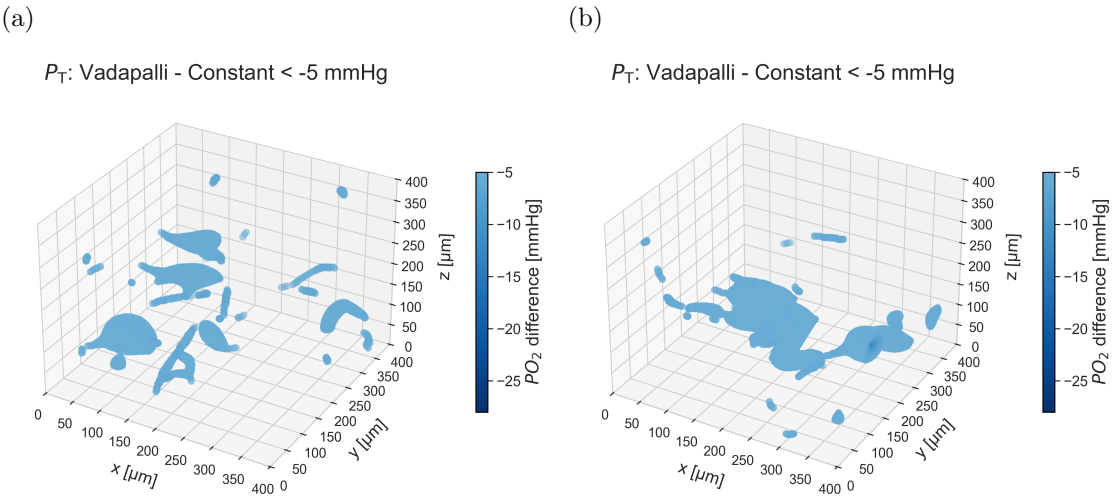

Figure D.7: Spatial distribution of the difference in tissue oxygen partial pressure (P_T) between Vadapalli and constant k_{cell} for Network 2 (a) and Network 3 (b).

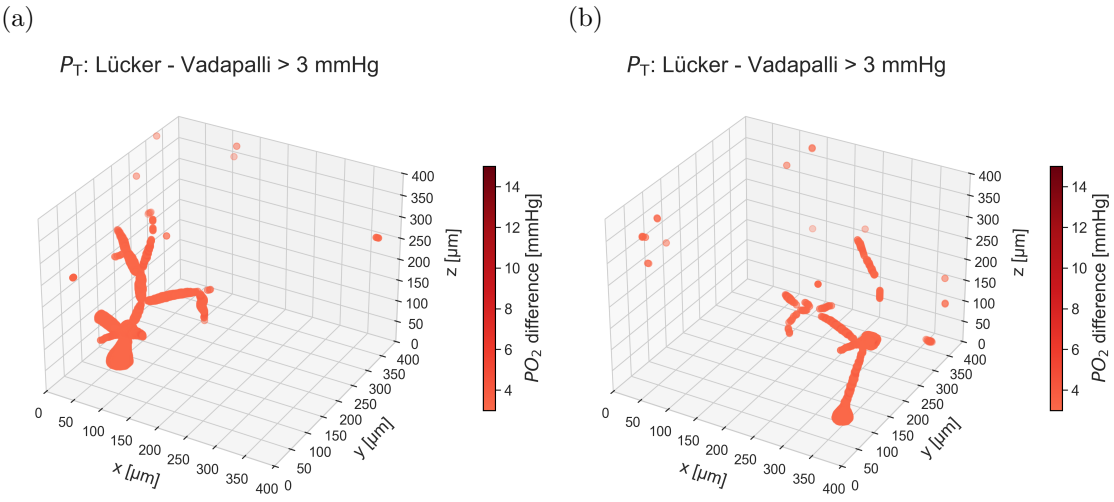

Figure D.8: Spatial distribution of the difference in tissue oxygen partial pressure (P_T) between Lücker and Vadapalli methods for Network 2 (a) and Network 3 (b).

Bibliography

[1] Adrien Lücker. «Computational Modeling of Oxygen Transport in the Microcirculation: From an Experiment-Based Model to Theoretical Analyses». PhD thesis. ETH Zurich, 2017. DOI: 10.3929/ethz-b-000181551. URL: https://doi.org/10.3929/ethz-b-000181551 (cit. on pp. ii, 1, 10, 13, 18, 26, 28–30, 32, 33, 47, 48, 73, 74, 82).

[2] Arjun Vadapalli, Daniel Goldman, and Aleksander S. Popel. «Calculations of Oxygen Transport by Red Blood Cells and Hemoglobin Solutions in Capillaries». In: *Artificial Cells, Blood Substitutes, and Biotechnology* 30.3 (2002), pp. 157–188. DOI: 10.1081/BIO-120004338 (cit. on pp. ii, 26, 28–30, 33–35).

[3] D. F. Rolfe and G. C. Brown. «Cellular energy utilization and molecular origin of standard metabolic rate in mammals». In: *Physiological Reviews* 77.3 (1997), pp. 731–758 (cit. on p. 1).

[4] P. J. Magistretti and L. Pellerin. «Cellular mechanisms of brain energy metabolism and their relevance to functional brain imaging». In: *Philosophical Transactions of the Royal Society B: Biological Sciences* 354.1387 (July 1999), pp. 1155–1163. DOI: 10.1098/rstb.1999.0471 (cit. on p. 1).

[5] John E. Hall and Arthur C. Guyton. *Guyton and Hall Textbook of Medical Physiology*. 13th. Philadelphia: Elsevier, 2016 (cit. on p. 2).

[6] Henry Gray. *Anatomy of the Human Body*. Philadelphia: Lea & Febiger, 1918 (cit. on p. 3).

[7] S. Hirsch, J. Reichold, M. Schneider, G. Szekely, and B. Weber. «Topology and hemodynamics of the cortical cerebrovascular system». In: *Journal of Cerebral Blood Flow & Metabolism* 32 (2012), pp. 952–967 (cit. on p. 3).

[8] F. Schmid, M. Barret, P. Jenny, and B. Weber. «Vascular density and distribution in neocortex». In: *NeuroImage* (2017) (cit. on p. 3).

[9] Cleveland Clinic. *Blood, Part 1*. https://my.clevelandclinic.org/health/body/24836-blood. 2023 (cit. on p. 3).

[10] School of Chemistry, Bristol University. *Hemoglobin*. https://web.archive.org/web/20091113230316/http://www.chm.bris.ac.uk/motm/hb/hemoglobin.htm. Archived 13 Nov 2009. Accessed 12 Oct 2009. 2009 (cit. on p. 3).

[11] Manuel Diez-Silva, Ming Dao, Jongyoon Han, Chwee Teck Lim, and Subra Suresh. «Shape and Biomechanical Characteristics of Human Red Blood Cells in Health and Disease». In: *Frontiers in Physiology* 1 (2010), p. 30. DOI: 10.3389/fphys.2010.00030. URL: https://www.frontiersin.org/articles/10.3389/fphys.2010.00030 (cit. on p. 4).

[12] Dominik Obrist. *Lecture 2 - Blood Rheology*. https://www.youtube.com/watch?v=lq5ZDDr-VqQ. 2022 (cit. on pp. 4, 6, 7).

[13] Timothy W. Secomb. «Blood flow in the microcirculation». In: *Annual Review of Fluid Mechanics* 49 (2017), pp. 443–461. URL: http://arjournals.annualreviews.org/loi/fluid (cit. on p. 5).

[14] Franca Schmid, Philbert S Tsai, David Kleinfeld, Patrick Jenny, and Bruno Weber. «Depth-dependent flow and pressure characteristics in cortical microvascular networks». In: *PLoS Computational Biology* 13.2 (2017), e1005392 (cit. on pp. 4, 23, 43, 44).

[15] Alexander S. Popel and Philip C. Johnson. «Microcirculation and Hemorheology». In: *Annual Review of Fluid Mechanics* 37 (2005), pp. 43–69. DOI: 10.1146/annurev.fluid.37.042604.133933 (cit. on p. 4).

[16] Frank M. White. *Fluid Mechanics*. 7th. New York, USA: McGraw-Hill Education, 2011 (cit. on p. 4).

[17] John R. Womersley. «Method for the calculation of velocity, rate of flow and viscous drag in arteries when the pressure gradient is known». In: *The Journal of Physiology* 127.3 (1955), pp. 553–563. DOI: 10.1113/jphysiol.1955.sp005276 (cit. on p. 4).

[18] W. R. Dean. «Note on the motion of fluid in a curved pipe». In: *The London, Edinburgh, and Dublin Philosophical Magazine and Journal of Science* 4.20 (1927), pp. 208–223. DOI: 10.1080/14786440708564324 (cit. on p. 5).

[19] Daniel Goldman and Aleksander S. Popel. «A computational study of the effect of capillary network anastomoses and tortuosity on oxygen transport». In: *Journal of Theoretical Biology* 206.2 (2000), pp. 181–194. DOI: 10.1006/jtbi.2000.2113 (cit. on pp. 5, 27).

[20] A. R. Pries, T. W. Secomb, P. Gaehtgens, and J. F. Gross. «Blood Flow in Microvascular Networks: Experiments and Simulation». In: *Circulation Research* 67.4 (1990), pp. 826–834. DOI: 10.1161/01.res.67.4.826 (cit. on pp. 7–9, 30).

[21] H.W. Song, K.L. Foreman, B.D. Gastfriend, J.S. Kuo, S.P. Palecek, and E.V. Shusta. «Transcriptomic comparison of human and mouse brain microvessels». In: *Scientific Reports* 10.1 (July 2020), p. 12358. DOI: 10.1038/s41598-020-69096-7 (cit. on p. 11).

[22] N. Abbasizadeh and J. A. Spencer. «Two-Photon Phosphorescence Lifetime Microscopy». In: *Advances in Experimental Medicine and Biology*. Vol. 3233. 2021, pp. 63–82. DOI: 10.1007/978-981-15-7627-0_4 (cit. on p. 11).

[23] Elizabeth M. C. Hillman. «Coupling mechanism and significance of the BOLD signal: a status report». In: *Annual Review of Neuroscience* 37 (2014), pp. 161–181. DOI: 10.1146/annurev-neuro-071013-014111 (cit. on p. 11).

[24] J. Condrau et al. «ECgo: All-Optical Induction of Single Endothelial Cell Injury and Capillary Occlusion in the Brain». In: *bioRxiv* (May 2025). Preprint, p. 2025.05.27.656398. DOI: 10.1101/2025.05.27.656398 (cit. on p. 11).

[25] August Krogh. «The number and distribution of capillaries in muscles with calculations of the oxygen pressure head necessary for supplying the tissue». In: *The Journal of Physiology* 52.6 (1919), pp. 409–415 (cit. on p. 12).

[26] J. D. Hellums. «The resistance to oxygen transport in the capillaries relative to that in the surrounding tissue». In: *Microvascular Research* 13.1 (1977), pp. 131–136. DOI: 10.1016/0026-2862(77)90122-4 (cit. on p. 12).

[27] J.D. Hellums, P.K. Nair, N.S. Huang, and N. Ohshima. «Simulation of intraluminal gas transport processes in the microcirculation». In: *Annals of Biomedical Engineering* 24 (1996), pp. 1–24. DOI: 10.1007/BF02770991 (cit. on pp. 12, 27, 35).

[28] Daniel Goldman. «Theoretical models of microvascular oxygen transport to tissue». In: *Microcirculation* 15.8 (2008), pp. 795–811. DOI: 10.1080/10739680801938289 (cit. on pp. 12, 13, 18, 19, 47).

[29] Alexander S. Popel. «Analysis of capillary-tissue diffusion in multicapillary systems». In: *Mathematical Biosciences* 39.3-4 (1978), pp. 187–211. DOI: 10.1016/0025-5564(78)90053-6 (cit. on p. 13).

[30] Alexander S. Popel, Charles Charny, and Alexander Dvinsky. «Effect of heterogeneous oxygen delivery on the oxygen distribution in skeletal muscle». In: *Mathematical Biosciences* 81.1 (1986), pp. 91–113. DOI: 10.1016/0025-5564(86)90164-1 (cit. on p. 13).

[31] L. Hoofd and Z. Turek. «Realistic modelling of capillary spacing in dog gracilis muscle greatly influences the heterogeneity of calculated tissue oxygen pressures». In: *Oxygen Transport to Tissue XVII*. Ed. by C. Ince, J. Kesecioglu, L. Telci, and K. Akpir. Boston, MA: Springer US, 1996, pp. 333–340. DOI: 10.1007/978-1-4613-0333-6_43 (cit. on p. 13).

[32] Timothy W. Secomb and Roy Hsu. «Analysis of oxygen delivery to tissue by microvascular networks». In: *Oxygen Transport to Tissue X*. Ed. by M. Mochizuki, C.R. Honig, T. Koyama, T.K. Goldstick, and D.F. Bruley. Boston, MA: Springer US, 1988, pp. 95–103. DOI: 10.1007/978-1-4615-9510-6_11 (cit. on p. 13).

[33] TW Secomb, R Hsu, EY Park, and MW Dewhirst. «Green's function methods for analysis of oxygen delivery to tissue by microvascular networks». In: *Annals of biomedical engineering* 32.11 (Nov. 2004), pp. 1519–1529. DOI: 10.1114/b:abme.0000049036.08817.44 (cit. on p. 13).

[34] Daniel Goldman and Aleksander S. Popel. «Computational modeling of oxygen transport from complex capillary networks». In: *Oxygen Transport to Tissue XXI*. Ed. by A. Eke and D.T. Delpy. Vol. 471. Advances in Experimental Medicine and Biology. Springer US, 1999, pp. 555–563. DOI: 10.1007/978-1-4615-4717-4_65 (cit. on p. 13).

[35] Gaia Stievano. «Modeling of oxygen transport in realistic microvascular networks: Studying the impact of perfusion heterogeneities and microvascular alterations». PhD thesis in preparation. PhD thesis. University of Bern, 2024 (cit. on pp. 15, 17, 20, 26, 43).

[36] M. Kobari, F. Gotoh, Y. Fukuuchi, K. Tanaka, N. Suzuki, and D. Uematsu. «Blood flow velocity in the pial arteries of cats, with particular reference to the vessel diameter». In: *Journal of Cerebral Blood Flow & Metabolism* 4.1 (1984), pp. 110–114 (cit. on p. 15).

[37] E. Gutiérrez-Jiménez, C. Cai, I.K. Mikkelsen, P.M. Rasmussen, H. Angleys, M. Merrild, and et al. «Effect of electrical forepaw stimulation on capillary transittime heterogeneity (CTH)». In: *Journal of Cerebral Blood Flow & Metabolism* (2016), p. 0271678X16631560 (cit. on p. 15).

[38] M. Schulte, J. Wood, and A. Hudetz. «Cortical electrical stimulation alters erythrocyte perfusion pattern in the cerebral capillary network of the rat». In: *Brain Research* 963.1 (2003), pp. 81–92 (cit. on p. 15).

[39] EBSCO Information Services. *Interstitial Fluid*. Accessed: 2025-10-24. 2025. URL: https://www.ebsco.com/research-starters/science/interstitial-fluid (cit. on p. 16).

[40] Gilbert S. Adair. «The hemoglobin system. VI. The oxygen dissociation curve of hemoglobin». In: *Journal of Biological Chemistry* 63 (1925), pp. 529–545 (cit. on p. 18).

[41] A. Clark, W. Federspiel, P. Clark, and G. Cokelet. «Oxygen delivery from red cells». In: *Biophysical Journal* 47.2 (1985), pp. 171–181. DOI: 10.1016/S0006-3495(85)83890-X (cit. on pp. 18, 47).

[42] Nikolaos M. Tsoukias, Daniel Goldman, Arjun Vadapalli, Roland N. Pittman, and Aleksander S. Popel. «A computational model of oxygen delivery by hemoglobin-based oxygen carriers in three-dimensional microvascular networks». In: *Journal of Theoretical Biology* 248.2 (2007), pp. 457–474. DOI: 10.1016/j.jtbi.2007.06.003 (cit. on pp. 18, 26).

[43] O. Kedem and A. Katchalsky. «Thermodynamic analysis of the permeability of biological membranes to non-electrolytes». In: *Biochimica et Biophysica Acta* 27 (1958), pp. 229–246 (cit. on p. 19).

[44] O. Kedem and A. Katchalsky. «A physical interpretation of the phenomenological coefficients of membrane permeability». In: *The Journal of General Physiology* 45 (1961), pp. 143–179 (cit. on p. 19).

[45] Timo Koch. «Mixed-dimension models for flow and transport processes in porous media with embedded tubular network systems». PhD thesis. Stuttgart: Universität Stuttgart, 2020. DOI: 10.18419/opus-10975. URL: https://elib.uni-stuttgart.de/items/849f03b0-908e-4ffd-8d2d-aa5ca07a4870 (cit. on pp. 19, 24).

[46] Aleksander S. Popel, Tuhin K. Roy, and Abhijit Dutta. «Distribution of Intravascular and Extravascular Resistances to Oxygen Transport». In: (1998). Ed. by James B. Bassingthwaighte, John H. Linehan, and Calvin A. Goresky, pp. 153–165. DOI: 10.1007/978-1-4612-2184-5_12 (cit. on pp. 27, 28).

[47] Tuhin K. Roy and Timothy W. Secomb. «Chapter 6 - Fundamental principles of oxygen transport in the microcirculation». In: *On Oxygen*. Ed. by Michael J. Joyner and Jerome A. Dempsey. Fundamentals of Physiology. Academic Press, 2025, pp. 169–189. DOI: https://doi.org/10.1016/B978-0-443-21877-4.00006-1 (cit. on p. 36).

[48] Timo Koch, Dennis Gläser, Kilian Weishaupt, et al. «DuMux 3 – an open-source simulator for solving flow and transport problems in porous media with a focus on model coupling». In: *Computers & Mathematics with Applications* 81 (2021), pp. 423–443. DOI: 10.1016/j.camwa.2020.02.012 (cit. on p. 38).

[49] DuMuX Developers. *DuMuX Handbook, version 3.7*. https://dumux.org/docs/handbook/releases/3.7/dumux-handbook.pdf. Accessed: 2025-09-26. 2025 (cit. on p. 38).

[50] DuMux Development Team. *Newton Solver Documentation*. Accessed: October 29, 2024. 2024. URL: https://dumux.org/docs/doxygen/master/group___newton.html (visited on 10/29/2024) (cit. on p. 39).

[51] DuMuX developers / Dennis Gläser. *Embedded Network 1D3D: Problem description*. https://git.iws.uni-stuttgart.de/dumux-repositories/dumux/-/blob/master/examples/embedded_network_1d3d/doc/problem.md. 2023 (cit. on pp. 39, 40).

[52] Timo Koch. «Projection-based resolved interface 1D-3D mixed-dimension method for embedded tubular network systems». In: *Computers & Mathematics with Applications* 109 (2022), pp. 15–29. ISSN: 0898-1221. DOI: 10.1016/j.camwa.2022.01.021. URL: https://www.sciencedirect.com/science/article/pii/S089812212200027X (cit. on p. 39).

[53] A. A. Linninger, I. G. Gould, T. Marrinan, C. Y. Hsu, M. Chojecki, and A. Alaraj. «Cerebral microcirculation and oxygen tension in the human secondary cortex». In: *Annals of Biomedical Engineering* 41.11 (Nov. 2013). Epub 2013 Jul 11. Erratum in: Ann Biomed Eng. 2014 Aug;42(8):1790; Erratum in: Ann Biomed Eng. 2016 Nov;44(11):3433. doi: 10.1007/s10439-016-1722-3, pp. 2264–2284. DOI: 10.1007/s10439-013-0828-0 (cit. on p. 40).

[54] William C. Shiel Jr. and Sruthi M. *Hematocrit Ranges (Normal, High, Low)*. 2024. URL: https://www.medicinenet.com/hematocrit/article.htm (cit. on p. 41).

[55] Cintia Klaudia Finszter, Róbert Kemecsei, Gergely Zachar, Sophie Holtkamp, Diego Echevarría, István Adorján, Ágota Ádám, and András Csillag. «Early cellular and synaptic changes in dopaminoceptive forebrain regions of juvenile mice following gestational exposure to valproate». In: *Frontiers in Neuroanatomy* Volume 17 - 2023 (2023). ISSN: 1662-5129. DOI: 10.3389/fnana.2023.1235047. URL: https://www.frontiersin.org/journals/neuroanatomy/articles/10.3389/fnana.2023.1235047 (cit. on p. 43).

[56] F. Schmid. «Cerebral blood flow modeling with discrete tracking of red blood cells – analyzing microvascular networks and their perfusion». Supervisor: Prof. Patrick Jenny, Defense date: June 15, 2017. PhD Thesis. ETH Zürich, Institute of Fluid Dynamics, 2017 (cit. on p. 43).

[57] Franca Schmid, Robert Epp, and Chryso Lambride. *microBlooM*. https://github.com/Franculino/microBlooM. GitHub repository. 2025 (cit. on pp. 44, 47).

[58] Declan G Lyons, Alexandre Parpaleix, Morgane Roche, and Serge Charpak. «Mapping oxygen concentration in the awake mouse brain». In: *eLife* 5 (Feb. 2016). Ed. by David Kleinfeld. ISSN: 2050-084X. DOI: 10.7554/eLife.12024. URL: https://doi.org/10.7554/eLife.12024 (cit. on pp. 45, 48).

[59] Philip L. Altman and Dorothy S. Dittmer. «Respiration and Circulation». In: 1971. URL: https://api.semanticscholar.org/CorpusID:80731927 (cit. on p. 47).

[60] C. Christoforides, L. H. Laasberg, and J. Hedley-Whyte. «Effect of temperature on solubility of O2 in human plasma». In: *Journal of Applied Physiology* 26.1 (1969), pp. 56–60. DOI: 10.1152/jappl.1969.26.1.56 (cit. on p. 47).

[61] M. Mahler, C. Louy, E. Homsher, and A. Peskoff. «Reappraisal of diffusion, solubility, and consumption of oxygen in frog skeletal muscle, with applications to muscle energy balance». In: *The Journal of General Physiology* 86.1 (1985), pp. 105–134. DOI: 10.1085/jgp.86.1.105 (cit. on p. 47).

[62] T. B. Bentley, H. Meng, and R. N. Pittman. «Temperature dependence of oxygen diffusion and consumption in mammalian striated muscle». In: *American Journal of Physiology - Heart and Circulatory Physiology* 264.6 (1993), H1825–H1830 (cit. on p. 47).

[63] C. Y. Liu, S. G. Eskin, and J. D. Hellums. «The oxygen permeability of cultured endothelial cell monolayers». In: *Advances in Experimental Medicine and Biology*. Springer Nature, 1994, pp. 723–730. DOI: 10.1007/978-1-4615-2468-7_95 (cit. on p. 47).

[64] M. A. Yaseen, V. J. Srinivasan, S. Sakadžić, D. A. Boas, A. M. Dale, and A. Devor. «Microvascular Oxygen Tension and Flow Measurements in Rodent Cerebral Cortex during Baseline Conditions and Functional Activation». In: *Journal of Cerebral Blood Flow & Metabolism* 31.4 (2010), pp. 1051–1063. DOI: 10.1038/jcbfm.2010.227 (cit. on p. 48).

[65] S. Sakadžić, E. Mandeville, L. Gagnon, J. Musacchia, M. A. Yaseen, and D. A. Boas. «Large arteriolar component of oxygen delivery implies a safe margin of oxygen supply to cerebral tissue». In: *Nature Communications* 5 (2014), p. 5734. DOI: 10.1038/ncomms6734. URL: https://doi.org/10.1038/ncomms6734 (cit. on p. 48).

[66] İ. Şencan et al. «Optical measurement of microvascular oxygenation and blood flow responses in awake mouse cortex during functional activation». In: *Journal of Cerebral Blood Flow & Metabolism* 42.3 (Mar. 2022). Epub 2020 Jun 9, pp. 510–525. DOI: 10.1177/0271678X20928011 (cit. on p. 48).

[67] B. Li et al. «Measurements of cerebral microvascular blood flow, oxygenation, and morphology in a mouse model of whole-brain irradiation-induced cognitive impairment by two-photon microscopy and optical coherence tomography: evidence for microvascular injury in the cerebral white matter». In: *Geroscience* 45.3 (June 2023). Epub 2023 Feb 16, pp. 1491–1510. DOI: 10.1007/s11357-023-00735-3 (cit. on p. 48).

[68] F. R. M. Beinlich et al. «Oxygen imaging of hypoxic pockets in the mouse cerebral cortex». In: *Science* 383.6690 (2024), pp. 1471–1478. DOI: 10.1126/science.adn1011. URL: https://doi.org/10.1126/science.adn1011 (cit. on p. 66).